

University of Denver

Digital Commons @ DU

Electronic Theses and Dissertations

Graduate Studies

1-1-2018

Superresolved Three-Dimensional Analysis of the Spatial Arrangement of the Human Immunodeficiency Virus Type-1 (HIV-1) Envelope Glycoprotein at Sites of Viral Assembly

Carmen Anne Buttler
University of Denver

Follow this and additional works at: <https://digitalcommons.du.edu/etd>



Part of the [Cell Biology Commons](#), [Molecular Biology Commons](#), and the [Virology Commons](#)

Recommended Citation

Buttler, Carmen Anne, "Superresolved Three-Dimensional Analysis of the Spatial Arrangement of the Human Immunodeficiency Virus Type-1 (HIV-1) Envelope Glycoprotein at Sites of Viral Assembly" (2018). *Electronic Theses and Dissertations*. 1449.
<https://digitalcommons.du.edu/etd/1449>

This Thesis is brought to you for free and open access by the Graduate Studies at Digital Commons @ DU. It has been accepted for inclusion in Electronic Theses and Dissertations by an authorized administrator of Digital Commons @ DU. For more information, please contact jennifer.cox@du.edu, dig-commons@du.edu.

Superresolved Three-Dimensional Analysis of the Spatial Arrangement of the *Human
Immunodeficiency Virus Type-1* (HIV-1) Envelope Glycoprotein at Sites of Viral Assembly

A Thesis

Presented to

the Faculty of Natural Sciences and Mathematics

University of Denver

In Partial Fulfillment

of the Requirements for the Degree

Master of Science

by

Carmen Anne Buttler

June 2018

Advisor: Professor Schuyler Van Engelenburg

Author: Carmen Anne Buttler

Title: Superresolved Three-Dimensional Analysis of the Spatial Arrangement of the *Human Immunodeficiency Virus Type-1* (HIV-1) Envelope Glycoprotein at Sites of Viral Assembly

Advisor: Professor Schuyler Van Engelenburg

Degree Date: June 2018

ABSTRACT

Human Immunodeficiency Virus type 1 (HIV-1) replicates by forcing infected host cells to produce new virus particles, which assemble from protein components on the inner leaflet of the host cell's plasma membrane. This involves incorporation of the essential viral envelope glycoprotein (Env) into a structural lattice of viral Gag proteins. The mechanism of Env recruitment and incorporation is not well understood. To better define this process, we seek to describe the timing of Env-Gag encounters during particle assembly by measuring angular positions of Env proteins about the surfaces of budding particles. Using three-dimensional superresolution microscopy, we show that Env distributions are biased toward the necks of budding particles, indicating incorporation of Env late in the assembly of the lattice. We show that this behavior is dependent on the host cell type and on the long cytoplasmic tail of Env. We propose a model wherein Env incorporation is regulated by opposing mechanisms: Gag lattice trapping of Env cytoplasmic tails, and intracellular sequestering of Env during lattice assembly.

ACKNOWLEDGEMENTS

I thank Dr. Van Engelenburg for his mentorship and for his guidance in experimental development, practice, and analysis. I also thank all current and past members of the Van Engelenburg lab, particularly Nairi Pezeshkian, for her collaboration on all live-cell labeling and imaging experiments, and Sofya Norman, for her help with cloning of modified viral genome plasmids. I thank Melissa Fernandez and Eric Freed for their input and for their collaboration on all biochemical and infectivity assays. I thank Harald Hess and Gleb Shtengel of the Howard Hughes Medical Institute Janelia Research Campus for their input and support. I also thank Jennifer Bourne and the Electron Microscopy Center at the University of Colorado Anschutz Medical Campus for assistance with transmission electron micrograph collection. IPALM microscopy was performed at the Advanced Imaging Center at Janelia Research Campus, jointly sponsored by the Gordon and Betty Moore Foundation and the Howard Hughes Medical Institute. Work was supported by funding from the National Institute of Allergy and Infectious Disease (Grant #5R21AI127192) and by the Boettcher Foundation Webb-Waring Biomedical Research Award.

TABLE OF CONTENTS

Chapter One: Introduction.....	1
Chapter Two: Defining Angular Distributions of Env.....	10
Chapter Three: Diffusion of Env on the Plasma Membrane.....	47
Chapter Four: Host Cell Intracellular Trafficking as a Regulator of Env incorporation.....	59
Chapter Five: Conclusions.....	73
References.....	78

LIST OF FIGURES

Chapter One.....	1
Figure 1.1 Gag drives assembly and maturation of HIV-1 particles.....	4
Figure 1.2 Hypothetical models for the angular distributions of Env about budding virus particles.....	8
Chapter Two.....	10
Figure 2.1 Point Localization can be used to estimate the sub-diffraction limited location of single point source emitters.....	12
Figure 2.2 The light collection, interference and detection system of an iPALM microscope.....	15
Figure 2.3 The uncertainty in localization of fluorophores from a representative dataset.....	20
Figure 2.4 Residual uncertainty of transformation of randomly sampled pairs of fiducial markers used for registration of one iPALM-imaged channel to another.....	21
Figure 2.5 Three color iPALM enables visualization of single HIV-1 assembly sites and resolution of Env clusters on a sub-viral spatial scale.....	23
Figure 2.6 Diagram representations of the two orthogonal methods of analysis used to quantify Env angular distributions.....	24
Figure 2.7 Weighted principal component analysis (PCA) was used to fit a plane to the local plasma membrane at each viral assembly site.....	27
Figure 2.8 The measured neck lengths of budding virus assembly sites imaged by iPALM agree with those measured by transmission electron microscopy.....	28
Figure 2.9 Estimated geometric characteristics of Env clusters were used to generate template Env clusters for simulation and for single cluster segmentation.....	29
Figure 2.10 Simulated budding particles demonstrate the particle averaging method of Env distribution analysis.....	31
Figure 2.11 Phase correlation of the angular (ϕ) probability density of Env between random half-datasets estimates the sampling resolution of Env.....	32
Figure 2.12 Phase correlation of the probability density of plasma membrane between random half-datasets estimates alignment error.....	32
Figure 2.13 Diagram describing simulation of error in rotational alignment of assembling viral particles.....	34
Figure 2.14 Radius and residual error of Gag shell fitting for a representative dataset.....	35
Figure 2.15 Geometric characteristics of aligned segmented plasma membranes.....	36
Figure 2.16 Results of simulated error in rotational alignment of assembly sites.....	37
Figure 2.17 Angular distributions of Env measured by segmentation of individual Env clusters.....	39
Figure 2.18 The mean ϕ value of individual segmented Env clusters describes the overall distribution bias.....	40
Figure 2.19 Cross-section probability density volumes of aligned assembly sites show Env angular biases.....	41
Figure 2.20 Distributions of angular probability densities by particle averaging.....	42
Figure 2.21 Immunogold labeling and transmission electron microscopy imaging of Env at assembly sites.....	44
Chapter Three.....	47
Figure 3.1 Incorporation of Env-CT mutants is defective in both CEM-A and COS7 cells.....	48
Figure 3.2 Differential Env incorporation between producer cell types.....	49
Figure 3.3 Single particle tracking of Env trimers, classified as mobile or trapped.....	53

Figure 3.4 Distributions of diffusion coefficients calculated for all tracks in each condition.....	54
Figure 3.5 Diffusion coefficients of mobile Env trimers do not differ significantly between genotype or cell type.....	55
Figure 3.6 The fraction of Env trimers classified as trapped is dependent on the Env-CT.....	56
Chapter Four.....	59
Figure 4.1 Density of Env on the host cell surface in CEM-A cells is dependent on Env-CT.....	61
Figure 4.2 Density of Env on the surfaces of host cells in COS7 cells is upregulated by deletion of the Env-CT, as it is in CEM-A cells.....	62
Figure 4.3 The internalized pool of Env in CEM-A cells is dependent on the Env-CT.....	65
Figure 4.4 Env labeled at the cell surface is endocytosed and sorted to the recycling compartment.....	66
Figure 4.5 Internalized pools of Env in COS7 cells are altered by mutation, but not by deletion of the Env-CT.....	67
Figure 4.6 Analysis of intracellular Env flux by Fluorescence Recovery After Photobleaching.....	70
Figure 4.7 Working model for the fate of single Env trimers during HIV-1 assembly.....	72

CHAPTER ONE: INTRODUCTION

Human Immunodeficiency Virus (HIV) is a major human health threat. Millions of people around the world are infected with HIV, and an estimated 2 – 3 million more people become infected each year (Klasse, 2012). Untreated HIV infections cause Acquired Immunodeficiency Syndrome (AIDS), which causes an estimated 1 million deaths every year. HIV can be treated with antiretroviral drugs to prevent the progression to AIDS, but there is currently no cure for the infection and no vaccine to protect against infection. Furthermore, undiagnosed infections are very common, even in diagnosed cases access to drugs can be limited, and failure to maintain drug treatment can still lead to the development of AIDS. If a cure is ever to be developed, a thorough understanding of the virus's infection cycle is needed.

HIV is an enveloped retrovirus that infects cells of the human immune system. It relies on infected host cells to produce new infectious virus particles by integrating its own genome into the DNA of the host cell, forcing the cell to replicate the viral genome and synthesize viral proteins in the normal course of its own processes. Retroviruses, whose viral genomes are packaged into infectious virus particles as RNA, accomplish this genome integration by using reverse transcriptase to convert their RNA genome into double stranded DNA, which is then spliced at random into the host cell's DNA by viral integrase (Craigie and Bushman, 2012; Ellison et al, 1990; Farnet and Haseltine, 1990). The infected cell will then begin to transcribe the encoded mRNA and synthesize viral proteins. These viral proteins, through their various synthesis and trafficking pathways, co-localize at sites of virus particle assembly on the inner leaflet of the cell's plasma membrane. In conjunction with certain hijacked host cell factors, the viral proteins form spherical membrane bud structures that protrude from the cytoplasm into the extracellular space and pinch off from the host cell membrane as new virus particles. When all of the essential viral

components are packaged into this budding particle before it pinches off, an infectious virion is produced, enveloped in the host cell's plasma membrane and containing all of the machinery necessary to repeat the infection cycle in a new host cell.

HIV type 1 (HIV-1) virions infect human immune cells that express the surface glycoprotein CD4, primarily helper T-cells. In healthy cells, CD4 is a coreceptor of the T-cell Receptor (TCR) and helps bind the Major Histocompatibility Complex class II (MHCII) on the surfaces of antigen-presenting cells. HIV-1 virions, enveloped in a lipid bilayer derived from their originating host cell's plasma membrane, must fuse their own membrane with that of the target cell to infect it. Fusion is enabled through binding of CD4 by the viral transmembrane glycoprotein Envelope (Env), a heavily glycosylated trimeric heterodimer and the only externally exposed viral component of the virion. The gp120 subunit of Env binds CD4, causing a conformational change in gp120 that allows it to bind a second host cell receptor, C-C Chemokine Receptor type 5 (CCR5; Kwong et al, 1998). A second conformational change induced by CCR5 binding allows the transmembrane subunit of Env, gp41, to contact the target cell plasma membrane and initiate fusion with the viral membrane and injection of the capsid-encased viral genome and protein components (the viral core) into the cell's cytoplasm (Klasse, 2012). In the cytoplasm, the viral RNA genome is reverse transcribed into double stranded DNA and forms the pre-integration complex (PIC) with viral capsid and integrase, among other factors (Lucic and Lusic, 2016). The PIC conveys the DNA genome into the cell nucleus, where integrase facilitates the integration of the genome by transposition of the two Long Terminal Repeat (LTR) sequences at either end of the viral genome into the host cell DNA at a non-specific site (Craigie and Bushman, 2012). Once integrated, the viral genome is replicated along with the host genome during cell division, transcribed in full as an RNA genome to be incorporated into new virus, and transcribed into spliced subunits of mRNA to be translated into the viral proteins required to make new virus particles.

The various protein components of the virus are synthesized by the infected cell through multiple biogenesis pathways. This study is concerned with two of these components in

particular: Gag, the main structural component responsible and sufficient for the formation of the protruding bud structures that become virus particles, and Env, the transmembrane spike protein responsible for facilitating binding and entry of released virus particles to new host cells. The co-localization of these two proteins at viral assembly sites is crucial to the production of infectious particles, but the mechanisms involved are poorly understood.

Gag and its frame-shifted enzymatic variant Gag-Pol are translated in the host cell cytoplasm and targeted to the plasma membrane by an N-terminal myristoylation and hydrophobic region of the matrix (MA) domain (Zhou et al, 1994; Ono et al, 2004; Saad et al, 2006). Gag monomers anchored to the inner leaflet of the plasma membrane oligomerize through interaction of their capsid (CA) domains to form a curved hexameric lattice of trimers which deforms the host cell's membrane into a protruding spherical bud (Figure 1.1A; Alfadhli et al, 2009; Briggs et al, 2009; Sundquist and Krausslich, 2012; Freed, 2015). The nucleocapsid domain of Gag recruits the viral genomic RNA to be packaged into the new virus particle, and the p6/late domain recruits host cell Endosomal Sorting Complexes Required for Transport (ESCRT) proteins, which aid in the pinching off of the budding membrane, leading to release of the assembled particle (Figure 1.1B; Gottlinger et al, 1991; Huang et al, 1995; Freed, 2002; Lippincott-Schwartz et al, 2017). Following particle release, the subdomains of Gag and Gag-Pol are cleaved by protease (PR) into separated proteins. Gag MA remains at the inner leaflet of the viral envelope while Gag CA forms a conical capsid around the viral core, including the viral genome, integrase and reverse transcriptase (Sundquist and Krausslich, 2012; Freed, 2015). This cleavage-based maturation step is necessary for the infectivity of released virions (Figure 1.1C).

Meanwhile, the transmembrane glycoprotein Env is synthesized through the canonical secretory pathway. Its precursor, gp160, is translated at the endoplasmic reticulum (ER) and co-translationally inserted into the ER membrane (Checkley et al, 2011). The luminal domain is heavily glycosylated in the ER, and glycosylated gp160 proteins trimerize before being trafficked

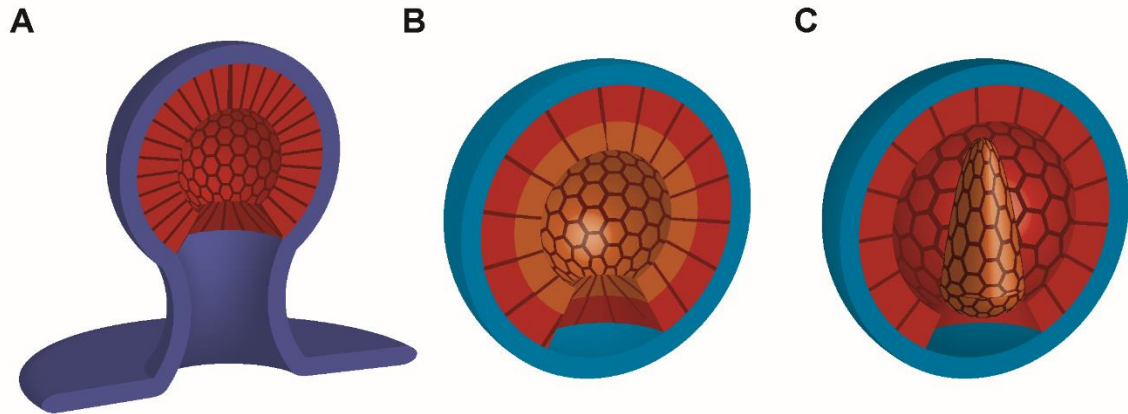


Figure 1.1. Gag drives assembly and maturation of HIV-1 particles. **(A)** The myristoylated N-terminus of the Gag MA domain targets Gag (red) to the inner leaflet of the host cell's plasma membrane (dark blue). The assembly of the curved Gag lattice, through interaction of the Gag CA domains, induces membrane curvature and causes budding of virus assembly sites, which protrude from the cell membrane. **(B)** Virus particles pinch off from the host cell plasma membrane and the plasma membrane becomes the viral envelope (light blue). In immature particles, Gag remains intact. The MA domain (red) remains associated with the viral envelope, and the CA domain (orange) maintains the lattice shell structure. **(C)** Virus particles mature through cleavage of the sub-domains of Gag by viral protease. The CA domain (orange) is cleaved from the MA domain (red) and forms a conical capsid around the viral core. MA remains associated with the viral envelope (blue), but does not retain its tight lattice structure in the absence of CA.

to the Golgi. In the Golgi, host cell proteases cleave gp160 into the two components of mature Env: gp120 and gp41 (McCune et al, 1988; Checkley et al, 2011). The components remain associated as a trimer of heterodimers, with gp120 as the luminal, and later the extracellular domain, and with gp41 comprising the transmembrane domain and the long cytoplasmic tail (Env-CT). Env is exocytosed to the cell surface where it diffuses freely in the plasma membrane but is quickly and specifically endocytosed and trafficked through the intracellular recycling endosome before being returned to the cell surface. This recycling pathway has been shown to be dependent on elements of the Env-CT (Egan et al, 1996; Groppelli et al, 2014; Kirschman et al, 2018).

Env trimers on the plasma membrane are efficiently incorporated into Gag lattices by an unknown mechanism. Env is seen to preferentially co-localize with Gag on host cell plasma membranes, again dependent on the Env-CT (Freed and Martin, 1995; Mammano et al, 1995; Akari et al, 2000; Murakami and Freed, 2000; Muranyi et al, 2013). Lentiviruses like HIV-1 have extraordinarily long cytoplasmic tails to their Env proteins, often, and in the case of HIV-1, more than twice the length of other retroviruses (Postler and Desrosiers, 2013). The long cytoplasmic tail of HIV-1 Env has been found to be required for efficient incorporation into virus particles, although this appears to have some dependence on host cell type (Akari et al, 2000; Murakami and Freed, 2000; Muranyi et al, 2013). The preferential co-localization of Env and Gag on cell surfaces could be explained by specific recruitment of either protein by the other, or by recruitment of both proteins to specific sites for assembly. Some studies have proposed that Gag either localizes to or creates membrane raft domains that may either attract or be induced by the presence of Env (Ono and Freed, 2001). Taken together, these studies would seem to suggest a mechanism for upregulating Env incorporation into virus particles by specific co-localization of Env with Gag lattices, but this model is complicated by the unusual sparsity of Env on released HIV-1 virus. Electron microscopy studies have shown that only 7 – 14 Env trimers occupy the surface of each virus particle (Zhu et al, 2003).

The sparsity of Env on released virus particles, despite the efficiency of its co-localization with sites of particle assembly, suggests that the incorporation of Env into Gag lattices during particle assembly is, by some mechanism, downregulated. This sparsity has been shown to decrease the infectivity of the virus particles (Stano et al, 2017). It is therefore likely that the tightly regulated sparsity of Env benefits the overall proliferation of the virus in some other way that compensates for the reduced infectivity of released virions. As Env is the only viral component of the enveloped HIV-1 particle that is externally exposed and recognizably “non-self,” it may be that regulating the density of Env on individual particles could help to minimize the likelihood of virus and infected cells being identified and destroyed by the host immune system before they can proliferate an infection.

The mechanism of this regulation is poorly defined, as is the mechanism of Env’s efficient co-localization with Gag. Several models have been proposed to describe the latter process (reviewed in Tedbury and Freed, 2014). The first model involves independent recruitment of Gag and Env to specific sites on the plasma membrane. This model assumes the lipid raft hypothesis of distinct membrane domains that exist independently of either protein, which remains a controversial concept, and while it can explain the preferential co-localization of Gag and Env, it does not explain the sparsity of Env incorporation. The second model describes a direct interaction of Gag with Env that is necessary for the incorporation of Env. This model fits well with the observed co-localization of the two proteins and the fact that mutations in Gag have been seen to rescue incorporation of mutant Env (Ono et al, 1997; Tedbury et al, 2013), but it cannot explain the sparsity of Env, and it cannot explain the cell type dependence of Env incorporation defects in the absence of the Env-CT. The third model involves indirect interaction of Env and Gag through their independent interaction with some unknown host factor. This would explain the cell type specific Env-CT dependence of incorporation, and could possibly explain the sparsity of Env if the host cell factor density is limiting, but neither it nor the direct interaction model can explain the observed co-localization of Gag with analogous glycoproteins of other viruses (Jorgenson et al, 2009). The fourth model suggests that Env occupies released virus membranes

by passive incorporation; there is no active mechanism of incorporation, Env diffuses freely across the surface of the plasma membrane and as viral buds pinch off from the host cell, they incorporate any Env that happens to be on the bud surface at the time of abscission. This would explain the low density of Env on released particles, but does not fit with the efficient co-localization of Env and Gag. However, if the free diffusion of Env were somehow halted by encounter with a Gag lattice, both preventing diffusion away from an assembly site once it has been encountered and specifically preventing endocytosis of incorporated Env (Egan et al, 1996), this model could explain the observed co-localization of the two proteins as an artifact of Gag's disruption of Env endocytosis. Some studies support this hypothesis, showing that the cytoplasmic tail of Env may become sterically trapped in the lattice of Gag at assembly sites, but diffuses freely when Gag matures and the lattice breaks down (Chojnacki et al, 2012; Roy et al, 2013; Chojnacki et al, 2017).

In order to explore this hypothesis and to probe potential mechanisms regulating incorporated Env density, we sought to determine the relative timing of Gag's and Env's arrivals at sites of viral assembly on the plasma membrane. We hypothesized that the order of recruitment of the two proteins would illuminate the nature of their interaction with each other. Because previous studies have suggested that Env becomes fixed in the immature Gag lattice of unreleased assembling particles (Chojnacki et al, 2012; Roy et al, 2013; Chojnacki et al, 2017), we expected that the timing of Env's arrival relative to the progress of Gag lattice oligomerization would be encoded by the angular distribution of Env about particles late in the assembly process. If an Env trimer will become trapped wherever the outer edge of the lattice was when the Env first encountered it, then we can infer the timing of this encounter from Env's angular position at the endpoint of particle assembly. We designed experiments to interrogate the angular distribution of Env at these assembly sites by fluorescence microscopy. We proposed three potential distribution models that would result from various models of Env-Gag co-localization (Figure 1.2). If Gag is recruited to sites of Env clustering, then we would expect to see that, on average, distributions of Env are biased toward the crowns (the upper hemispheres) of budding particles

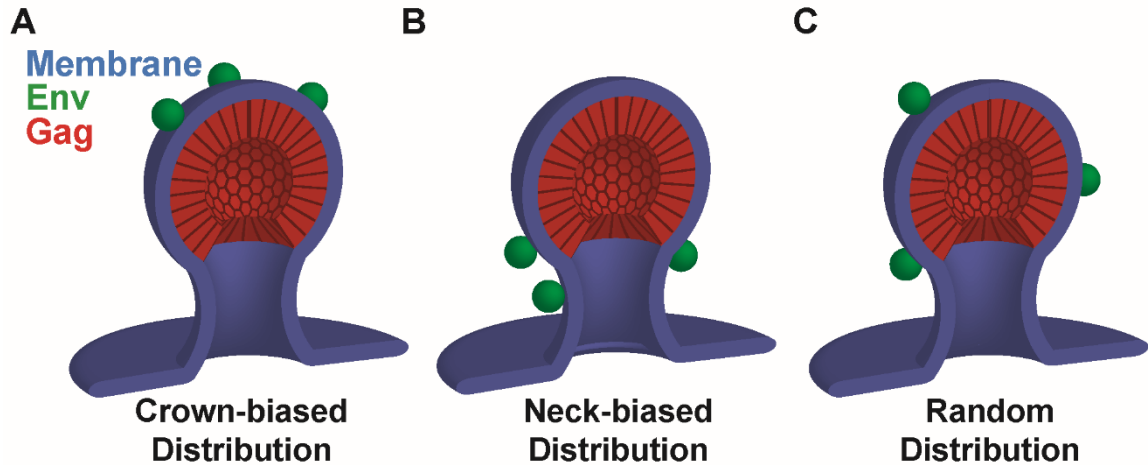


Figure 1.2. Hypothetical models for the angular distributions of Env about budding virus particles. According to our hypothesis, the timing of Env encounter with virus particle assembly sites can be inferred from the distribution of Env fixed in the Gag lattice. Here the three possible distributions of Env (external domain represented by green spheres) are diagrammed. **(A)** We would expect for a crown-distributed Env distribution to result from assembly of Gag lattices at sites of Env clustering. **(B)** Neck-distributed Env clusters are expected to result from late acquisition of Env at assembly sites, after the Gag lattice has begun to assemble. **(C)** We expect unbiased distributions of Env clusters as the result of two possible causes. Env will be distributed randomly over the particle surface if it is stochastically trapped throughout Gag assembly, or if it does not become fixed in the lattice when it encounters assembly sites.

(Figure 1.2A). If Env is incorporated to already-assembling Gag lattices, then we would expect to see that, on average, distributions of Env are biased toward the necks (the lower, cell-proximal hemispheres) of budding particles (Figure 1.2B). If Env incorporates nonspecifically throughout the assembly of the Gag lattice, or if Env does not become fixed in the lattice as has been suggested, then we would expect a random or un-biased angular distribution of Env on the surfaces of budding particles (Figure 1.2C).

CHAPTER TWO: DEFINING ANGULAR DISTRIBUTIONS OF ENV

In order to discriminate between our three expected models (Figure 1.2) using fluorescence microscopy, we needed to be able to measure the angular positions of the Env trimers that were incorporated into unreleased budding assembly sites. To do that, we needed to localize Env trimers on the surfaces of cell-associated budding virus particles at a spatial scale smaller than the size of the virus particle itself, and we need to be able to localize them in reference to both the centroid of the Gag shell and the angle and polarity of the particle's budding axis. The relative positions of Env and Gag can be measured simply by immunolabeling both proteins with antibodies conjugated to two different organic dyes with resolvable excitation and emission spectra. However, while the Gag shell does have a gap at its base where the "neck" of the budding particle connects it to the host cell cytoplasm, labeling density and the small size of this gap make it an unreliable indicator of budding polarity. Instead, identification of the budding axis was accomplished by labeling of the host cell plasma membrane. The local plane of the plasma membrane at sites of virus assembly could be fit to a plane which defined a normal vector that approximated the budding axis of the associated virus particle.

To differentiate angles about the virus particle, all three of these components had to be localized in three dimensions on a sub-viral spatial scale. HIV-1 virus particles are an average 150 nm in diameter, which is well below the diffraction limit of light. Until recent years, the ability of light microscopy to visualize biological structures was limited by the fundamental diffraction limit of light. The diffraction of light waves makes it impossible to focus an image at a resolution smaller than approximately half of the wavelength of light in question in a projected 2D image ($\lambda / 2NA$, where λ is the wavelength of light being resolved and NA is the numerical aperture of the objective being used to collect it) and approximately the full wavelength in the third dimension,

along the light wave ($2\lambda / NA^2$). For the visible spectrum, this means a resolution limit of, at best, about 250 nm in the planar dimensions of the image, and about 500 nm in the axial dimension of the light collection. Many crucial biological structures, including our virus particles, are smaller than this resolution limit, and therefore are unresolvable by conventional, diffraction limited light microscopy. In order to measure the locations of particular proteins on the surface of a virus particle, we needed to be able to resolve our images on a much smaller scale.

It is possible to estimate the location of a fluorescent emitter at a sub-diffraction limited scale using the technique of point localization. In a diffraction limited image, each single emitter is resolved as a point spread function (PSF). By fitting the diffraction limited PSF to a two-dimensional Gaussian distribution, which approximates an airy disk (the theoretically ideal PSF), the actual position of the emitter can be localized by finding the peak of the Gaussian (Figure 2.1). The uncertainty of this localization is defined by the sampling of the Gaussian distribution, which is related to the brightness of the emitter. The brighter a fluorophore is, the more photons it will emit. The more photons are detected for each PSF, the better it will be sampled and the better it will be fit to a Gaussian, making for greater certainty in localization of the Gaussian peak. This uncertainty can be described by the following equation:

$$\sigma^2 = \frac{\sigma^2 + a^2/12}{N} + \frac{4\sqrt{\pi}s^3b^2}{aN^2}$$

where N is the number of photons detected, b is the photons due to background noise, s is the standard deviation of the Gaussian fit, and a is the pixel size of the magnified image (Betzig et al, 2005).

Unfortunately, this method will only work if each diffraction limited point spread function corresponds to only one point source emitter, which means that single emitters must be dispersed sparsely enough to be resolvable at the diffraction limit anyway. This makes point localization essentially useless for resolving complex, sub-diffraction limited biological structures. However, a 1995 paper proposed a theoretical means of circumventing this problem (Betzig, 1995). The suggested solution points out that multiple emitters whose point spread functions

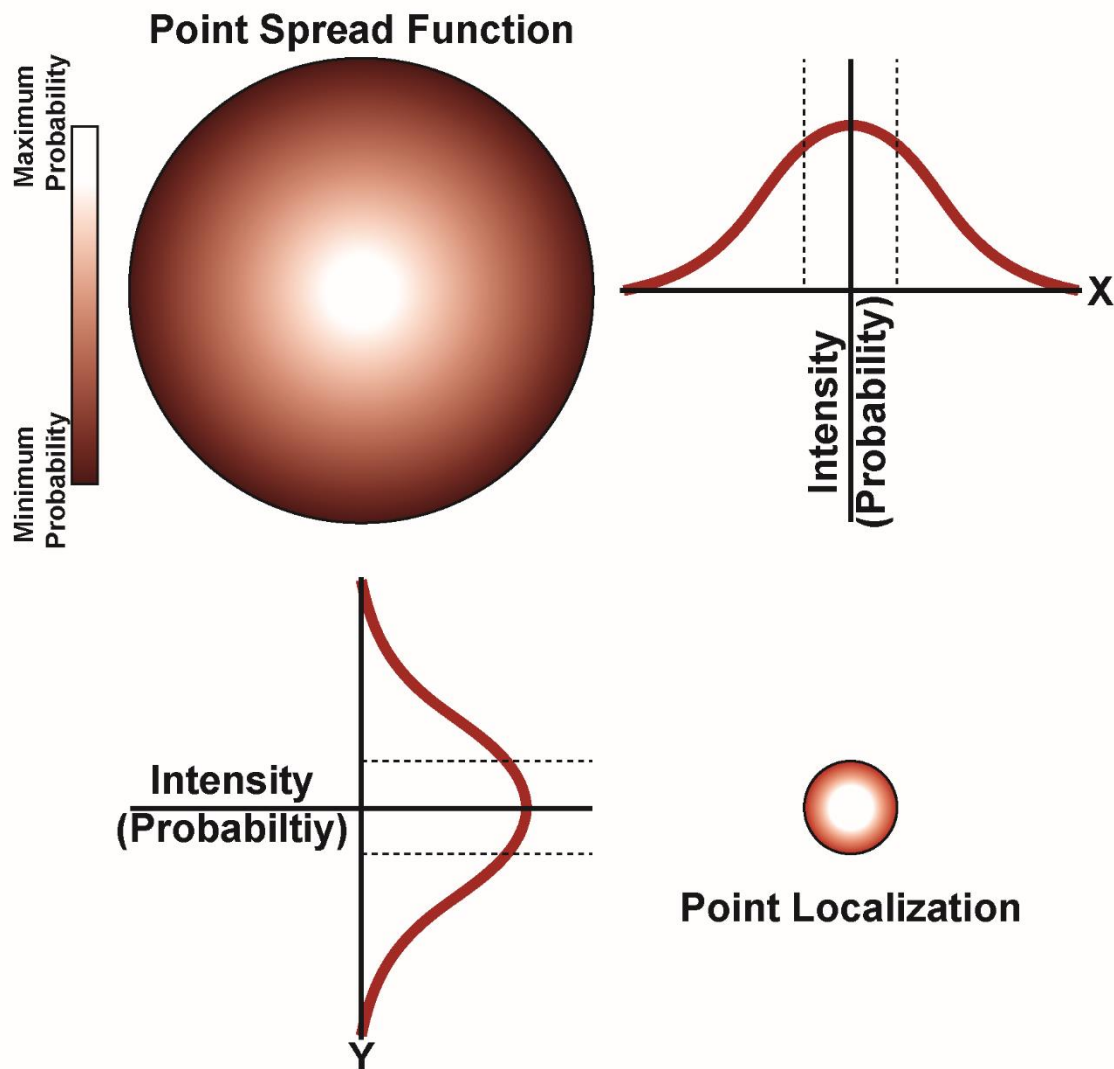


Figure 2.1. Point Localization can be used to estimate the sub-diffraction limited location of single point source emitters. The wave properties of light make it impossible to focus a light wave to less than its diffraction limit. In a diffraction limited image, a single point source emitter will be projected as a point spread function (PSF, lower left). Signal intensity (photon count) varies over this area as an airy disk distribution. When the PSF is projected across multiple detecting pixels, the distribution of photon count over those pixels can be used to fit a function to the distribution of photons. Over this gross detection profile, a 2D Gaussian distribution (upper left and lower right) approximates an airy disk. Point localization uses this fit distribution of signal intensity to pinpoint the sub-diffraction limited location of the point source emitter at the peak of the 2D Gaussian, with a certainty determined by how well sampled the distribution is by collected photons (upper right).

overlap at the diffraction limit can still be resolved from each other if they are resolvable in some other dimension. For instance, if two proximal emitters are spectrally resolvable, their emitted photons can be differentiated, and their PSF's can be fit separately. A much more convenient "resolvable state" by which emitters can be distinguished is time. If various sub-populations of sparsely dispersed emitters are sampled separately over resolvable periods of time, they can be superresolved by point localization, and then overlaid to reconstruct a much denser image without sacrificing resolution. This is the method upon which both PALM and dSTORM imaging are based.

Photo-Activated Localization Microscopy (PALM; Betzig et al, 2006) and direct Stochastic Optical Reconstruction Microscopy (dSTORM; Heilemann et al, 2008) both rely on the ability to resolve spatially sparse subsets of single emitters in time. Both techniques do this by using fluorophores that can be made to occupy a dark, non-emitting state. At any given time, most emitters must be in this dark state so that the subset that are in the bright state and are being detected can be assumed to be sparsely dispersed enough to apply point localization. The bleaching of bright-state emitters, combined with the continuous sparse conversion of dark-state emitters to the bright state, either spontaneously or by photo-activation with a high energy laser pulse, ensures the turnover of the population of bright emitters being detected. Each temporally resolved frame can be separately subjected to point localization of its detected subset of point spread functions, and the resulting superresolution images can be overlaid to reconstruct a single superresolved, sub-diffraction sampled image. PALM employs fluorescent proteins with multiple spectral states to accomplish this, whereas dSTORM uses organic dyes which can be chemically shelved in a dark state using an oxygen scavenging buffer (Appendix A), which prevents reactive oxygen from irreversibly bleaching the dyes and allows them to be reversibly photobleached to a dark state through light-induced interaction with thiols which quench their fluorescence. This allows dyes to return spontaneously to their bright states over long periods of time as these quenching interactions spontaneously dissociate. In both PALM and dSTORM, the majority of emitters are in their dark state and a sparse population are converted to the bright state at any

given time, either spontaneously or by photo-stimulation. This activated population will be imaged and then irreversibly bleached; they will go dark and cannot return to a bright state. Another population of sparse fluorophores can then replace them in the bright state to be imaged separately, ideally without overlapping PSF's.

These techniques were originally conceived as two-dimensional imaging methods. However, several strategies have since been developed for their three-dimensional application. The simplest is astigmatism (Kao and Verkman, 1994; Huang et al, 2008). Astigmatism introduces an optical deformation to point spread functions that are out of focus. An emitter's PSF becomes elliptical rather than circular when the emitter is above or below focus, and the axial position of the emitter relative to the focal plane can be calculated based on the aspect ratio of the PSF. However, the resolution of this technique in the axial dimension is limited, and our applications required isotropic sub-viral resolution to be able to accurately measure angular positions of Env clusters. A 2009 paper described a modification to the PALM/dSTORM method which allows the axial resolution we required using interferometry (Shtengel et al, 2009). Interferometric PALM (iPALM) derives a third superresolved dimension by taking advantage of the wave properties of the emitted light. The fluorescent signal is collected through two opposing objectives, above and below the sample. The two collected light paths are redirected into a three-way beam splitter (Figure 2.2), where they converge and interfere with each other. The photons given off by each single emitter in the sample will be collected by both objectives and will travel through both light paths to the beam splitter. However, the lengths of the two light paths are not perfectly identical, so that when they meet, the photons will have traveled a slightly different distance through one than through the other. The difference between the traveled distances will be determined by the axial position of the emitter between the two objectives, and it will define the relative phase of the two sets of corresponding photons when they interfere and, therefore, the nature of their interference. If the signals in each light path from a single emitter are in phase with each other when they interfere, they will interfere constructively, and the intensity of the resulting signal will be greater. If they are out of phase, they will interfere destructively, and the resulting

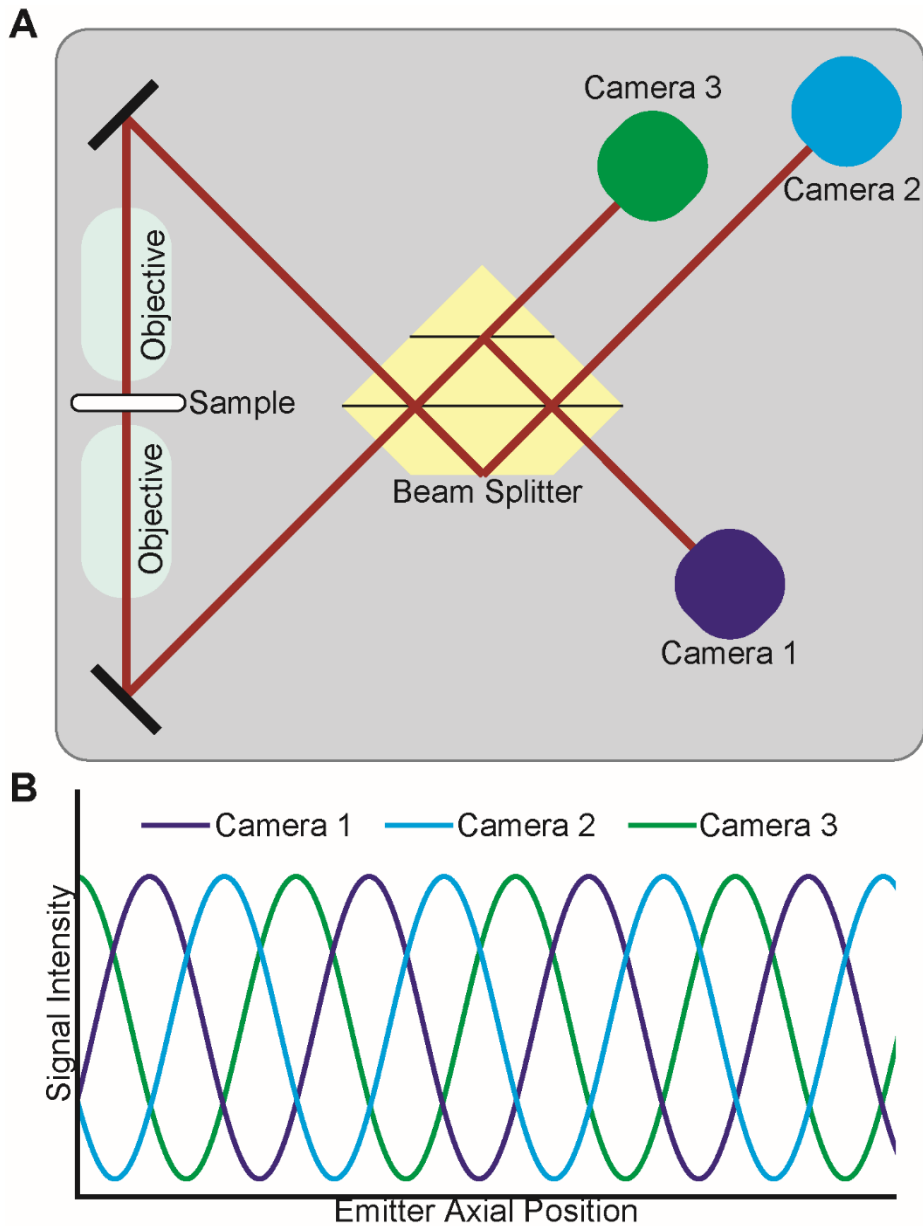


Figure 2.2. The light collection, interference and detection system of an iPALM microscope. (A) Light (red) emitted in the sample (white) is collected through two opposing objectives (gray). Mirrors (black) redirect both light paths into a three-way beam splitter (yellow). The light paths interfere with each other, altering the intensity of the resulting light paths based on their relative phase. One resultant light path is partially directed out of the beam splitter and detected by an EM-CCD camera (green), and partially reflected within the beam splitter, so that it interferes again with the second resultant light path. The two light paths resulting from this second interference are collected by two additional EM-CCD cameras (blue, purple). **(B)** The intensities of the collected light paths cycle as the pattern of interference cycles. Path lengths within the beam splitter are such that the intensities of the three collected signals (green, blue, purple) are perfectly out of phase. In this way, there is never a resolution minimum in one camera (where intensity changes least at the peaks and troughs of the wave) that is not covered by a higher resolution (larger intensity change) in the other two cameras.

signal will be lower. The light paths interfere twice in the beam splitter and are collected by three separate cameras (Figure 2.2A). The pattern of relative intensities between the three cameras can be compared to a known calibration in order to infer the axial position of the original emitter within the sample. The three post-beam splitter light paths are perfectly out of phase with each other, such that the resolution of the detected intensity changes will be constant for every originating axial position, and will not have minima and maxima as the degree of change in intensity cycles, as would be the case if only one or two post-interference light paths were detected (Figure 2.2B). The resolution in the axial dimension of this system is much finer than that of astigmatism, but its depth of field becomes very limited. The pattern of interference, and therefore the pattern of resulting intensities, will cycle with the period of the light wave. This can be overcome by adding astigmatism. The resolution of the astigmatism method is fine enough to distinguish between periods of the interference signal, so it can be applied in addition to iPALM to assign emitters to the correct period, or “fringe.” Using this system, we were able to resolve our viral structures and their associated Env clusters with the necessary resolution to calculate accurate angular positions, and we were able to do so with a depth of field that allowed us to visualize the associated plasma membranes of infected host cells at each site and accurately identify the angle and polarity of the budding axis for each individual structure.

The host cells we infected in these experiments were of the CEM-A cell line (Tremblay et al, 1989), an adherent T-cell like cell line permissive for HIV-1 infection, used as a model for the natural host cells of HIV-1 infections (this cell line was obtained through the NIH AIDS Reagent Program, Division of AIDS, NIAID, NIH: CEM-A from Dr. Mark Wainberg and Dr. James McMahon, CEM-CL10). Cells were cultured in media without phenol red to reduce background fluorescence (Appendix B). Since Env incorporation has been suggested to be cell type dependent (Akari et al, 2000; Murakami and Freed, 2000; Muranyi et al, 2013), virus particles were also imaged in the fibroblast like cell line COS7 (#CRL-1651, ATCC, Manassas, VA; Appendix C), in order to test whether there are any differences in Env-Gag interactions between the two cell types. We used a modified HIV-1 NL4-3 reference genome, which encoded our

plasma membrane marker, S15-psCFP2 (Sochacki et al, 2014), lacked protease (Δ Pol), and containing a late domain mutation (Δ PTAP; Gottlinger et al, 1991; Huang et al, 1995, Freed, 2002). S15-psCFP2 is a myristoylated photo-switchable cyan fluorescent protein (psCFP2). It is targeted to the plasma membrane by its N-terminal myristoylation and allowed us to map the topology of the cell surface so that the budding axes of assembling virus particles could be determined. The Δ Pol mutation meant that the viral protease (PR) was not expressed and the Gag lattice could not be cleaved and could not mature. This was crucial to our experimental design because, as previous studies have suggested that Gag lattice maturation allows Env to become un-trapped and diffuse across particle surfaces (Chojnacki et al, 2012; Chocknacki et al, 2017), maturation deficient particles are necessary to keep Env locked in the lattice where encounter occurred. With maturation deficient particles we can expect that the angular positions of Env we measure accurately represent the point where the Env first encountered the Gag lattice and became trapped. Likewise, the Δ PTAP mutation, which prevents proper recruitment of the host cell ESCRT proteins responsible for particle release, is necessary to ensure that particles do not pinch off from the host cell membrane, release into the extracellular space and lose their polarity. With the Δ PTAP mutation, we can expect that particles we see have been arrested in a late stage of budding, have not been released and are still cell-associated, and therefore, that the angular positions we calculate with respect to the apparent budding axis will be accurate. A sequence encoding a FLAG tag (SGDYKDDDDK) was also added to the C-terminus of Gag for immunolabeling of this sterically crowded structure (van Engelenburg et al, 2014).

In order to produce virus with which to infect our cells for imaging, this modified viral genome was co-transfected into HEK293T cells (#CRL-11268, ATCC, Manassas, VA; Appendices C, D), along with a pSPAX2 plasmid, which encodes PR, allowing produced virus particles to mature even though they themselves are incapable of an infection that will synthesize PR, and with a pVSVG plasmid, which induced expression of the Vesicular Stomatitis Virus glycoprotein (VSVG). As a far less cell type specific fusion initiator than HIV-1 Env, the presence of VSVG on virus particles allowed our virus to infect COS7 cells, which lack CD4 and cannot be

infected by Env alone. However, neither of these co-transfected plasmids was packaged into the resulting virus particles. This allowed us to produce and collect released virions which would be able to infect both of the cell lines we intended to image (CEM-A and COS7), but which would then be incapable of producing further release- or maturation-competent virus. In this way, we were able to image CEM-A and COS7 cells expressing and assembling the release- and maturation-deficient mutant virus particles necessary for our experimental design, but at expression levels native to a true infection, rather than over-expressed by direct transfection, as has been a common caveat of previous studies.

Glass cover slips were cleaned (Appendix E) to minimize background signal due to light scattering and fluorescent contaminants, which can be detected by the single molecule-sensitive cameras used for iPALM. The coverslips were then scattered with gold nanorods that are constitutively fluorescent over a wide range of excitation wavelengths (#A12-25-700, Nanopartz, Loveland, CO). These were used as fiducial markers to align each of the three spectral channels from a single experiment, and to correct for any physical drift that might occur in the microscope system during image acquisitions. These gold nanorods were covered with a sputter coated layer of SiO₂ (Denton Explorer sputtering system; Denton Vacuum, Moorestown, NJ) to prevent them from being endocytosed by cells. We obtained these cleaned, nanorod treated, sputter coated coverslips from Harald Hess and Gleb Shtengel at the Howard Hughes Medical Institute (HHMI) Janelia Research Campus. We treated the coverslips with fibronectin to facilitate cell adhesion (Appendix F), and then added either CEM-A or COS7 cells. The cells were permitted to adhere fully before virus was added (Appendix G). Cells were allowed to express the viral proteins for 38 – 42 hours after infection before being fixed and prepared for imaging. This was found to be a sufficiently late time point to optimize both plasma membrane labeling with S15-psCFP2 and late-stage assembly of most virus particles. At approximately 24 hours post-infection, the media was aspirated and replaced with fresh media to maximize cell health.

After 38 – 42 hours of infection, the samples were chemically fixed by submerging the coverslip fully in a solution of 4% paraformaldehyde and 0.2% glutaraldehyde (Appendix H),

which crosslink the proteins and lipids of the cells, fixing them in place. This fixation was followed by three washes with a solution of 30 mM glycine in order to quench autofluorescence of the glutaraldehyde. As Gag is not exposed to the outside of the cell, and as antibodies cannot diffuse across the plasma membrane, the membrane had to be permeabilized with detergent before immunolabeling could be carried out. The samples were then subjected to a long blocking step, incubated in a solution of 10% bovine serum albumin for at least 30 minutes to prevent signal contamination due to nonspecific binding of antibodies, which would be detected by the highly sensitive cameras of the iPALM system just as well as “real” signal. Following blocking, the samples were immunolabeled with highly dilute, directly dye-labeled primary antibodies. The use of secondary antibodies was omitted to minimize nonspecific labeling, to prevent crowding of fluorophores that might degrade the sparsity of emitters needed for accurate point localization, and to minimize the physical size of the immunolabeling system. Antibodies themselves are approximately 7 nm in length, and a secondary antibody could be as much as 14 nm from the epitope of interest, which could become competitive with the resolution of our system under ideal conditions. Gag and Env were labeled by incubation with a cocktail of anti-Gag antibody KC57 (Beckman Coulter, Brea, CA) and α FLAG (#F3165, Sigma-Aldrich), both conjugated to the organic dye Alexafluor750 (AF750; #A20111, Life Technologies), and the anti-Env antibodies 2G12 (Polymun, Klosterneuburg, Austria; Buchacher et al, 1994; Trkola et al, 1996) and b12 (this reagent was obtained through the NIH AIDS reagent program, Division of AIDS, NIAID, NIH: anti-HIV-1 gp120 monoclonal IgG b12 from Dr. Dennis Burton and Dr. Carlos Barbas; Burton et al, 1991; Barbas et al, 1992; Burton et al, 1994; Roben et al, 1994), both conjugated to the organic dye Alexafluor647 (AF647; #A37566, Life Technologies). The samples were washed thoroughly, again to prevent non-specific labeling. They were then mounted in dSTORM buffer and sealed beneath a clean 18mm coverslip with gas-impermeable Vaseline or epoxy to prevent oxygen from entering the sealed system and saturating the oxygen scavenging capacity of the dSTORM buffer (Appendix I).

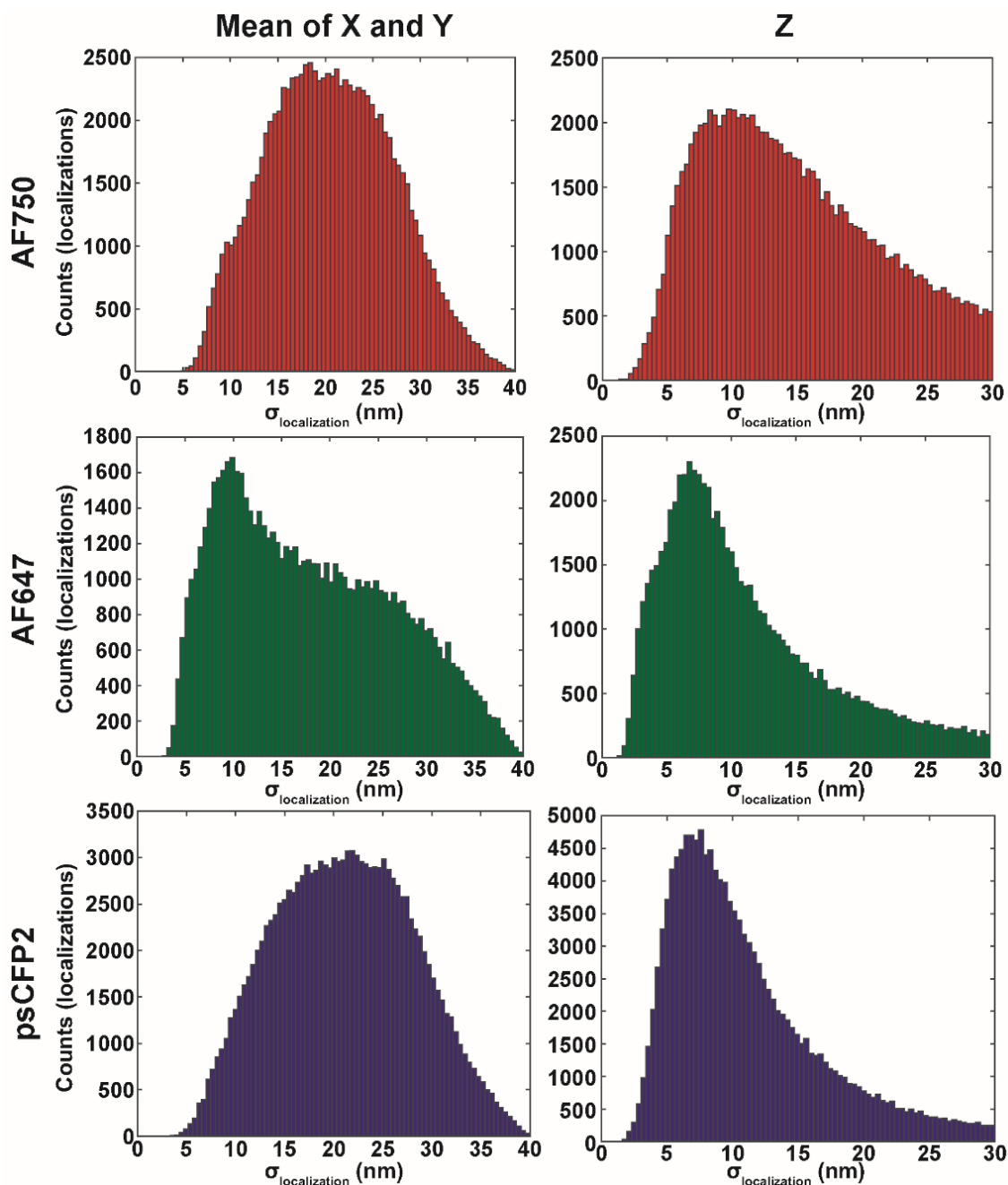


Figure 2.3. The uncertainty in localization of fluorophores from a representative dataset. Histogram representations of the σ values of localization precision for each single molecule localization in the planar X- and Y-dimensions (mean) and in the axial Z-dimension from all segmented particles of the largest collected dataset (d8-Env expressed in COS7 cells). For AF750 (red, top), the mean σ in X,Y = 20.6 ± 6.6 nm (left) and in Z = 14.6 ± 6.6 nm (right). For AF647 (green, middle), mean σ in X,Y = 18.0 ± 8.7 nm (left) and in Z = 11.0 ± 6.3 nm (right). For psCFP2 (blue, bottom), mean σ in X,Y = 21.1 ± 7.0 nm (left), and in Z = 11.0 ± 5.7 nm (right). Errors are given as standard deviation.

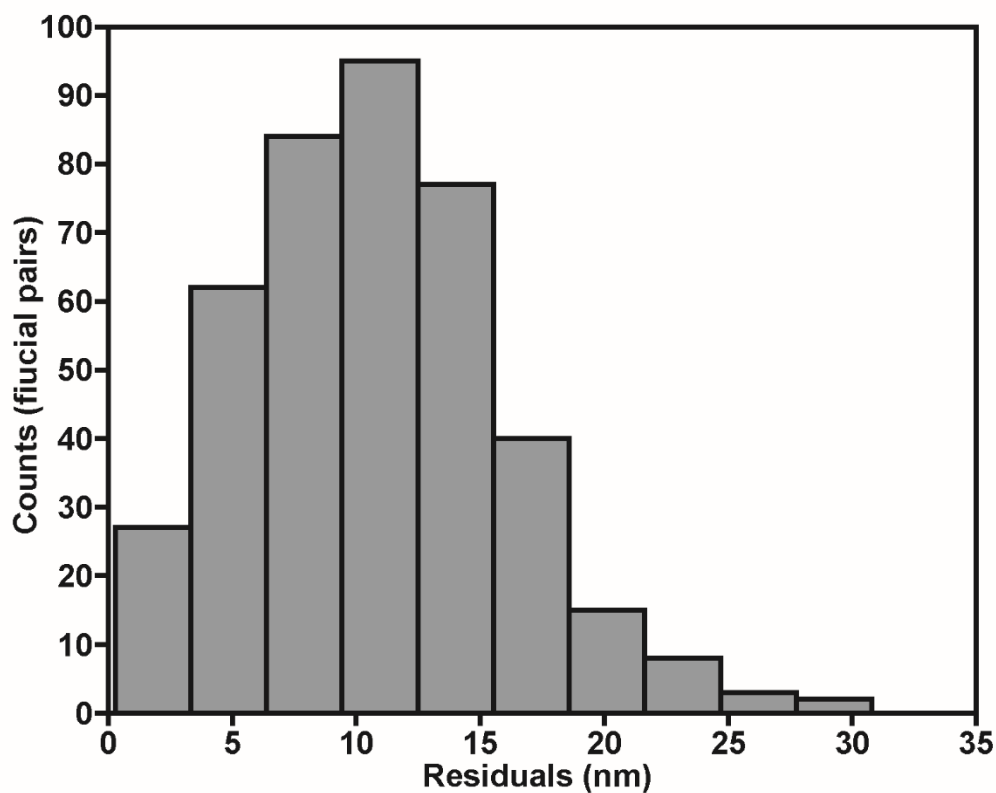


Figure 2.4. Residual uncertainty of transformation of randomly sampled pairs of fiducial markers used for registration of one iPALM-imaged channel to another. Broadly fluorescent gold nanorods were used as fiducial markers across all three channels. Alignment of sequentially imaged channels was accomplished by transformation of fiducial markers in one channel onto the corresponding markers in another. Here, a histogram describes the residuals of this registration for 413 fiducial pairs over 19 separate imaging experiments. The standard deviation of these residuals = $\sigma_{\text{registration}} = 5.2$ nm.

Imaging experiments were performed on the iPALM microscope at the HHMI Janelia Research Campus, thanks to a grant awarded through the Advanced Imaging Center. Cells were chosen for imaging based on their brightness in the 750 nm channel (Gag) and their morphology, assessed by differential interference contrast (DIC). Ideal cells had large areas of flat lamella and bright 750 nm fluorescence indicative of abundant labeled Gag. Once a cell was selected, the microscope was left to “de-drift” for several minutes before imaging to prevent excessive drifting of the sample or the objectives during image acquisition, as even nanometer-scale drift would be detectable at this resolution. Cells were then imaged in each fluorescence channel sequentially, starting at the longest wavelength (750 nm) and ending with the shortest (488 nm), to avoid bleaching by higher energy wavelengths of un-acquired channels. Imaging was done in total internal reflection mode (TIRF) to minimize background fluorescence from out-of-focus signal. However, the ventral and dorsal surfaces of lamella were often still visible, increasing the number of assembly sites visible in our images. For each channel 40,000 – 60,000 frames were collected on the three electron-multiplying charge coupled device (EM-CCD) cameras. The AF750 (Gag) was excited with a 750 nm laser at $\sim 2 \text{ kW cm}^{-2}$, at exposure times of 50 – 75 ms. Emitted light was filtered through a 795/50 emission filter (Chroma Technology, Bellows Falls, VT). The AF647 (Env) channel was excited with a 640 nm laser at $\sim 3 \text{ kW cm}^{-2}$ at exposure times of 20 – 30 ms. The psCFP2 (membrane) channel was excited with a 488 nm laser at $\sim 0.4 \text{ kW cm}^{-2}$ at exposure times of 50 ms. The 640 and 488 nm channels were both filtered as described in van Engelenburg et al, 2014.

Superresolved images were derived by point localization and interferometry of image stacks using the Peak Selector software developed for this purpose (Betzig, 2005; Shtengel et al, 2009). Any drift of the sample or the objective was assessed by tracking movement of the fixed gold fiducial markers throughout the acquired frames, and was computationally corrected. Peaks localized with an uncertainty greater than 40 nm in the X- and Y-dimensions or greater than 30 nm in the axial Z-dimension were discarded (Figure 2.3). The three channels were then aligned to

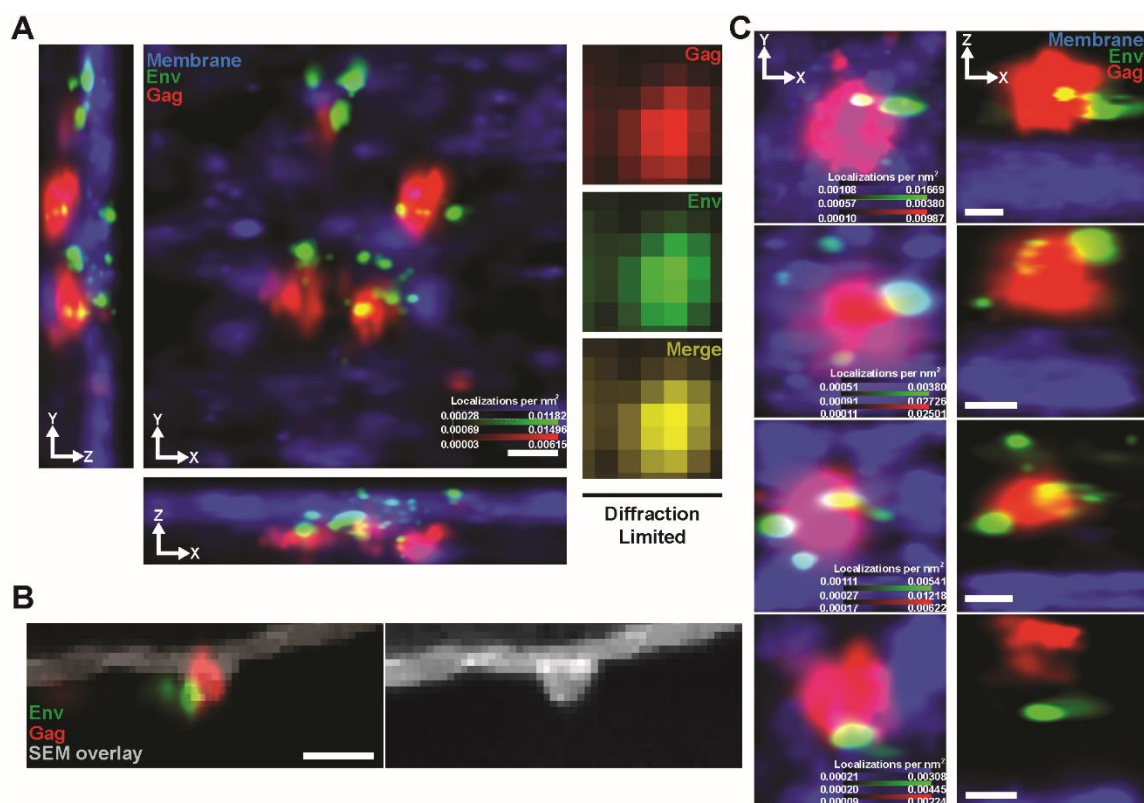


Figure 2.5. Three color iPALM enables visualization of single HIV-1 assembly sites and resolution of Env clusters on a sub-viral spatial scale. (A) Three-dimensional superresolution imaging is able to resolve four closely clustered virus assembly sites (Gag, red) protruding from the host cell plasma membrane (blue), and is able to resolve individual Env clusters (green) at each assembly site. Center image is an X,Y projection. Left and below are Y,Z and X,Z projections, respectively, of the same field. Scale bar is 100 nm. To the right, a diffraction limited rendering of the same X,Y field of view fails to resolve individual assembly sites. Pixel size is 133 nm. **(B)** Correlative iPALM (green, red) and scanning electron microscopy (SEM, grayscale) imaging confirm that Gag clusters (red) correspond to protruding membrane bud structures seen by SEM. Scale bar is 100 nm. **(C)** Representative examples of segmented assembly sites, displayed as top-down X,Y projections (left) and side-on X,Z projections (right). Scale bars are 100 nm.

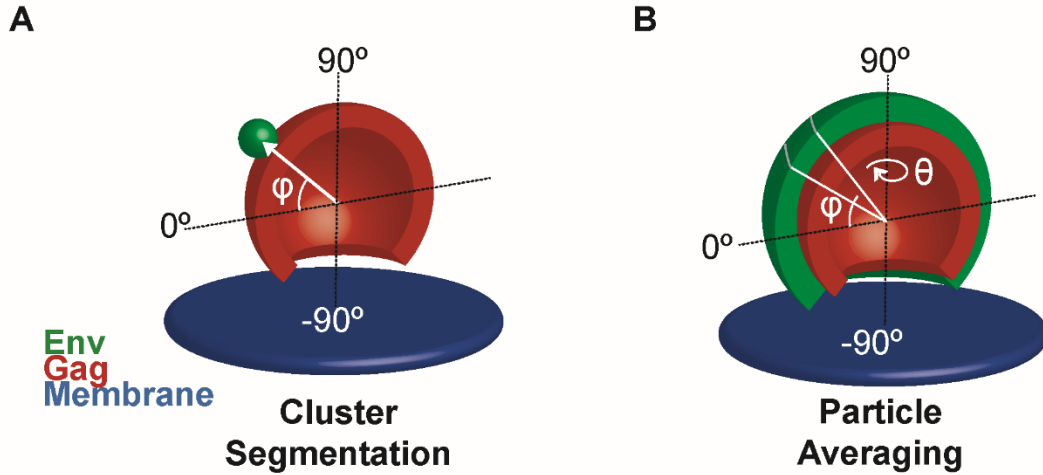


Figure 2.6. Diagram representations of the two orthogonal methods of analysis used to quantify Env angular distributions. (A) Individual clusters of Env signal were segmented and the elevation angle ϕ of the cluster's centroid was calculated relative to the equatorial angle $\phi = 0^\circ$, the angle perpendicular to the budding axis and which passes through the Gag centroid. **(B)** The integrated probability density of all aligned particles was summed about the azimuthal angle θ and along the radius of each elevation angle ϕ relative to the equatorial angle $\phi = 0^\circ$.

each other by transforming the localizations from the fluorescent gold nanorods in the 750 and 488 nm channels onto the corresponding localizations in the 640 nm channel (Figure 2.4).

Individual particle assembly sites were segmented by manual cropping in the X-, Y- dimensions (Figure 2.5; van Engelenburg et al, 2014). Particles were not segmented if they had no associated Env localizations, if they or their associated Env clusters were not resolvable from nearby particles, if the local plasma membrane was not sufficiently well sampled to define the particle's budding axis, or if the particles were directly beneath the cell nucleus, the refractive index of which distorts the interferometric pattern by altering the velocity of the upper light path. These cropped images were written as individual ASCII files.

The biological sparsity of Env clusters on virus particles made it necessary for us to achieve the statistical power to make quantitative claims about Env distributions by imaging many individual assembly sites and measuring overall average distributions. We designed two orthogonal methods for analyzing these distributions to control for the shortcomings of each. First, individual Env clusters were segmented using 3D convolution with a template based on seed parameters derived from experimental data, and the angular position of each segmented cluster was measured (Figure 2.6A). This method allowed us to quantify the statistical characteristics of the distribution, most importantly mean and skewness, but the convolution algorithms used to segment the clusters were occasionally unable to detect clusters and those that were segmented had to be manually confirmed to be real clusters: both potential sources of selection bias. To control for this potential bias, a second, orthogonal analysis method was employed, adapting the technique of single particle averaging, which is common in cryo electron microscopy and has been used previously in iPALM (van Engelenburg et al, 2014). In iPALM imaging, this method was applied to HIV-1 assembly sites, aligning symmetrical structures translationally and summing all localizations into a composite volume to improve sampling. For our applications, we needed to align assembly sites not only translationally, but also rotationally which we were able to do using the budding axis of each individual particle. The probability density of Env in the resulting composite volume was then summed about the azimuthal angle and along the radius at each

degree of the elevation angle ϕ to plot a distribution of Env probability from the assembly site crown to its neck (Figure 2.6B). This method accounted for all Env localization at the segmented assembly sites, so it avoided the potential for selection bias, but it is not as easily quantified and has the potential to be skewed by any spurious signal such as coverslip noise or non-specifically bound antibodies that were not excluded during sample preparation and data processing. The results of both analysis methods were compared against each other as controls for the potential sources of error associated with each.

Custom MATLAB code was written to process segmented assembly sites and to apply both analysis methods described above. First, all assembly sets from each individual experiment of the same conditions (genotype and cell type) were combined into a single dataset and a module of code was applied to identify “ghost” signals which had been miss-assigned by astigmatism to the wrong interferometric period and to re-assign them to the correct one. During this step, the segmented 2D images were viewed in 3D, and any segmented assembly sites that were found to have inadequate membrane sampling, multiple assembly sites in the Z-dimension, Env clusters that were not truly associated with the assembly site, or a distance from the membrane which suggested the particle may be released, were discarded. This was typically ~15 – 50% of the segmented sites from each cell. Localizations were filtered by proximity to the Gag localization cluster to avoid inclusion of cover slip noise. The cluster of Gag localizations was least-squares-fit to the model of a spherical shell to identify the cluster centroid for translational alignment of particles and as a reference for angular measurements. Assembly sites that were not sufficiently well sampled in the Gag channel and were fit poorly to the shell model were discarded. This was typically no more than ~5% of the segmented assembly sites. A plane was then fit to the plasma membrane localizations of each segmented assembly site using principal component analysis (PCA). The normal vector of the fitted plane was used to define the budding axis of the particle (Figure 2.7). The distance between the Gag centroid and the mean point of the membrane signal was measured as the particle’s neck length and used to confirm that the distribution of neck lengths agreed with those measured by electron microscopy, suggesting they

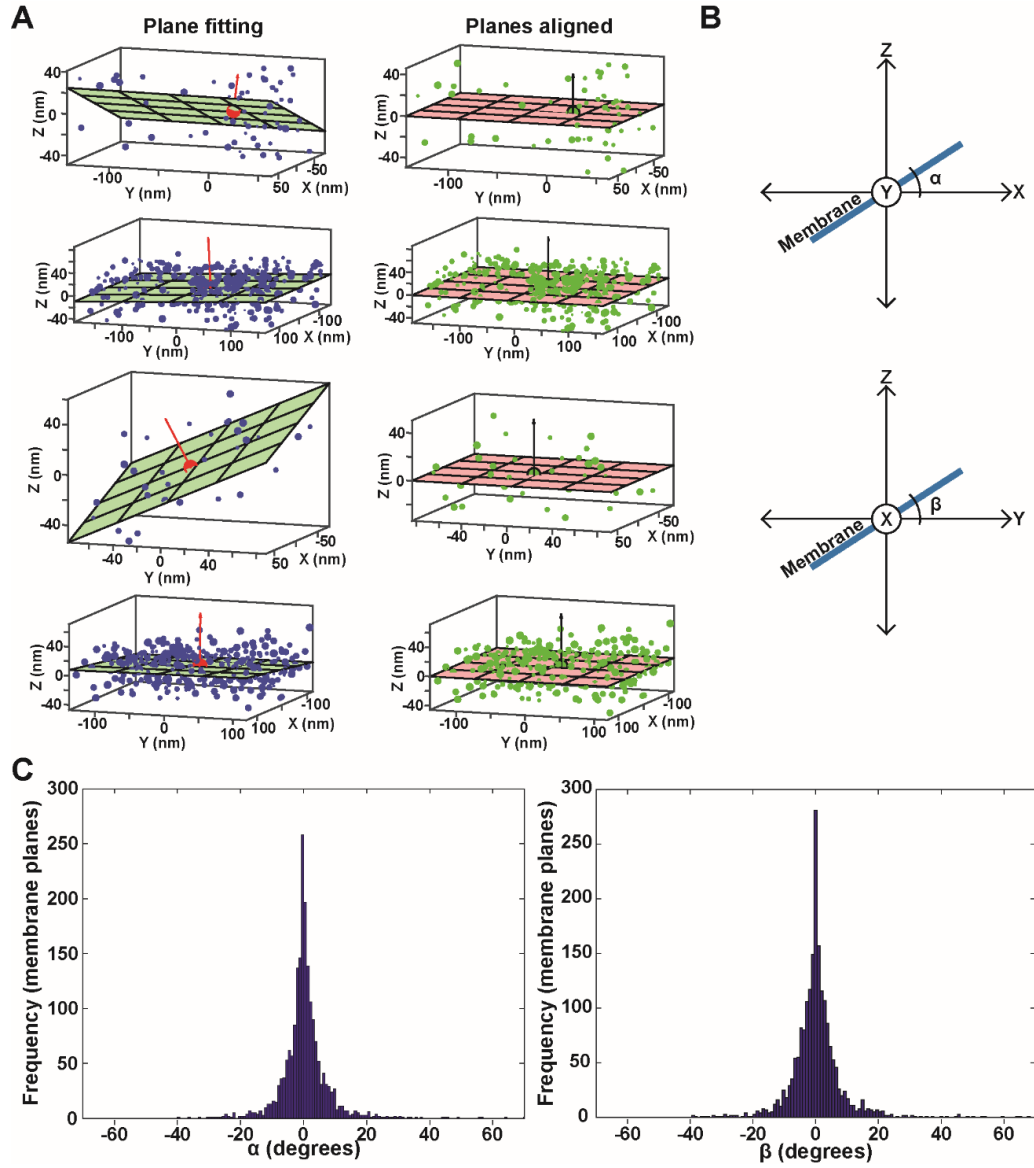


Figure 2.7. Weighted principal component analysis (PCA) was used to fit a plane to the local plasma membrane at each viral assembly site. (A) Representative examples of local membrane signals at segmented assembly sites, which were fit to a plane (green, left) with a normal vector (red, left) describing the budding axis of the associated particle. Planes were then aligned (pink, right) by aligning the normal vector along the optical axis Z (black, right). **(B)** Diagrams defining the angles α and β as the X- and Y-dimension components, respectively, of the membrane plane tilt. **(C)** The α (left) and β (right) angles for the planes fitted to each segmented assembly site's local plasma membrane.

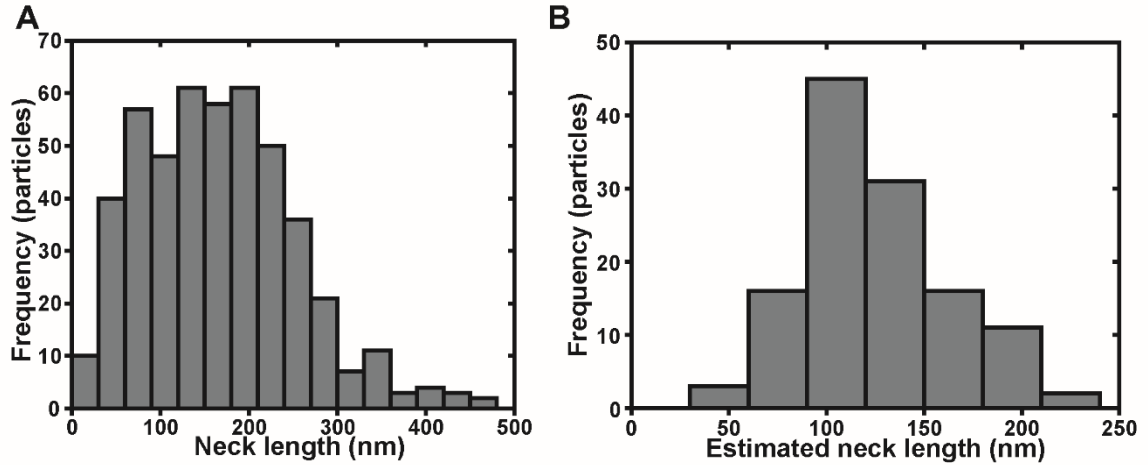


Figure 2.8. The measured neck lengths of budding virus assembly sites imaged by iPALM agree with those measured by transmission electron microscopy. (A) A histogram representation of budding virus particle neck lengths from a representative dataset. Neck length was measured as the distance along the budding axis between the Gag centroid and the local membrane centroid. For this dataset, the mean neck length was 165 ± 86 nm (standard deviation, $n = 474$ assembly sites). For all datasets, the mean neck length was 150 ± 92 nm (standard deviation, $n = 1837$ assembly sites). **(B)** A histogram representation of the estimated neck lengths of budding virus particles seen by TEM. Neck lengths were manually traced from the approximate centroid of dense Gag signal to the approximate plasma membrane plane on particles that appeared to be sectioned along the budding axis (see Figure 2.21). The mean neck length was measured to be 127 ± 38 nm (standard deviation, $n = 124$ assembly sites).

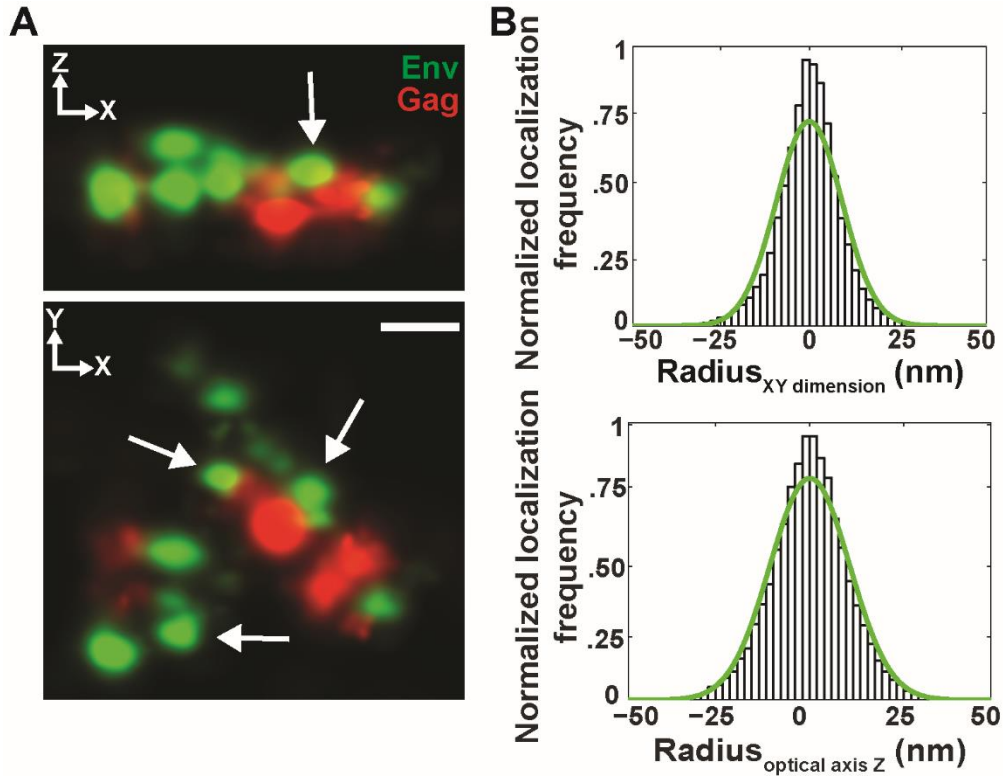


Figure 2.9. Estimated geometric characteristics of Env clusters were used to generate template Env clusters for simulation and for single cluster segmentation. (A) iPALM images of Env clusters (green, white arrows) at Gag assembly sites (red) in COS7 cells. Below is an X,Y projected image, and above, an X,Z projection of the same field. Scale bar is 100 nm. **(B)** Distributions of Env localization probability for Env clusters from 400 assembly sites in the X- and Y-dimensions (above) and in the Z-dimension (below). Standard deviations of the gaussian functions (green) fit to the distributions were 9.3 nm in X,Y and 11 nm in Z.

are indeed cell-associated and un-released (Figure 2.8). For display purposes, neck lengths were then normalized to 200 nm.

Individual particles were aligned with each other translationally at their Gag centroids and rotationally along their budding axes. In order to measure the angular positions of individual Env signal clusters, an algorithm for segmentation of single clusters was written. The localization coordinates and uncertainties from point localization and interferometric localization were used to convert the Env channel of each segmented particle from a point cloud into a 3D probability density and a template Env cluster, based on seed parameters from experimental data (Figure 2.9), was convolved against the Env probability density to identify Env clusters. This was repeated three times for each virus particle to ensure that most clusters were found, and the centroids of the identified Env clusters were calculated. The process was supervised by manual inspection of the results; the calculated centroids were mapped to the point cloud of each virus particle, and the Env cluster centroids identified by the convolution algorithm were either accepted or rejected. Centroids within a cluster's radius of a previously accepted cluster were considered to be the same cluster, and were not counted again. The accepted centroids' angular positions relative to the Gag centroid and budding axis were then measured. By setting the equatorial elevation angle (perpendicular to the budding axis and passing through the Gag centroid) as elevation angle $\phi = 0^\circ$, we defined the crowns of the particles (the northern hemispheres) as all positive angles 0 through 90° and the necks of the particles (the southern hemispheres) as all negative angle 0 through -90° . The measured elevation angles of the individual Env clusters were plotted as histograms to visualize their distribution, and their statistical characteristics were used to quantify that distribution.

The orthogonal method of analysis, which mapped the distribution of all Env localizations, was done by single particle averaging of the aligned segmented particles. Each particle was converted into a 3D probability density and the individual particles from each condition were then integrated into a single probability density map. These probability density volumes were trimmed to $601 \times 601 \times 601$ nm cubes, centered around the Gag centroid. The probability density of Env for

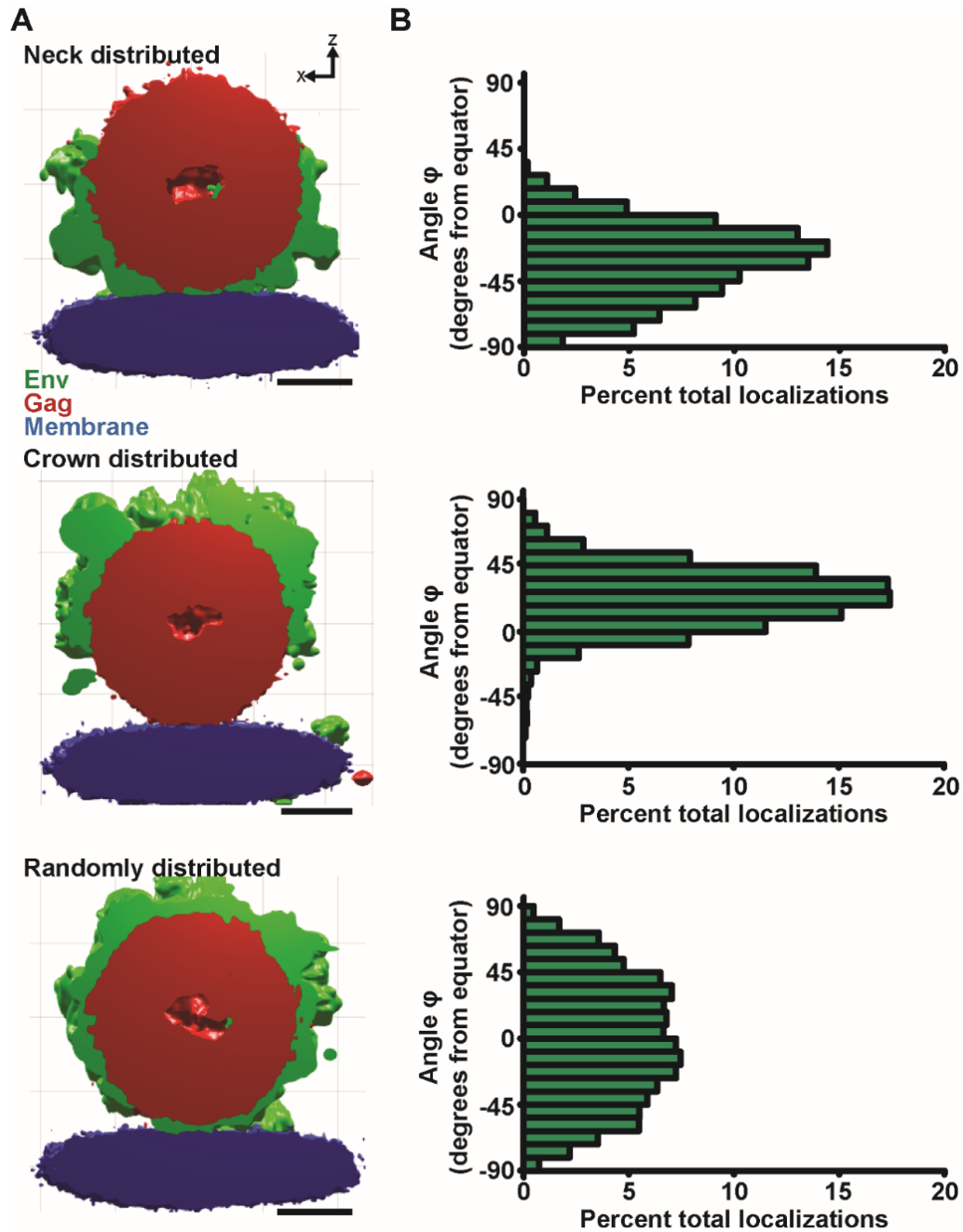


Figure 2.10. Simulated budding particles demonstrate the particle averaging method of Env distribution analysis. Simulated datasets were generated with biased distributions of Env, using seed parameters from biological datasets. These datasets were processed through our custom software, and the biased distributions were reconstructed as expected. Simulated dataset generated with a neck-biased distribution centered at $\phi = -45^\circ$ (top), with a crown-biased distribution centered at 45° (middle), and with a random distribution of Env clusters (bottom). **(A)** Cuts of rendered probability density volumes. **(B)** Histogram representations of Env distributions in ϕ , binned in 9° increments. Scale bars are 100 nm.

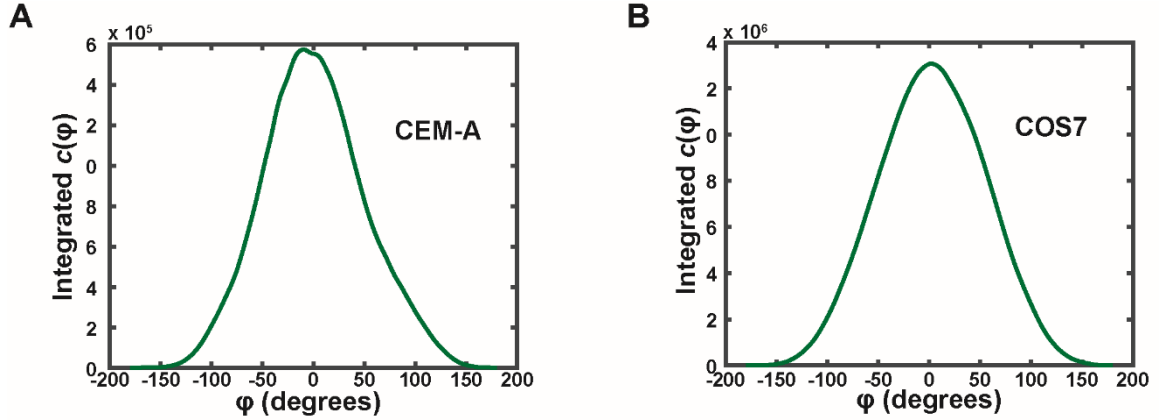


Figure 2.11. Phase correlation of the angular (ϕ) probability density of Env between random half-datasets estimates the sampling resolution of Env. We estimated the sampling resolution of Env in our system along the elevation angle ϕ by phase correlation of the final mapped probability densities of randomly divided half-datasets for each condition. The wild type (WT) datasets from each cell type are shown as representative examples. **(A)** For CEM-A cells producing WT-Env, the lag between perfect correlation (0°) and maximum correlation was -20° ($n = 265$ assembly sites). **(B)** For COS7 cells producing WT-Env, lag = 2° ($n = 454$ assembly sites). The mean of the absolute values for all datasets was lag = 9° .

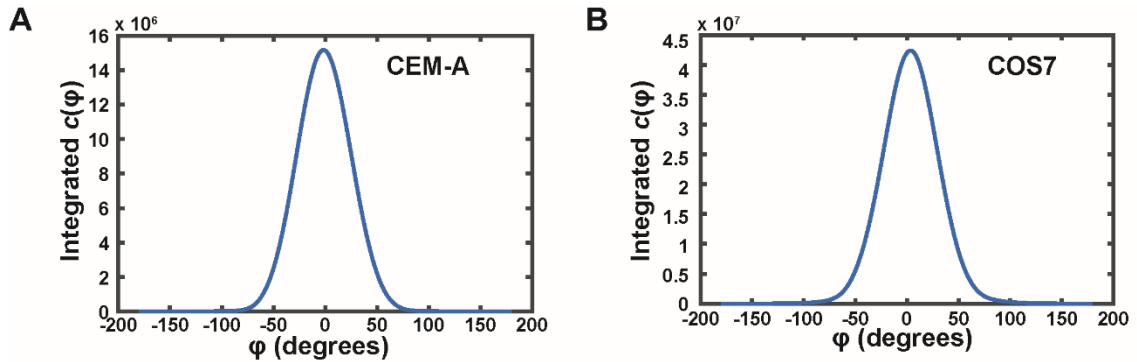


Figure 2.12. Phase correlation of the probability density of plasma membrane between random half-datasets estimates alignment error. **(A)** For CEM-A cells producing WT-Env, lag = 2° ($n = 265$ planes). **(B)** For COS7 cells producing WT-Env, lag = 3° ($n = 454$ planes). The maximum lag for all datasets was 3° .

each cube was integrated about the azimuthal angle θ to collapse the 3D map into a 2D map, and then along the radius of each elevation angle ϕ (Figure 2.6B), to map the angular probability of Env localization in a single dimension. Simulated datasets were generated to test this method, with imposed biases in angular distribution of Env channel signal that were easily detected (Figure 2.10).

In order to assess the error in this experimental system, we employed several orthogonal methods of both indirect measurement and error simulation. First, we assessed the potential for sampling uncertainty (the uncertainty in our measurements due to under-sampling the elevation angle) in the Env channel by phase correlation of randomly divided half-datasets of each condition's full dataset (Figure 2.11). Given the known biological sparsity of Env on particles, this uncertainty is a significant concern, which we hoped to minimize by analysis of many assembly sites. We found that the average lag between the half-dataset correlation was 9° . With this uncertainty in sampling of the Env distribution, we are still easily able to distinguish between our hypothesized results (Figure 1.2).

Next, we used phase correlation along the elevation angle ϕ of the membrane channel to assess error in the rotational alignment of particles (Figure 2.12). This resulted in no greater than 3° of lag. However, to support this indirect assessment, we also generated a simulated dataset based on seed parameters from our experimental data (Figure 2.13). The gag shell, local membrane, and Env were simulated as a point cloud, with Env localized as a single point at the equatorial angle $\phi = 0^\circ$. The points in all channels were assigned localization uncertainties from a normal distribution matching the experimental localization uncertainties (Figure 2.3). The points of each channel were then randomly displaced based on the experimental uncertainty in channel registration (Figure 2.4). Points in the Gag channel were displaced according to the uncertainty of the least-squares shell fitting (Figure 2.14). The membrane was simulated as a Gaussian disc according to the measured characteristics of plane-fitted membranes to simulate error in the PCA plane fitting (Figure 2.15). To simulate biological differences in budding axes relative to the microscope, the membrane and Env channels were rotated together about the Gag centroid. The

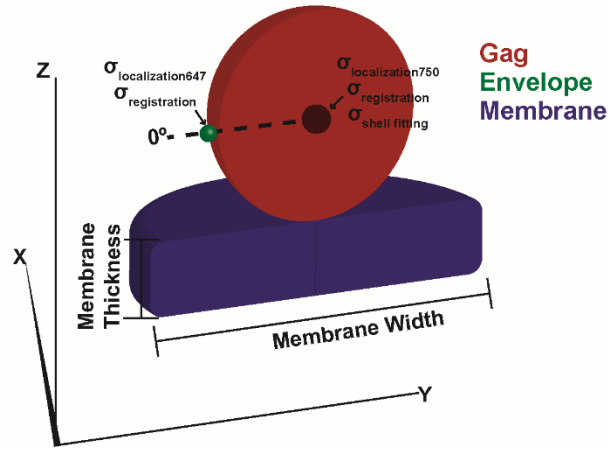


Figure 2.13. Diagram describing simulation of error in rotational alignment of assembling viral particles. Gag clusters were generated with a random radius sampled from a distribution derived from the fit in Figure 2.14 (red sphere). Membrane planes were randomly simulated using seed parameters and variance from the fits seen in Figure 2.15 (blue). Membrane planes were randomly offset from the Gag centroid based on the distribution of neck lengths (Figure 2.8). Each particle was generated with a single Env localization (green) at a fixed equatorial angle $\varphi = 0^\circ$. All three channels were rotated about the Gag centroid at random angles of α and β (see Figure 2.7). Localization precisions were assigned for each point based on the distributions of σ for each fluorophore (see Figure 2.3). Channels were offset from each other based on the distribution of registration uncertainties (see Figure 2.4).

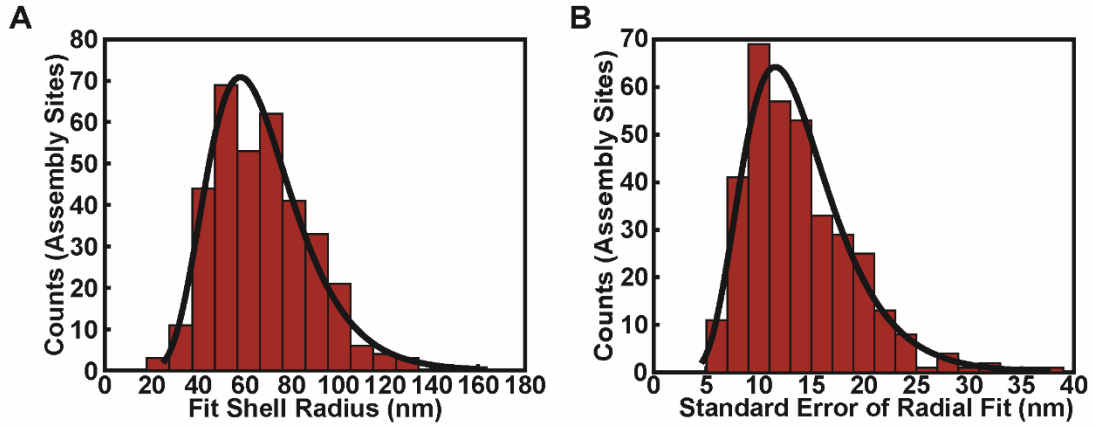


Figure 2.14. Radius and residual error of Gag shell fitting for a representative dataset. (A) Distribution of the radius of shells fit to a random set of 350 segmented Gag clusters. The mean radius of this dataset was 70 ± 22 nm (standard deviation). **(B)** Distribution of the fit uncertainty for the same representative set. The mean uncertainty was 13.9 ± 5.1 nm (standard deviation). This was used as an estimate of uncertainty in translational alignment of assembly sites.

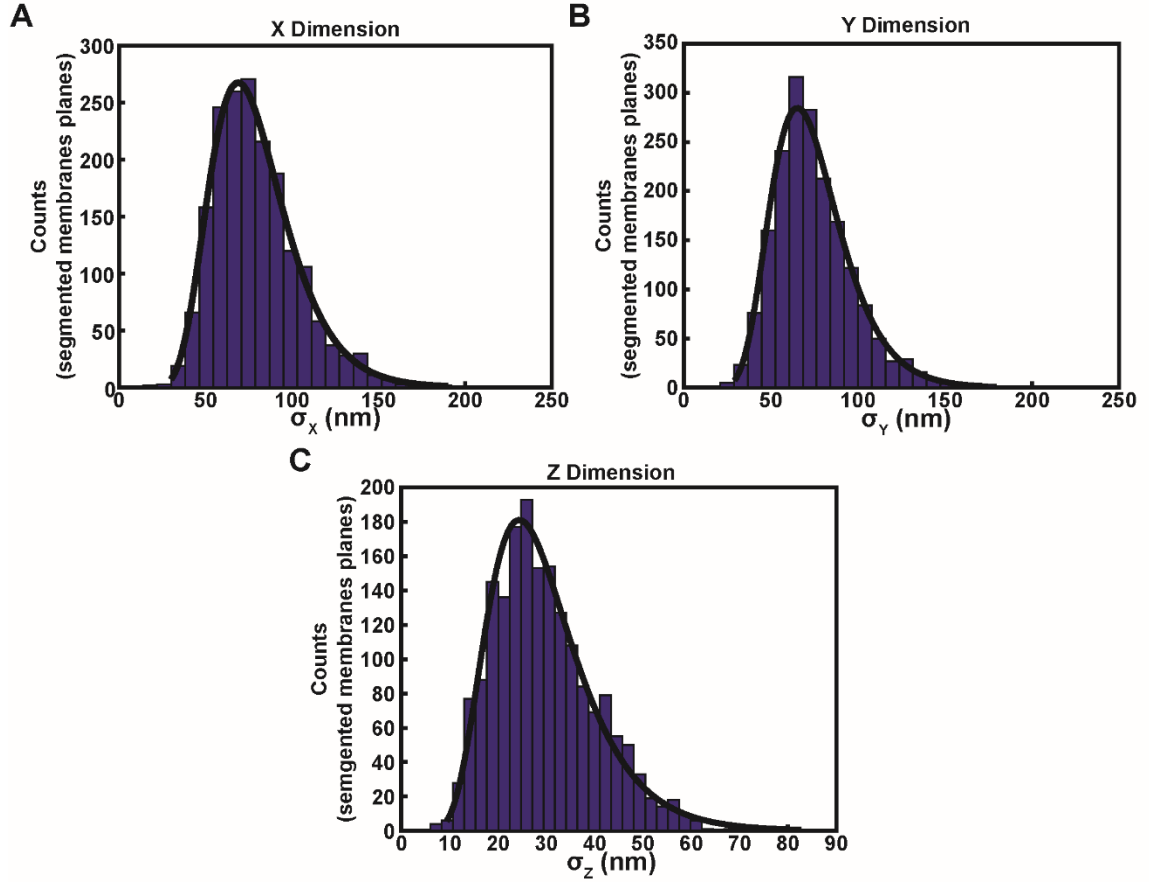


Figure 2.15. Geometric characteristics of aligned segmented plasma membranes. (A) Distribution of the standard deviations of localization positions in the X-dimension. The mean value = 79.3 ± 25.0 nm (standard deviation, $n = 1837$ segmented plasma membrane planes). **(B)** Distribution of the standard deviations of localization positions in the Y-dimension. The mean value = 74.51 ± 22.7 nm (standard deviation, $n = 1837$). **(C)** Distribution of the standard deviations of localization positions in the Z-dimensions, describing membrane signal thickness. The mean value = 29.72 ± 11.2 nm (standard deviation, $n = 1837$).

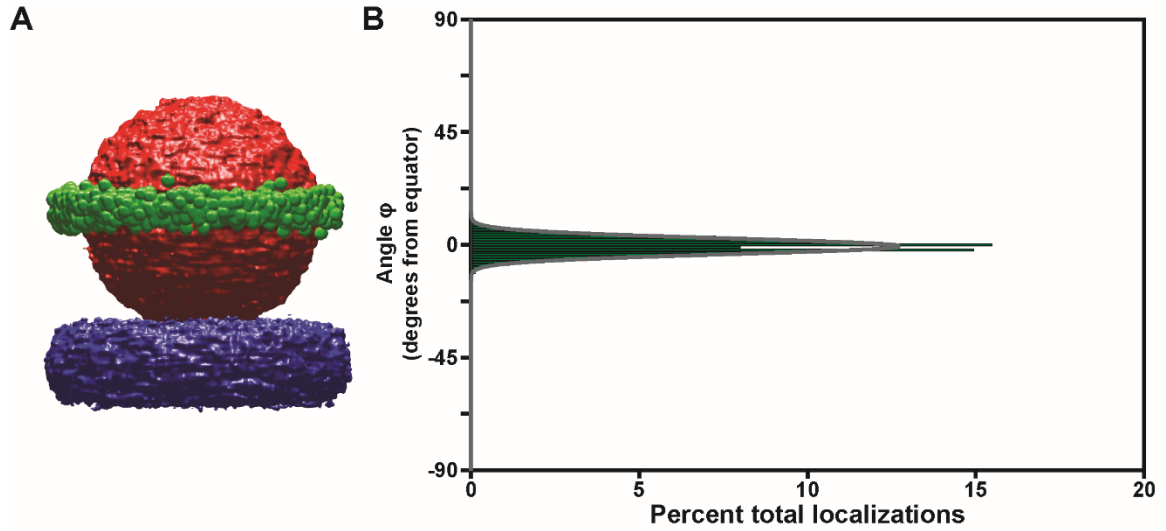


Figure 2.16. Results of simulated error in rotational alignment of assembly sites. A dataset of 2500 assembly sites was simulated as described in Figure 2.13, with ground truth Env angular positions of 0° only. These assembly sites were processed through our custom software to assess potential error in rotational alignment. **(A)** The probability density resulting from particle averaging was isosurfaced with thresholds 0.1 (Gag, red), 0.0001 (Env, green), and 0.15 (plasma membrane, blue). **(B)** An un-binned histogram representation of Env signal at each elevation angle ϕ . Fit to a Gaussian distribution (gray), this resulted in a standard deviation of $4.39 \pm 0.12^\circ$ (standard error), which estimates the error in rotational alignment.

membrane points were then displaced according to the measured neck lengths of experimental data (Figure 2.8). The simulated dataset of 2500 particles was then processed normally through our custom MATLAB modules and its probability distribution was mapped (Figure 2.16). The standard deviation of the Env ϕ distribution, estimating the uncertainty in our experimental angular measurements, was found to be 4.39° , with a standard error of 0.12° . As the most conservative value, the 9° uncertainty in Env distribution sampling was used to bin distribution histograms, but all uncertainty remained well below the scale of the hemispheric analysis required to distinguish our models.

Additionally, all errors of the imaging and data processing system were used to estimate the overall resolution of our system in the X-, Y-, and Z-dimensions. Independent errors must be added in quadrature, so the total resolution of our system was estimated by Equation 1.

Equation 1.

$$\sigma_{\text{total}} = \sqrt{\sigma_{\text{drift}}^2 + \sigma_{\text{registration}}^2 + \sigma_{\text{AF750}}^2 + \sigma_{\text{AF647}}^2 + \sigma_{\text{psCFP2}}^2 + \sigma_{\text{averaging, translational}}^2 + \sigma_{\text{averaging, rotational}}^2}$$

Physical drift varied but was typically measured to be 5 – 50 nm. The uncertainty in the computational correction of this drift (Shtengel et al, 2009) was typically between 1 and 5 nm (σ_{drift}). The uncertainty in the registration of the three channels to each other ranged from 3 to 8 nm ($\sigma_{\text{registration}}$). The mean localization uncertainty of AF750 was 10 – 15 nm in X- and Y-dimensions, and 5 – 12 nm in the Z-dimension (σ_{AF750}). The mean localization uncertainty of AF647 was 5 – 10 nm in X- and Y-dimensions, and 3 – 8 nm in the Z-dimension (σ_{AF647}). The mean localization uncertainty of psCFP2 was 10 – 20 nm in X- and Y-dimensions, and 10 – 15 nm in the Z-dimension (σ_{psCFP2}). The uncertainty in alignment of Gag centroids was less than 5 nm ($\sigma_{\text{averaging, translational}}$), and the residual uncertainty of rotational alignment was estimated to be 3 – 5° , or about 10 nm in Euclidean space. Based on these values, we estimated the total resolution of our imaging system to be approximately 33.5 nm (σ_{total}).

In CEM-A cells, the overall distribution of Env clusters was found to be biased toward the necks of assembling particles (Figure 2.17A). By measuring the individual angular positions of single Env clusters, we calculated a mean ϕ value of $-17.13 \pm 2.019^\circ$ (standard error, $n = 338$

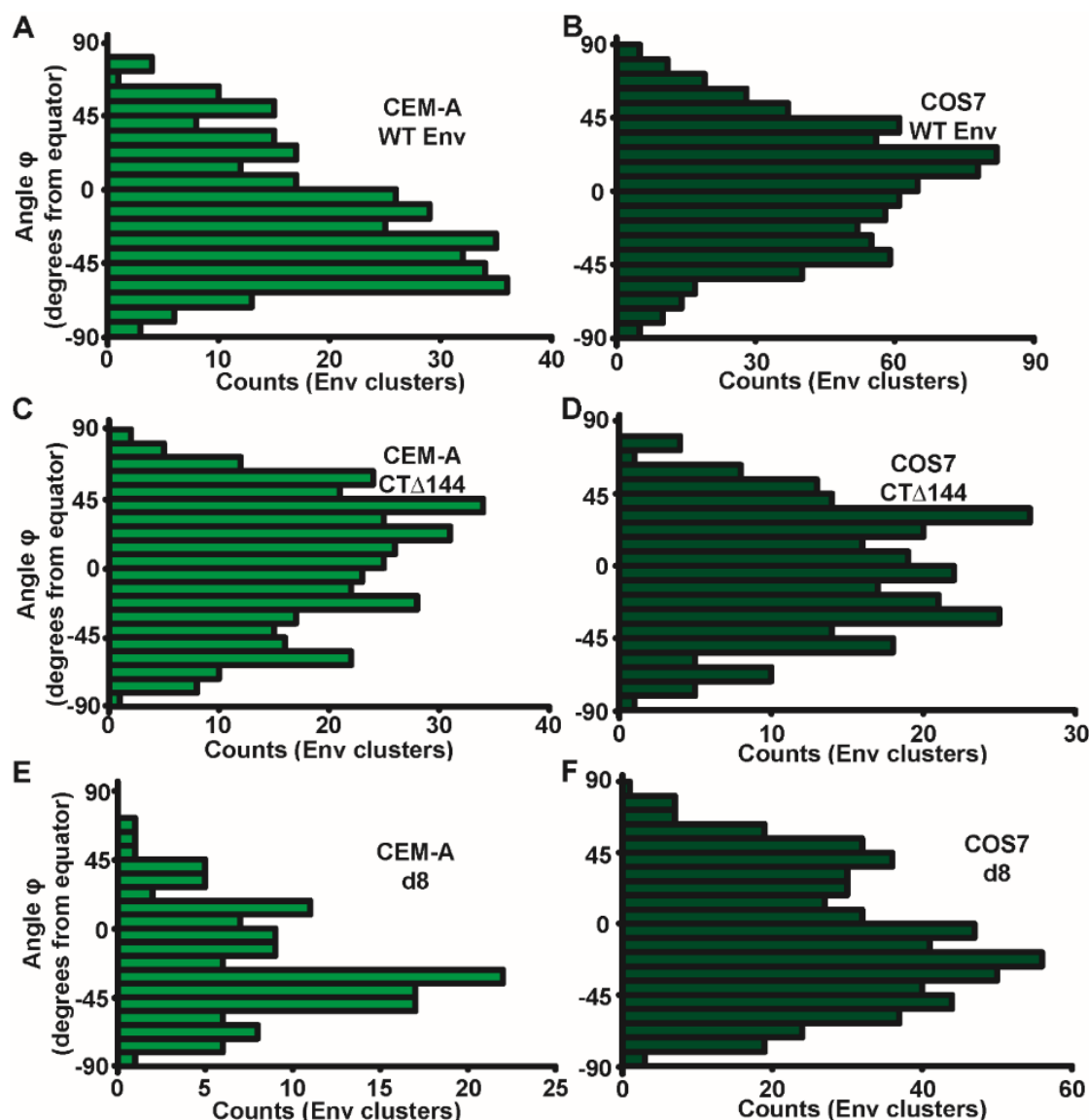


Figure 2.17. Angular distributions of Env measured by segmentation of individual Env clusters. Individual Env clusters were segmented using 3D convolution and template matching, and the elevation angle ϕ of each cluster centroid was calculated (see Figure 2.6A). Distributions of ϕ were binned in 9° increments according to the sampling resolution estimated in Figure 2.11. **(A)** Distributions of wild type Env (WT-Env) are biased toward the necks of particles produced in CEM-A cells ($n = 338$ clusters on 265 particles from 3 cells). **(B)** Distribution of WT-Env is unbiased on particles produced in COS7 cells ($n = 813$ clusters on 454 particles from 5 cells). **(C)** Unbiased distribution of CT Δ 144-Env on particles produced in CEM-A cells ($n = 367$ clusters on 276 particles from 4 cells). **(D)** Unbiased distribution of CT Δ 144-Env on particles produced in COS7 cells ($n = 260$ clusters on 244 particles from 3 cells). **(E)** Neck-biased distribution of d8-Env on particles produced in CEM-A cells ($n = 134$ clusters on 124 particles from 4 cells). **(F)** Neck-biased distribution of d8-Env on particles produced in COS7 cells ($n = 582$ clusters on 474 particles from 4 cells).

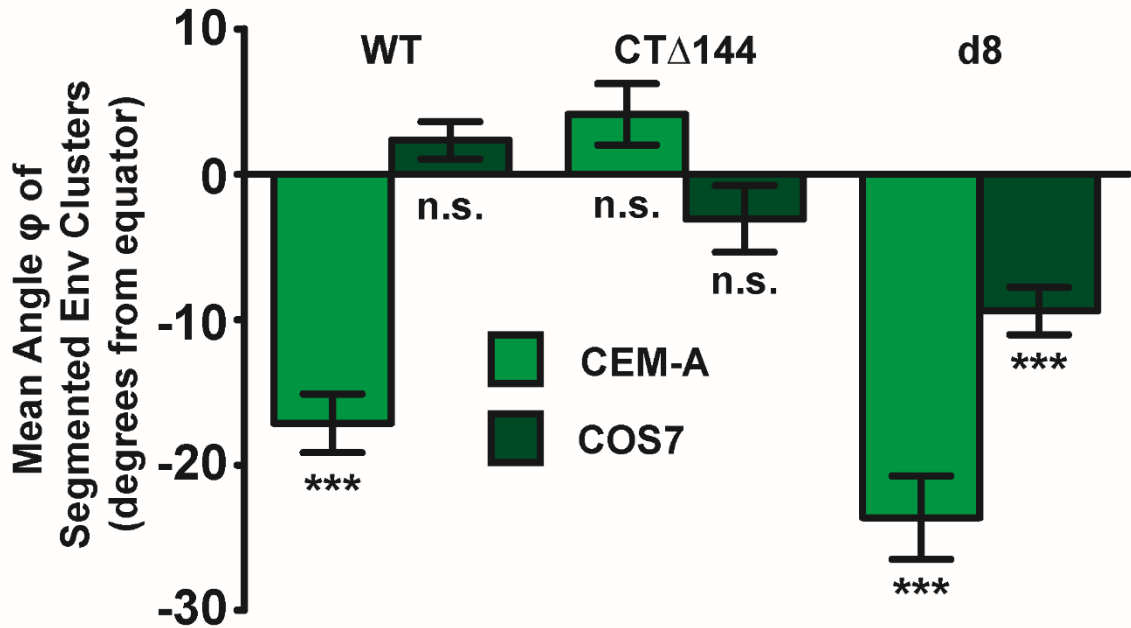


Figure 2.18. The mean ϕ value of individually segmented Env clusters describes the overall distribution bias. The statistical characteristics, particularly the mean, of the distribution of ϕ values measured explicitly for individual segmented Env clusters (see Figure 2.6A) was used to quantify angular bias, with negative ϕ values corresponding to neck-biased distributions and positive ϕ values corresponding to crown-biased distributions. Error bars indicate standard error. The mean value for each dataset was tested for significant difference from the theoretical unbiased mean value of 0° . *** indicates $P < 0.0001$ and n.s. indicates not significant by two-way ANOVA and Bonferroni post-test.

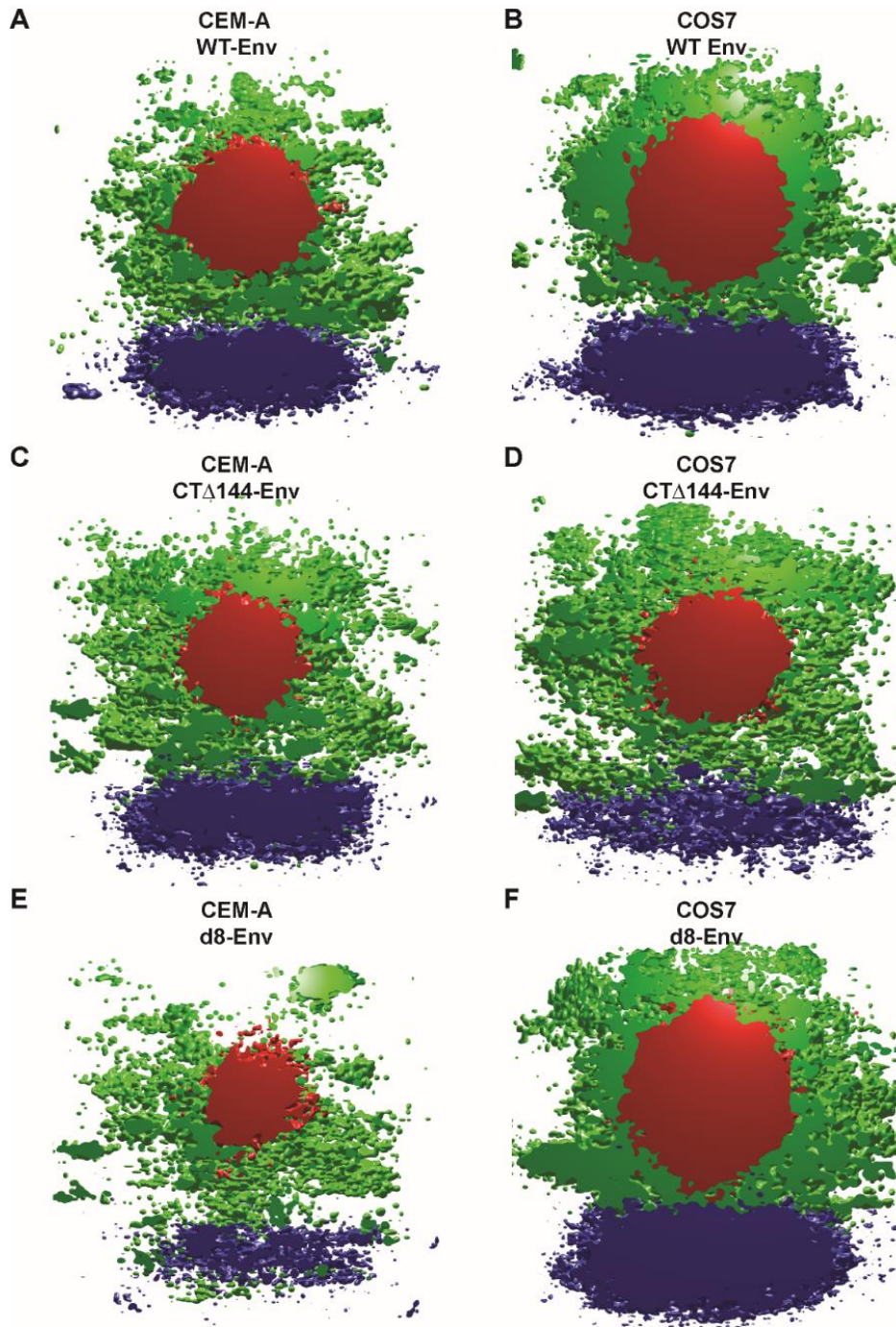


Figure 2.19. Cross-section probability density volumes of aligned assembly sites show Env angular biases. All volumes were isosurfaced at thresholds of 0.003 (Gag, red), 0.001 (Env, green), and 0.0045 (plasma membrane, blue) localizations nm^{-3} . **(A)** WT-Env produced in CEM-A cells ($n = 265$ assembly sites from 4 cells). **(B)** WT-Env produced in COS7 cells ($n = 454$ assembly sites from 5 cells). **(C)** CT Δ 144-Env produced in CEM-A cells ($n = 276$ assembly sites from 4 cells). **(D)** CT Δ 144-Env produced in COS7 cells ($n = 244$ assembly sites from 3 cells). **(E)** d8-Env produced in CEM-A cells ($n = 124$ assembly sites from 4 cells). **(F)** d8-Env produced in COS7 cells ($n = 474$ assembly sites from 4 cells).

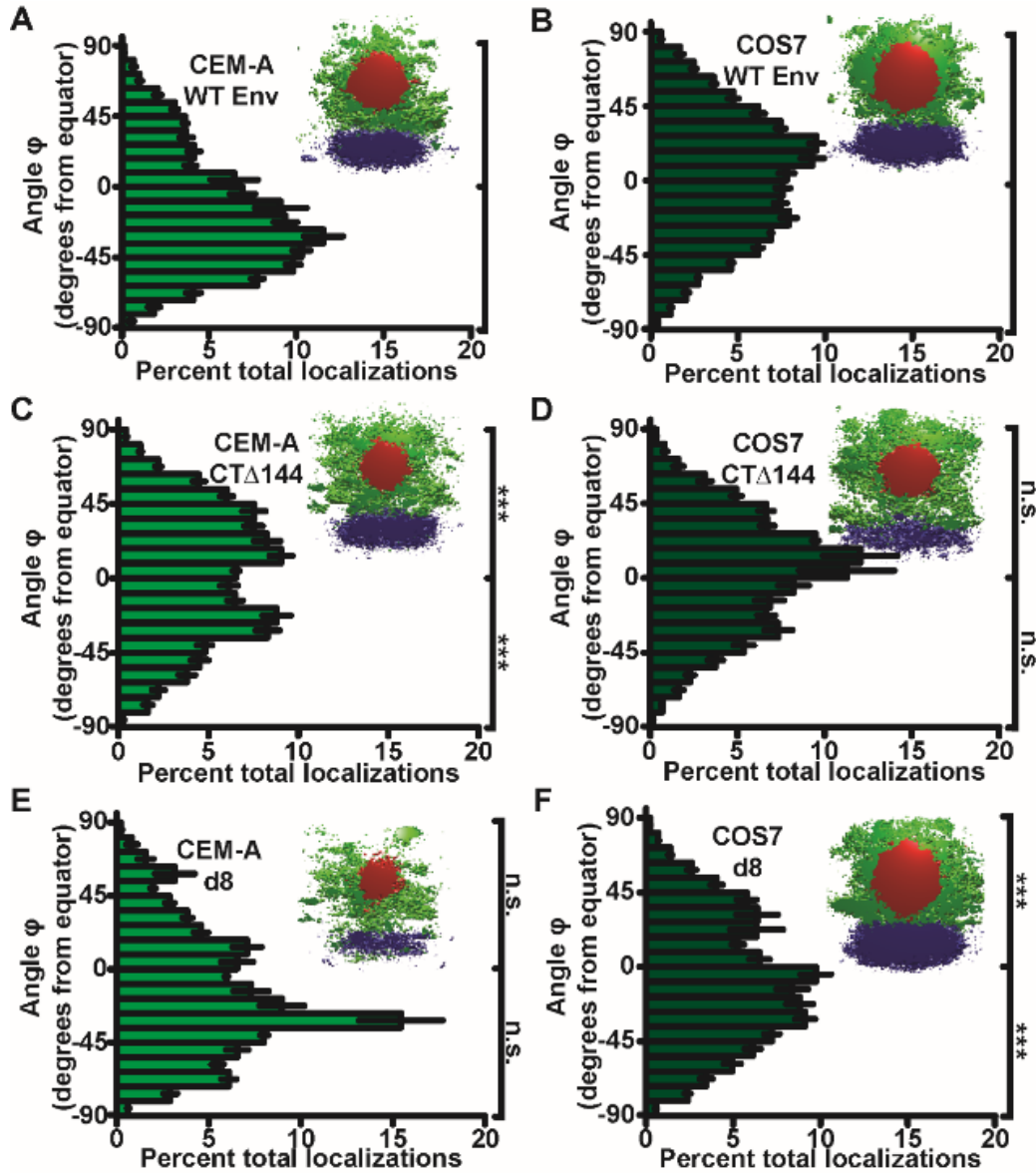


Figure 2.20. Distributions of angular probability densities by particle averaging. Probability densities of Env for all aligned particles from each dataset were integrated along the cone representing each elevation angle ϕ (see Figure 2.6B). Histograms were binned in 9° increments as in Figure 2.17. Probability density was normalized as a percentage of the total probability in each dataset. **(A)** The distribution of WT-Env is biased toward the necks of particles produced in CEM-A cells. **(B)** Unbiased distribution of WT-Env on particles produced in COS7 cells. **(C)** Unbiased distribution of CT Δ 144-Env on particles produced in CEM-A cells. **(D)** Unbiased distribution of CT Δ 144-Env on particles produced in COS7 cells. **(E)** Neck-biased distribution of d8-Env on particles produced in CEM-A cells. **(F)** Neck-biased distribution of d8-Env on particles produced in COS7 cells. Error bars represent standard deviation of the means of three pairs of randomly divided half-datasets. Integrated probability of each hemisphere, with errors added in quadrature, were tested for significant difference from the WT-Env distributions for each cell type. *** indicates $P < 0.001$ and n.s. indicates not significant using two-way ANOVA and Bonferroni post-test.

clusters), with a skewness of 0.5227 (Figure 2.18). This result was supported by the single particle averaging method. The probability density of Env signal was clearly skewed toward the neck hemisphere of the composite volume (Figures 2.19A, 2.20A). This fits with the model proposed in (Figure 1.2B), wherein Env arrives at assembly sites late in the process of Gag lattice assembly and is therefore most often trapped toward the edges of the lattice and neck of the particle.

In COS7 cells, on the other hand, the distribution of Env clusters appeared to be unbiased (Figure 2.17B). The mean ϕ value of $2.338 \pm 1.280^\circ$ (standard error, $n = 813$) clusters did not significantly differ from the theoretical mean of 0° that would be expected of an unbiased distribution (Figure 2.18) and the skewness of -0.09703 suggests a relatively symmetrical distribution. Again, the single particle averaging analysis was in agreement with these results (Figures 2.19B, 2.20B). This fits with the model in (Figure 1.2C), which is explained either by Env incorporation throughout Gag lattice assembly or by Env not becoming trapped in the lattice, which would seem to be unlikely given the skewed distribution that was observed in CEM-A cells.

Interestingly, this suggests a cell type dependence of Env-Gag encounter timing. The most likely explanation for this cell type dependence is that there is a role in regulating timing for some host cell mechanism. This is supported by previous studies which examined the Env recycling pathway and suggested a role for the host cell factor FIP1C in regulating trafficking of Env between the intracellular recycling compartment and the plasma membrane (Qi et al, 2013; Qi et al, 2015; Kirschman et al, 2018).

Both experiments were then repeated with a mutant form of Env lacking the final 144 amino acids that comprise the long cytoplasmic tail (CT Δ 144). According to the previous studies that suggested that Env trapping in the Gag lattice is dependent on interaction between immature Gag and the Env cytoplasmic tail (Chojnacki et al, 2012; Roy et al, 2013; Chojnacki et al, 2017), we would expect that this mutant will not become fixed in the lattice, and will therefore fit the model in (Figure 1.2C), an unbiased distribution of Env about the particles. Indeed, in CEM-A cells CT Δ 144-Env clusters appeared to have an unbiased distribution by both the single particle

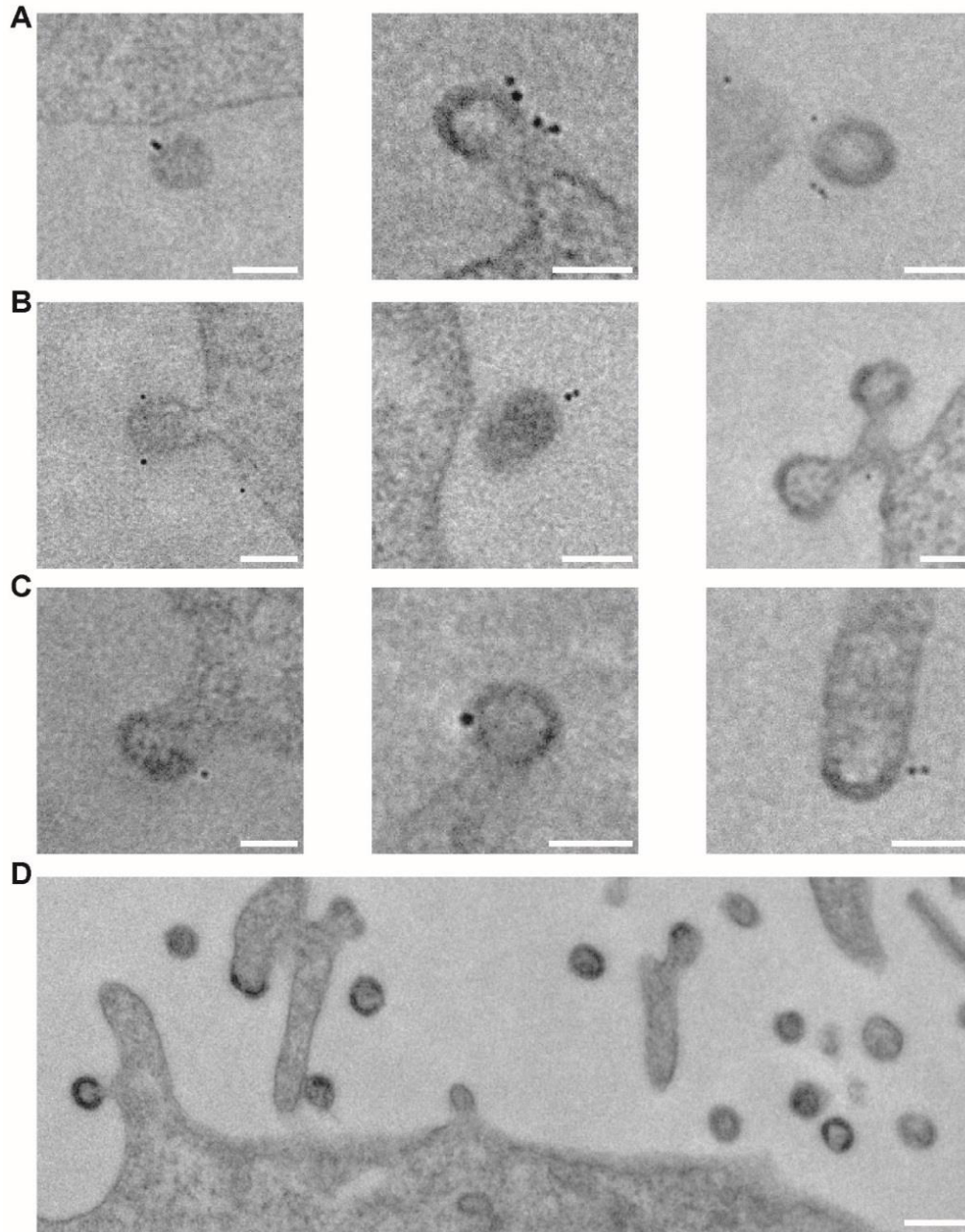


Figure 2.21. Immunogold labeling and transmission electron microscopy imaging of Env at assembly sites. Only assembly sites that were immunolabeled for Env and had visible necks are shown. Assembly sites on CEM-A cells producing **(A)** WT-, **(B)** CT Δ 144-, and **(C)** d8-Env. Less than 50% of visible Gag budding structures were labeled with gold and the vast majority of all budding structures were sectioned off axis, resulting in uncertain budding polarities. Scale bars are 100 nm. **(D)** As a control for non-specific immunolabeling, CEM-A cells were infected with Δ Env virus. No gold was observed in any fields of view from these experiments. Scale bar is 200 nm.

averaging method and by the cluster segmentation method (Figures 2.17C, 2.19C, 2.20C). This was supported by the measured mean ϕ value of $4.124 \pm 2.111^\circ$ (standard error, $n = 367$ clusters) and a skewness of -0.2209 (Figure 2.18). In COS7 cells, the distribution of CTΔ144-Env remained unbiased (Figures 2.17D, 2.19D, 2.20D), with a mean ϕ value of $2.338 \pm 2.287^\circ$ (standard error, $n = 260$ clusters) and a skewness of -0.09703 (Figure 2.18).

Next, the experiments were repeated with a second Env mutation, d8, a five-amino acid deletion in the second predicted helix region (LLP-3) of the cytoplasmic tail, which has been shown in previous studies to reduce incorporation of Env into released particles (Murakami and Freed, 2000). The mechanism of this incorporation defect has been suggested to be a steric clash or a disruption of binding between the lattice of Gag MA domains and the mutant cytoplasmic tail, supported by the fact that the incorporation levels can be rescued by Gag MA mutations (Murakami and Freed, 2000; Tedbury et al, 2013).

The d8 mutation did not significantly alter the distribution of Env on particles produced in CEM-A cells. Again, both analysis methods agreed on a significantly neck-biased distribution (Figures 2.17E, 2.19E, 2.20E), with a mean ϕ value of $-23.62 \pm 2.864^\circ$ (standard error, $n = 134$ clusters) and a skewness of 0.53 (Figure 2.18). Strikingly, the d8 mutation caused a slight neck-biased distribution of Env on particles produced in COS7 cells, where the distribution of wild type (WT) Env was unbiased (Figures 2.17F, 2.19F, 2.20F). A skewness of 0.236 suggested only a somewhat asymmetric distribution, but the mean ϕ value of $-9.401 \pm 1.641^\circ$ (standard error, $n = 582$ clusters) differed significantly from the theoretical unbiased mean of 0° (Figure 2.18).

We attempted to repeat these results in an entirely separate experimental system, using immunogold labeling of Env, imaged by transmission electron microscopy (Figure 2.21; Appendix J). However, the poor labeling density of immunogold and the sample sectioning required for TEM imaging made it unreasonable to amass significant statistical power of budding particles that were both labeled for Env and sectioned such that the budding axis was identifiable.

Nevertheless, we hypothesized two possible explanations for the neck bias induced in COS7 cells by the d8 mutation. The first relies on the proposed model of d8-Env being

specifically occluded from virus particles due to a steric clash with the Gag lattice. Possibly this disruption of complementarity causes Env to be forced to the edges of the lattice, even though encounters still occur throughout Gag lattice assembly. The second hypothesis recalls the model results we proposed for this experiment (Figure 1.2B). According to this models, a neck bias is expected if timing of Env encounter is late in the assembly of the Gag lattice. The cell type dependence of WT-Env distribution suggested a host cell mechanism of regulating this timing, and the d8 mutation could be disruptive to this mechanism, causing a delay in Env encounter with Gag lattices, supported by previous studies that showed related mutations of the Env cytoplasmic tail altered intracellular trafficking (Qi et al, 2015). Our data could not distinguish between these two explanations of the neck-biased distribution of d8-Env in COS7 cells, and they could not definitively distinguish between the two explanations of the unbiased distributions of CTΔ144-Env and of WT-Env in COS7. Further experiments were needed to properly understand these results.

CHAPTER THREE: DIFFUSION OF ENV ON THE PLASMA MEMBRANE

In our hypothesized model (Figure 1.2), there were two possible explanations for unbiased distributions of Env about particles. Either Env is incorporated throughout the duration of Gag lattice formation, or Env does not become fixed in the lattice during incorporation and is able to diffuse to any angular position regardless of the timing of its encounter with the lattice. The fact that the CTΔ144 mutant was found to have an unbiased distribution about particles produced in both cell types could be explained by the hypothesis suggested in previous studies that trapping of Env in the Gag lattice is dependent on the long cytoplasmic tail.

This explanation fits with the incorporation defect that has previously been shown for CTΔ144-Env. If WT-Env becomes trapped at assembly sites when it encounters a Gag lattice, and CTΔ144-Env does not become trapped and is able to diffuse away, then there will be less CTΔ144-Env incorporated into particles when they release. In collaboration with Melissa Fernandez and Eric Freed's lab, we confirmed this result (Figure 3.1) by western blot of released virus, stained for Env and normalized to Gag CA labeling. This assay showed a significant reduction in the level of incorporation of both CTΔ144- and d8-Env relative to WT-Env in both cell types. If the unbiased distribution of CTΔ144-Env had resulted from trapping of Env throughout lattice assembly, then incorporation levels of CTΔ144-Env would be higher.

Likewise, if the cell type specific unbiased distribution of WT-Env in COS7 cells were the result of some kind of cell type dependent lack of trapping, we would expect to see a defect in Env incorporation into COS7-produced virus particles compared with the CEM-A-produced counterparts, whereas if it were the result of Env incorporation throughout lattice assembly, we would expect to see increased incorporation relative to CEM-A-produced particles. This was

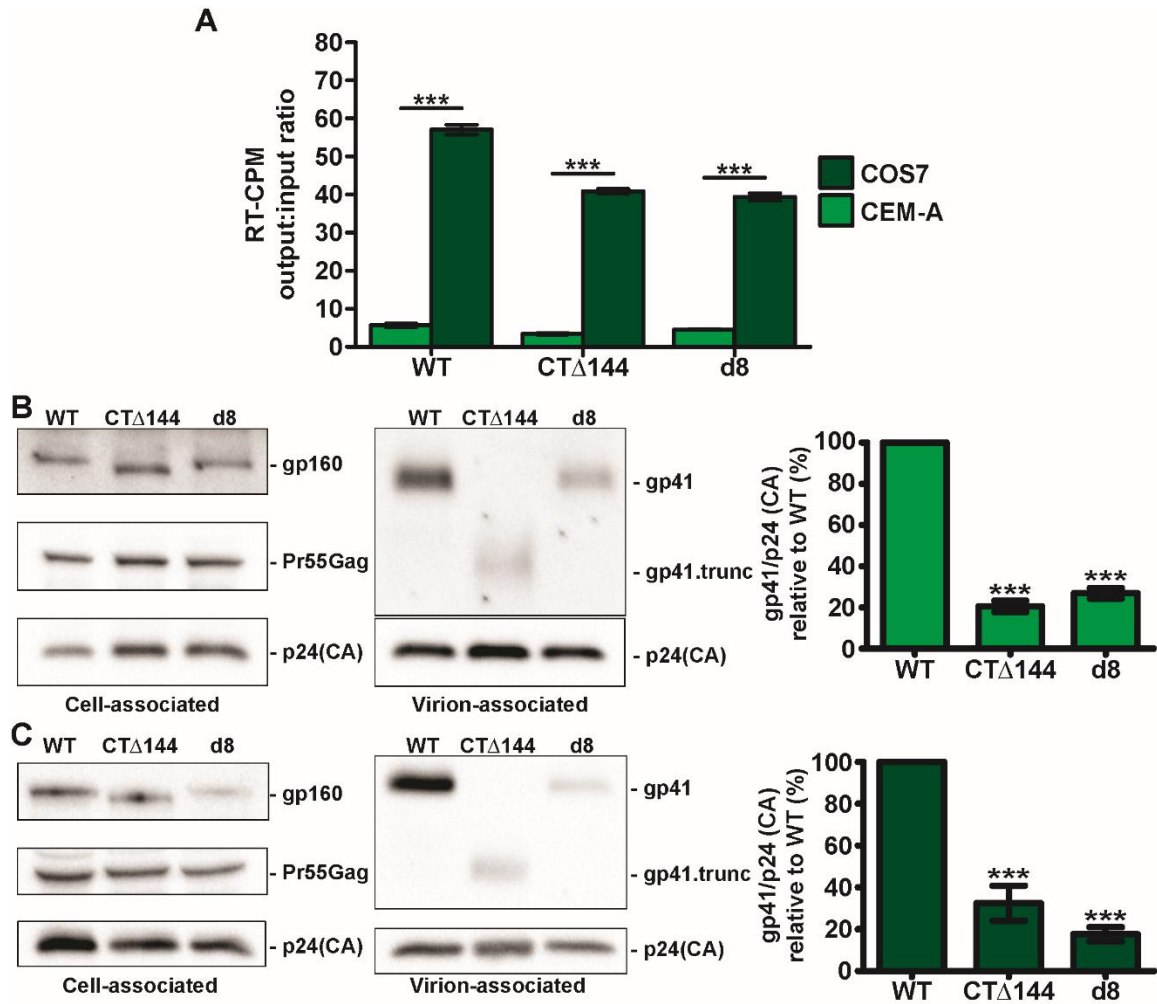


Figure 3.1. Incorporation of Env-CT mutants is defective in both CEM-A and COS7 cells.

(A) Ratio of output reverse transcriptase (RT) activity in post-infection supernatant to input RT activity used for infection, normalized to cell count. Production levels of viral proteins are much higher in COS7 cells than in CEM-A cells. Virus produced in **(B)** CEM-A cells and in **(C)** COS7 cells both incorporate significantly less CTΔ144- and d8-Env than WT-Env. Env incorporation was calculated as the ratio of gp41 to p24 (CA) signal in a western blot. Representative blots (left) and quantification (right) of **(B)** 4 and **(C)** 3 independent experiments are shown. Bars represent mean and standard error. In **(A)**, *** indicates significant difference between cell lines for each genotype with $P < 0.0001$ by one-way ANOVA and Tukey's post-test. In **(B)** and **(C)**, *** indicates significant difference from WT with $P < 0.0001$ by one-way ANOVA and Tukey's post-test.

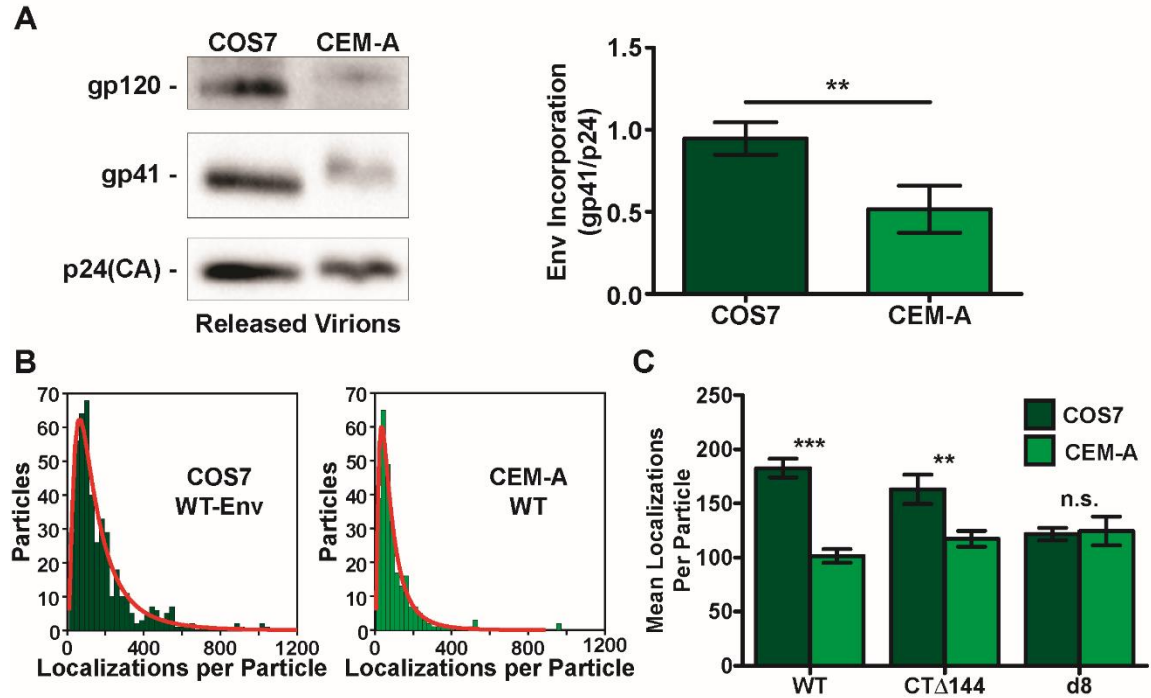


Figure 3.2. Differential Env incorporation between producer cell types. **(A)** Western blots of released virions were used to assess levels of WT-Env incorporation into viruses produced in CEM-A compared with COS7 cells, quantified as in Figure 3.1. In COS7 cells, the mean ratio of gp41 to p24 was calculated as 0.95 ± 0.10 ($n = 4$ experiments). In CEM-A cells the mean ratio was 0.52 ± 0.14 ($n = 4$ experiments). The bar graph to the right represents mean and standard deviation. ** indicates $P < 0.005$ by two-tailed unpaired t-test. **(B)** Indirect qualitative assessment of the density of Env signal per assembly site by counting localizations per segmented particles. Histograms were generated and fit to lognormal distributions (red). **(C)** The parameters of the lognormal fit of each histogram were used to compare Env densities at assembly sites in each cell type. Bars represent mean and standard error. For WT-Env, mean in COS7 = 182.6 ± 8.6 localizations, mean in CEM-A = 101.5 ± 6.3 . For CTΔ144-Env, mean in COS7 = 163.1 ± 13.5 , mean in CEM-A = 117.4 ± 7.2 . For d8-Env, mean in COS7 = 121.7 ± 5.8 , mean in CEM-A = 124.6 ± 13.4 . *** indicates $P < 0.0001$, ** indicates $P < 0.005$, and n.s. indicates $P = 0.8445$, by two-tailed unpaired t-test with Welch's correction.

tested; released virus particles produced by both cell types were collected and compared directly by western blot. It was confirmed that a much greater ratio of Env to Gag was incorporated particles produced in COS7 cells than in those produced in CEM-A cells (Figure 3.2A). To support this result, we also returned to our iPALM imaging data. For each segmented assembly site, the number of localizations collected in the Env channel was counted. Histograms were generated of these counts for each dataset and a lognormal function was fit to the distribution (Figure 3.2B). The particles segmented from COS7 cells included significantly more WT-Env signal than those segmented from CEM-A cells (Figure 3.2C). Interestingly, the COS7 particles also included significantly more CTΔ144-Env than the CEM-A particles, while particles produced in both cell types incorporated approximately the same amount of d8-Env. Although this is not a direct measure of Env molecules, since both the labeling density and blinking properties of the organic dye vary, it is generally proportional across experiments conducted under consistent labeling conditions.

In order to test this explanation directly, we decided to visualize the diffusion behavior of Env on the surfaces of live cells and the effect of our mutations and cell types on that behavior. Through collaboration with Nairi Pezeshkian, a PhD student in the van Engelenburg lab, on her live cell imaging project, data was collected on the same PALM microscope system (absent the interferometric components), imaging immunolabeled Env on the surfaces of both CEM-A and COS7 cells. This data was used for single particle tracking (SPT) analysis. SPT uses point localization of sparse fluorophores to track movement of the emitters over time by identifying PSF's in sequentially imaged frames that were emitted by the same molecule. This analysis is made difficult by many characteristics of biological systems such as that of our diffusing Env. The density of emitters, the high speed at which they can diffuse on the nanometer scale, and the blinking and bleaching characteristics of the fluorophores make properly identifying and differentiating individual molecules' tracks challenging. However, SPT benefits by analyzing populations of molecules, rather than measuring the average or net characteristics of the population as a whole. It also allows us to discriminate between sub-populations of the whole,

such as between Env trimers of different diffusive states. A 2008 study established a method of SPT analysis that confronts these challenges, which has been widely used since (Jaqaman et al, 2008). We used the software made available in that study to analyze live-cell time lapses of Env on the surfaces of cells.

Coverslips were prepared in the same way as those used for iPALM experiments and CEM-A cells were infected by the same protocol and allowed to express for 40 hours before live-cell immunolabeling (Appendices B, D, E, F, G). The cells were blocked, again in 10% bovine serum albumin and again for 30 minutes, but in a solution of RPMI media and at 37°C to preserve cell health. To prevent the crosslinking of Env trimers by bivalent antibodies, which would disturb the diffusion behavior of Env, immunolabeling was done using recombinantly produced b12 antibody Fab fragments. These recombinant Fab fragments were developed by Nairi Pezeshkian for application in her own research, and were directly conjugated to the organic dye Atto565 (#72464, Sigma-Aldrich, St. Louis, MO) at approximately a 1:1 ratio. Atto565 is bright and photostable, and is therefore well-suited to tracking experiments. The pulse-chase labeling protocol used for immunolabeling Env on live cells was also developed and performed by Nairi (Appendix K). This labeling pulse allowed for Fab binding of only the Env trimers that were exposed on the cell surface during the pulse. Labeling was done at room temperature to limit endocytosis of labeled Env, which would reduce the statistical power of the measured surface population and could contribute to defocused background signal or even be localized while trafficking in vesicles and misclassified as directed motion at the cell surface. The cells were washed thoroughly as before to remove any un-bound Fab, but with media and for shortened time periods to preserve cell health. The samples were then mounted in media and sealed under a clean, sterile 18 mm coverslip with epoxy. Time lapses were collected until failing cell health became apparent, or, at most, 1 hour after samples were sealed.

Samples were imaged on the PALM microscope in the absence of the beam splitter, the top objective, and two of the three cameras. The Atto565 dye was excited by a 561 nm laser at frame rates of 17 – 19 ms. The diffraction limited PSF's in each frame of the acquired time lapses

were point-localized as before. The shorter exposure times limited the photons collected in each frame, and therefore degraded the certainty of point localization, but were necessary for adequate temporal sampling resolution of diffusing tracks. The uTrack MATLAB program (Jaqaman et al, 2008), modified and implemented for our purposes by Nairi, was used to identify PSF's given by the same emitter in consecutive frames and link them into tracks. Only tracks composed of 20 or more individual localizations were included in our population analyses. These tracks were classified by the uTrack system as either mobile, confined, or immobile. Confined and immobile tracks were considered to represent an immobilized or trapped population, and mobile tracks were considered freely diffusing (Figure 3.3). The diffusion coefficient D of each track was calculated (Figure 3.4), and the diffusion coefficients of all tracks in the mobile population were compared across genotype and cell type (Figure 3.5).

In CEM-A cells, we calculated the mean diffusion coefficients of the tracks that had been classified as mobile (Figure 3.5A). The mobile fraction of WT-Env tracks had a mean diffusion coefficient of $0.097 \pm 0.049 \mu\text{m}^2 \times \text{s}^{-1}$ (standard deviation, $n = 1514$ tracks, 4 biological replicates). The mobile fraction of CTΔ144-Env had a mean diffusion coefficient of $0.149 \pm 0.054 \mu\text{m}^2 \times \text{s}^{-1}$ (standard deviation, $n = 9694$, 4 biological replicates), which did not significantly differ from that of WT. This agrees with previous studies (Chojnacki et al, 2017). The mobile fraction of d8-Env had a mean diffusion coefficient of $0.107 \pm 0.067 \mu\text{m}^2 \times \text{s}^{-1}$ (standard deviation, $n = 2139$ tracks, 4 biological replicates). This was not significantly different from either WT- or CTΔ144-Env. This suggests that the absence or mutation of the cytoplasmic tail does not alter the diffusive behavior of Env. However, the fraction of the total population of Env that was classified as mobile did differ between genotypes. Four cells were imaged of each condition, and a mean was taken of the fractions classified as either confined or immobile, weighted by the number of tracks in each cell (Figure 3.6A). A weighted mean of $80 \pm 6\%$ of WT-Env were classified as confined/immobile (standard deviation, $n = 7862$ tracks, 4 biological replicates), whereas only $27 \pm 5\%$ of CTΔ144-Env were confined/immobile (standard deviation, $n = 13338$ tracks, 4 biological replicates). This

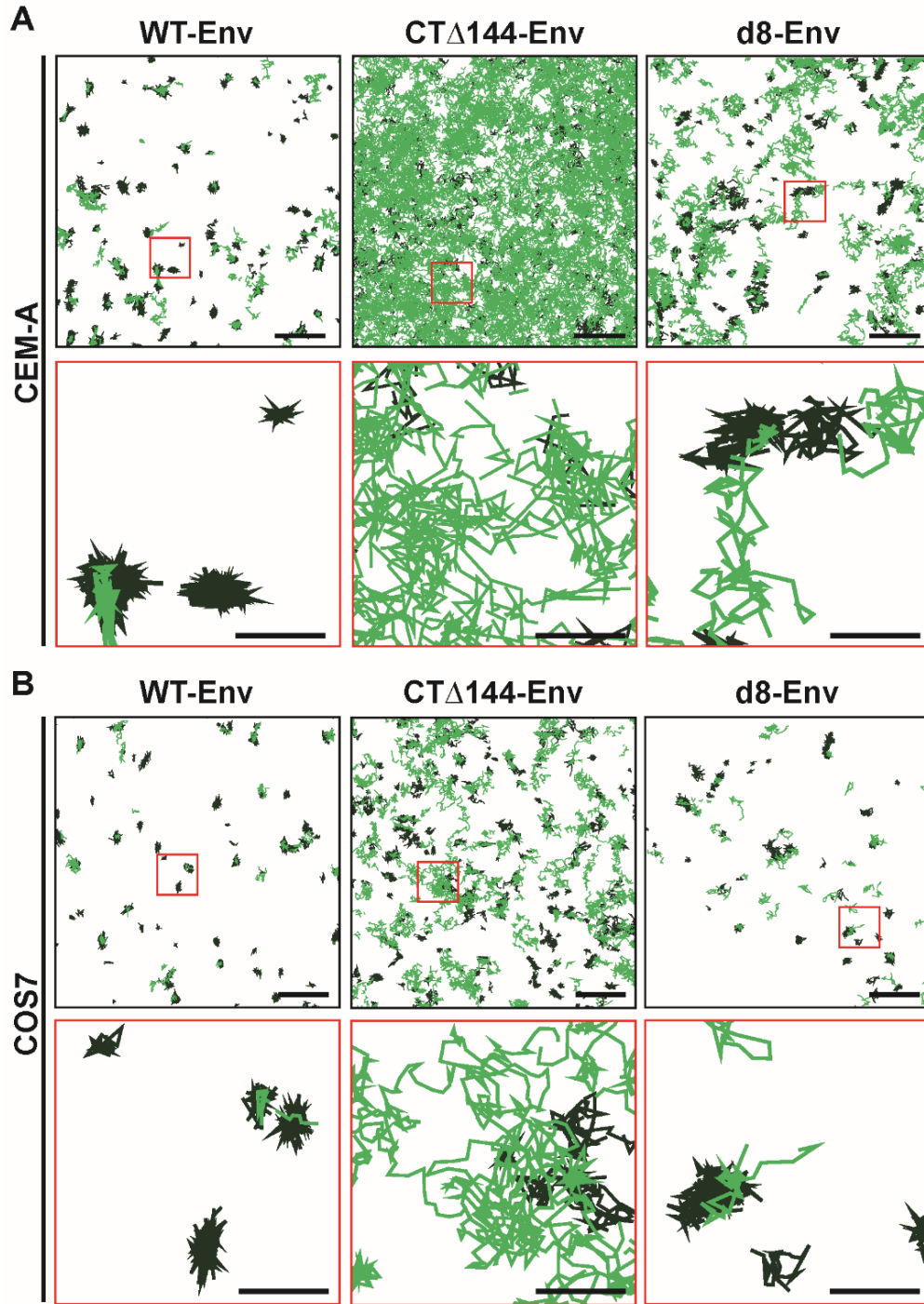


Figure 3.3. Single particle tracking of Env trimers, classified as mobile or trapped. Representative fields of view showing rendered Env tracks in **(A)** CEM-A and **(B)** COS7 cells. Tracks classified as mobile are rendered in light green. Tracks classified as either immobile or confined are rendered in dark green. Scale bars in wide zoom (top, black border) are 2 μ m. Scale bars in insets (bottom, red border) are 500 nm.

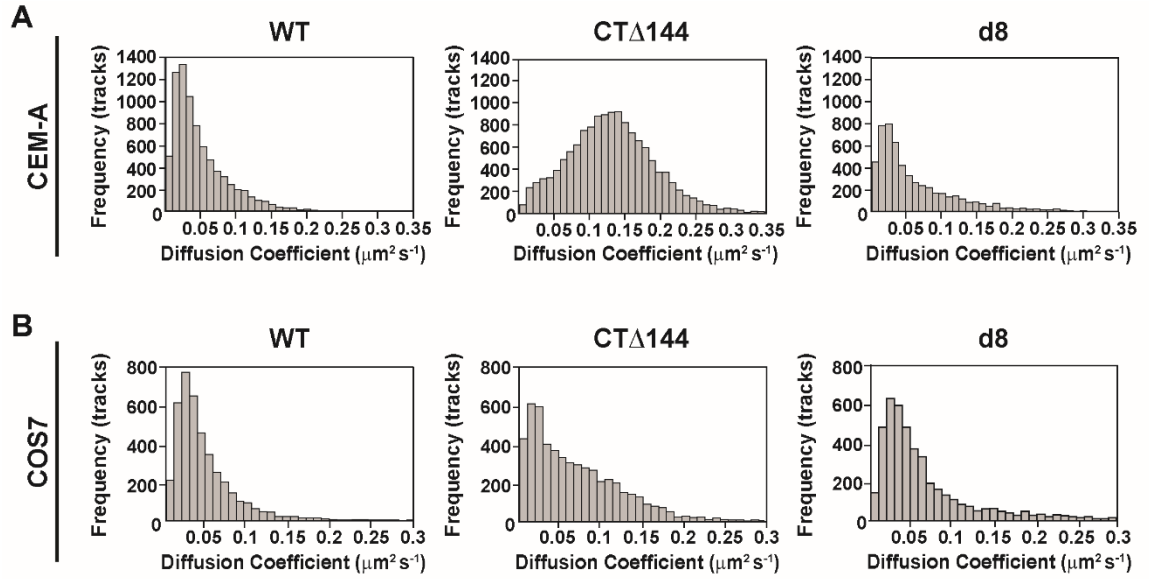


Figure 3.4. Distributions of diffusion coefficients calculated for all tracks in each condition. For all tracks observed by single particle tracking, the diffusion coefficient D was calculated in uTrack (Jaqaman et al, 2008). The distributions of D values for each condition in **(A)** CEM-A and **(B)** COS7 cells are displayed as histograms. For **(A)** CEM-A, WT-Env $n = 7862$ tracks from 4 cells, CT Δ 144-Env $n = 13,338$ tracks from 4 cells, d8-Env $n = 5434$ tracks from 4 cells. For **(B)** COS7, WT-Env $n = 3790$ tracks from 5 cells, CT Δ 144-Env $n = 5283$ tracks from 4 cells, d8-Env $n = 4384$ tracks from 17 cells.

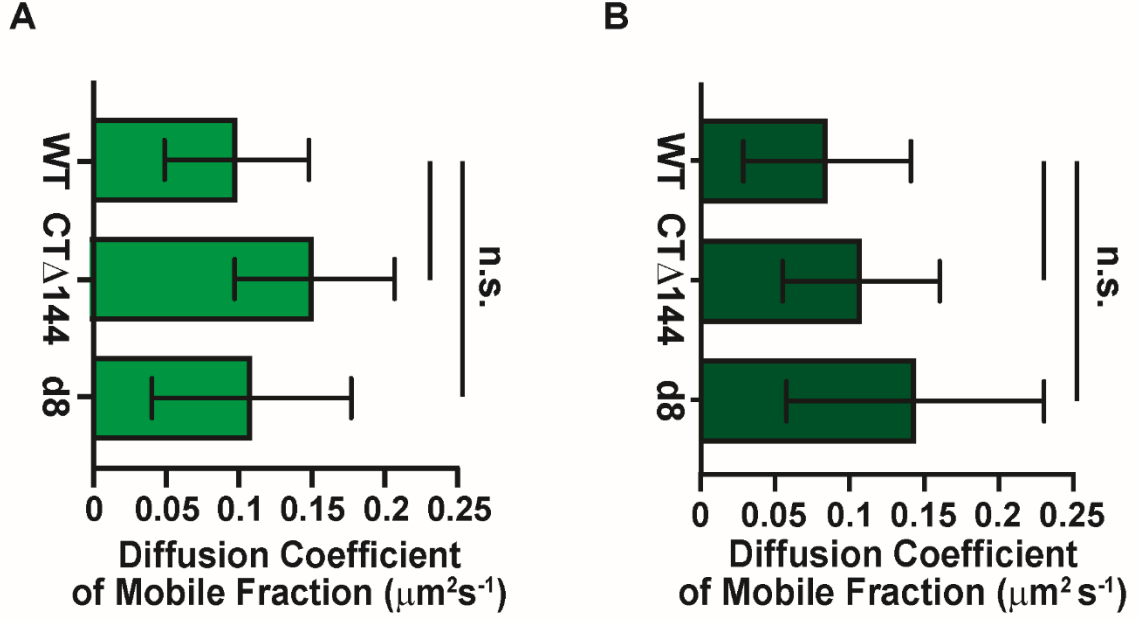


Figure 3.5. Diffusion coefficients of mobile Env trimers do not differ significantly between genotype or cell type. For the tracks classified as mobile in each condition, the mean diffusion coefficient D was calculated. **(A)** In CEM-A cells, the mean diffusion coefficients of CT Δ 144-Env ($D_{\text{mobile}} = 0.149 \pm 0.087 \mu\text{m}^2\text{s}^{-1}$, $n = 9694$ tracks) and d8-Env tracks ($D_{\text{mobile}} = 0.107 \pm 0.057 \mu\text{m}^2\text{s}^{-1}$, $n = 2139$ tracks) did not differ significantly from that of WT-Env ($D_{\text{mobile}} = 0.097 \pm 0.049 \mu\text{m}^2\text{s}^{-1}$, 1514 tracks). **(B)** In COS7 cells, the mean diffusion coefficients of CT Δ 144-Env ($D_{\text{mobile}} = 0.108 \pm 0.053 \mu\text{m}^2\text{s}^{-1}$, $n = 2238$ tracks) and d8-Env tracks ($D_{\text{mobile}} = 0.144 \pm 0.087 \mu\text{m}^2\text{s}^{-1}$, $n = 1019$ tracks) did not differ significantly from that of WT-Env ($D_{\text{mobile}} = 0.085 \pm 0.056 \mu\text{m}^2\text{s}^{-1}$, 274 tracks). Error bars represent standard deviation. n.s. indicates not significant by one-way ANOVA and Tukey's post-test.

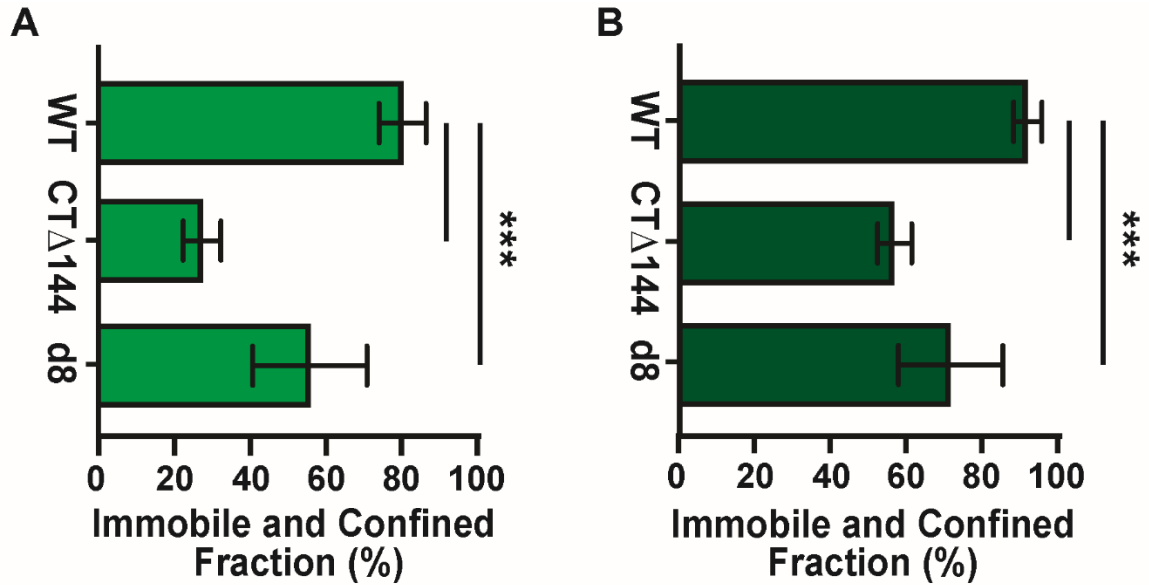


Figure 3.6. The fraction of Env trimers classified as trapped is dependent on the Env-CT. The fraction of Env tracks classified as either immobile or confined was found for each cell, and a mean fraction, weighted by the number of tracks in each cell, was calculated. **(A)** In CEM-A cells, the fraction of the total population of Env tracks that was classified as either immobile or confined was significantly smaller in both CTΔ144-Env (27±5%, n = 13,338 total tracks from 4 cells) and d8-Env (56±15%, n = 5434 total tracks from 4 cells) than in WT-Env (80±6%, n = 7862 total tracks from 4 cells). **(B)** In COS7 cells, immobilization of different genotypes follows the same trend as in CEM-A cells. Both CTΔ144-Env (57±5%, n = 5283 total tracks from 4 cells) and d8-Env (72±13%, n = 4384 total tracks from 17 cells) had significantly smaller immobile/confined fractions than did WT-Env (92±4%, n = 3790 total tracks from 5 cells). Error bars represent standard deviation. *** indicates $P < 0.0001$ by one-way ANOVA with Tukey's post-test.

supports the model that Env trapping depends on the cytoplasmic tail. The CTΔ144-Env does not become fixed in the Gag lattice, and more of it remains mobile on the plasma membrane. A mean of $56 \pm 15\%$ of d8-Env were classified as confined/immobile (standard deviation, $n = 5434$ tracks, 4 biological replicates). This suggests a partial defect in trapping due to the d8 mutation.

When the experiments were conducted in COS7 cells, the cells were reverse transfected rather than infected (Appendix L). Again, the mean diffusion coefficients of the mobile fractions did not differ significantly between genotypes (Figure 3.5B). The mobile fraction of WT-Env had a mean diffusion coefficient of $0.085 \pm 0.056 \mu\text{m}^2\text{s}^{-1}$ (standard deviation, $n = 274$ tracks, 5 biological replicates), the mobile fraction of CTΔ144-Env had a mean diffusion coefficient of $0.108 \pm 0.053 \mu\text{m}^2\text{s}^{-1}$ (standard deviation, $n = 2238$, 4 biological replicates), and the mobile fraction of d8-Env had a mean diffusion coefficient of $0.144 \pm 0.087 \mu\text{m}^2\text{s}^{-1}$ (standard deviation, $n = 1019$ tracks, 17 biological replicates). The trend of mobile fraction size did not differ from that observed in CEM-A cells (Figure 3.6B). A weighted mean of $92 \pm 4\%$ of WT-Env were classified as confined/immobile (standard deviation, $n = 3790$ tracks, 5 biological replicates), while a weighted mean of $57 \pm 5\%$ of CTΔ144-Env (standard deviation, $n = 5283$ tracks, 4 biological replicates) and a weighted mean of $72 \pm 13\%$ of d8-Env were confined/immobile (standard deviation, $n = 4384$ tracks, 17 biological replicates), both significantly less than in WT.

The significantly lower fraction of immobile and confined CTΔ144-Env compared with that of WT-Env in both cell types helps to explain the genotype-dependent differences in Env angular distributions observed by iPALM (Figure 2.18). It appears to confirm the model that the CTΔ144-Env does not become trapped and samples the entire surface of budding particles by undeterred diffusion. It also disproves the hypothesis that a lack of trapping of Env in the Gag lattice causes the unbiased distribution of WT-Env observed in COS7 cells, supporting the alternate explanation that the unbiased distribution is due to earlier Env encounters with Gag lattices. The smaller immobilized fraction of d8-Env compared with WT-Env supports the hypothesis that the d8 mutant is specifically excluded from assembly sites. If d8-Env is sterically occluded from Gag lattices due to clashing, it would explain the decreased population of trapped d8-Env compared

with WT. This does not necessarily disprove the hypothesis that the d8 mutation alters the timing of incorporation, but it does not appear to be due to differential diffusivity. However, the fact that the pattern of Env diffusion characteristics of each Env genotype does not differ between the CEM-A and COS7 cell lines suggests that the observed characteristics are not cell type dependent, and, therefore, cannot account for the cell type dependent differences observed in Env angular distributions.

CHAPTER FOUR: HOST CELL INTRACELLULAR TRAFFICKING AS A REGULATOR OF ENV INCORPORATION

Having shown that the late-stage incorporation of WT-Env into particle assembly sites is cell type dependent and that the unbiased distribution seen in COS7 cells, but not CEM-A cells, is due to earlier incorporation of Env, we still hoped to illuminate the mechanism of this cell type dependent regulation. It has previously been shown that Env is rapidly internalized upon reaching the plasma membrane and is then sorted into the recycling endosome before being returned to the plasma membrane (Egan et al, 1996; Gropelli et al, 2014; Kirschman et al, 2018). This pathway seemed a likely candidate for a mechanism of host cell regulation of the timing of Env encounters with assembly sites.

We hypothesized that the cell type dependent neck-biased distribution of WT-Env which we observed in CEM-A cells, but not COS7 cells, may result from Env retention within intracellular compartments and limited recycling back to the plasma membrane during autonomous assembly of Gag lattices. In this model, lattice trapping of Env is a driver of Env incorporation, ensuring that any Env that encounters a particle assembly site will be incorporated into the subsequent virus, but it is opposed by the competing mechanism of rapid Env endocytosis and sequestration within intracellular compartments. In the natural host cell type, T-cells, the steady state balance of these two opposing mechanisms optimizes the levels of Env on cell surfaces and released virions to maintain infectivity but minimize visibility. However, in other cell types, such as fibroblasts, the host cell's endocytosis and recycling behaviors may be different and could account for both the cell type dependent timing of Env-Gag lattice encounter and the upregulated incorporation of Env into released particles.

In order to test this hypothesis, we designed a series of experiments to assess the distribution of Env between the cell surface and the recycling endosome within the cell, and the dependence of this distribution on Env genotype and host cell type. Since sub-diffraction limited resolution was not required for these assays, conventional spinning disk confocal microscopy was used instead of iPALM.

First, surface staining of fixed infected cells was used to assay the relative densities of Env present on the cell surface for each condition. By labeling only surface-exposed Env, we hoped to be able to explore any effect that Env genotype may have on the amount of Env available to be incorporated into lattices. If, as we hypothesize, the cytoplasmic tail mutants we have tested disrupt proper trafficking through the Env pathway, steady state levels of Env on the cell surface would likely be altered.

Coverslips were cleaned (Appendix E) but were not treated with nanorods or glass. CEM-A and COS7 cells were each adhered to coverslips (Appendix F) and infected with virus using the same protocol that was used for the iPALM experiments (Appendix G). The cells were fixed by the same method 40 hours after infection, but were blocked and immunolabeled without being treated with detergent so that the membrane stayed intact and only externally exposed Env was accessible to the dye-labeled antibodies. The same antibodies against Env were used, but at a higher concentration to improve signal brightness on the less sensitive camera of the confocal microscope system. The samples were mounted in Fluoromount-G (#0100-01, Southern Biotech) and sealed under clean cover glass (Appendix M). Z-stacks of approximately 100 fields of view, usually including multiple cells in each field, were acquired with super-sampled slices of 300 nm at exposure times of 100 ms. The AF647 dyes were excited by a 640 nm laser at approximately $315 \pm 5 \mu\text{Wcm}^{-2}$. The data were quantified by normalizing the total labeling intensity of each cell to the cell's approximate size. Maximum projections were generated of each cell and thresholded to create a mask of the cell border, which was applied to an integrated projection of the cell to compute both the projected area and the integrated intensity of that cell. Intensity was normalized

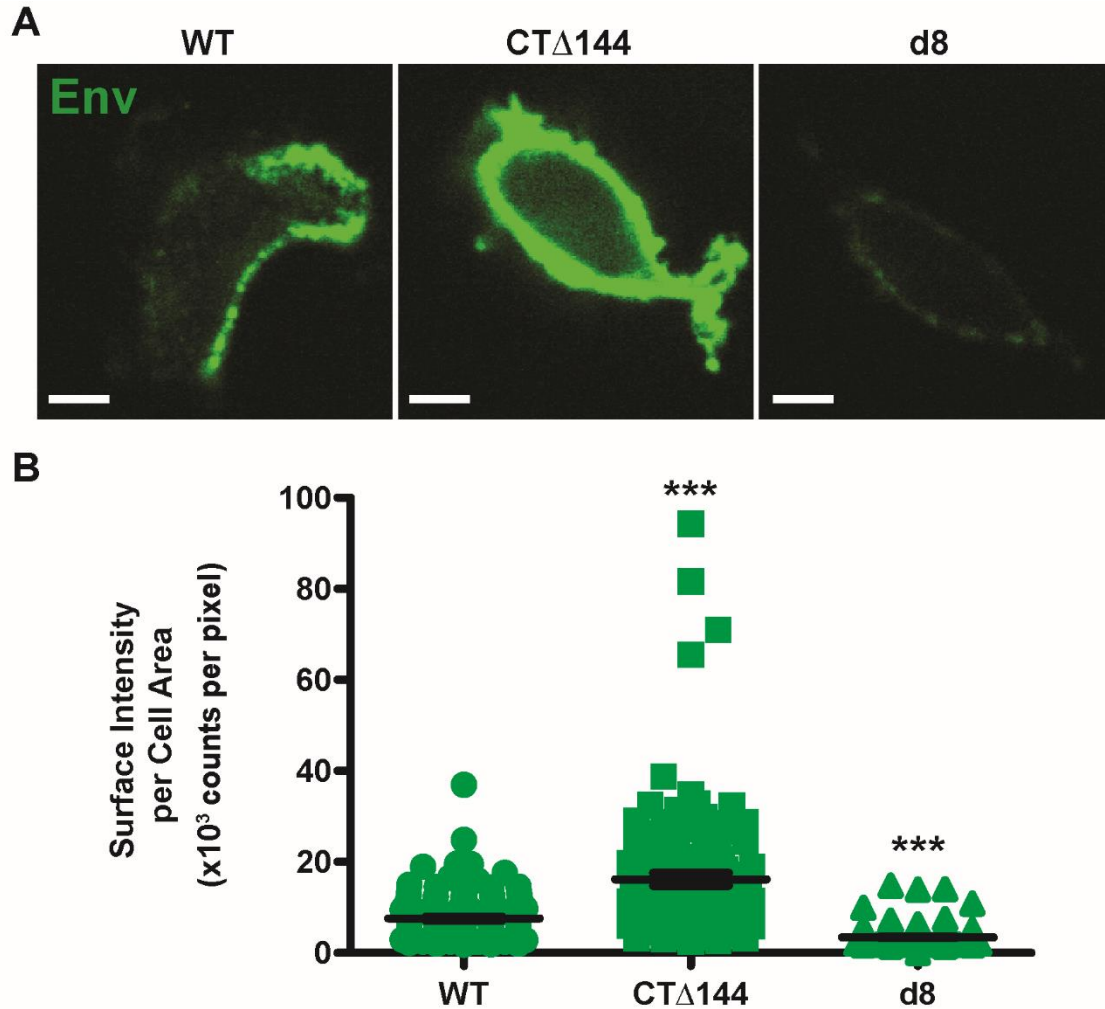


Figure 4.1. Density of Env on the host cell surface in CEM-A cells is dependent on Env-CT. **(A)** Representative images of whole CEM-A cells producing WT- (left), CT Δ 144- (middle), and d8-Env (right), fixed and labeled for surface-exposed Env. Scale bars are 10 μ m. **(B)** Quantification of the surface density of Env by normalization of integrated signal intensity throughout the Z-stack of each cell to each cell's projected area. There was significantly more CT Δ 144-Env (16,201 \pm 1385 counts per pixel, standard error, n = 113 cells) and significantly less d8-Env (3488 \pm 171.2 counts per pixel, standard error, n = 146 cells) on host cell surfaces than WT-Env (7594 \pm 478.6 counts per pixel, standard error, n = 123 cells). Bars represent mean and standard error. *** indicates significant difference from WT $P < 0.0001$ by two-tailed unpaired t-test.

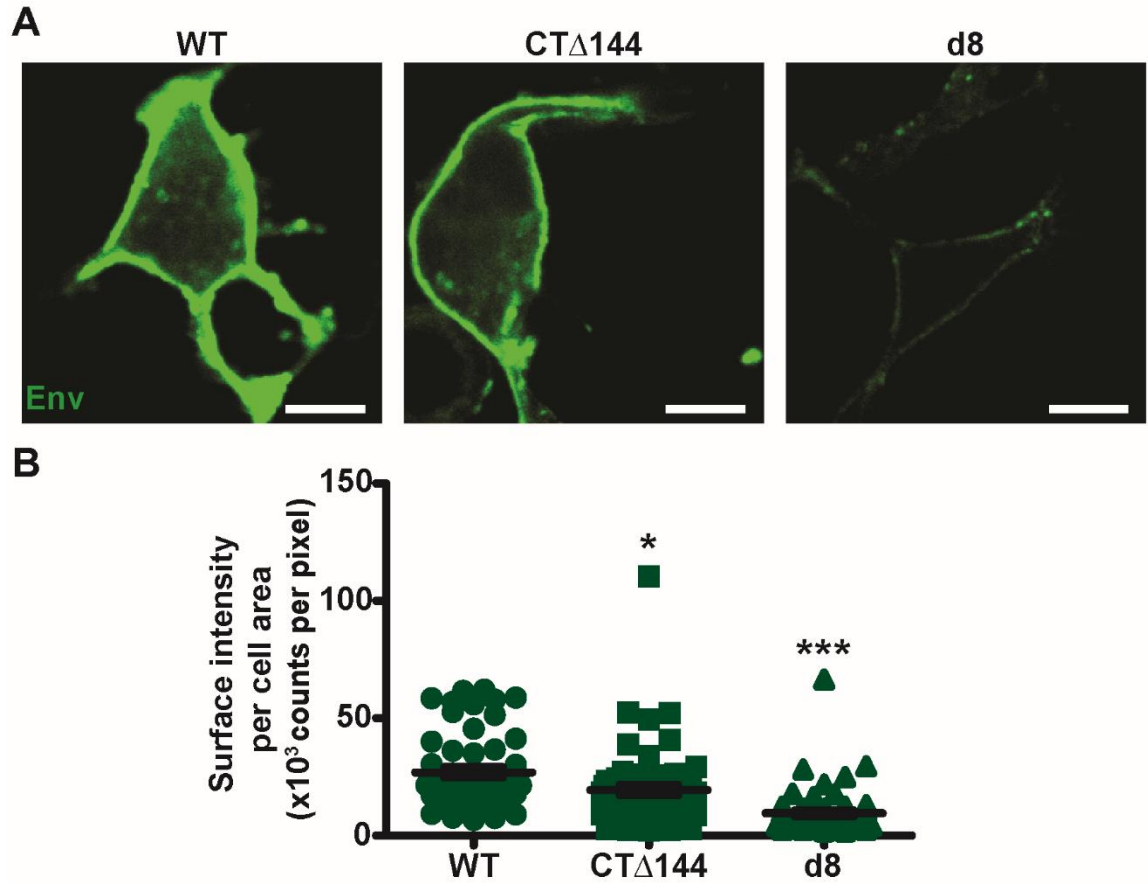


Figure 4.2. Density of Env on the surfaces of host cells in COS7 cells is upregulated by deletion of the Env-CT, as it is in CEM-A cells. (A) Representative images of whole COS7 cells producing WT- (left), CT Δ 144- (middle), and d8-Env (right), fixed and labeled for surface-exposed Env. Scale bars are 20 μ m. **(B)** Quantification of surface-exposed Env density, as in Figure 4.1, show that cell surface levels of both CT Δ 144- (19,434 \pm 2135 counts per pixel, standard error, n = 61 cells) and d8-Env (9507 \pm 1307 counts per pixel, standard error, n = 57 cells) are reduced compared with WT-Env (26,973 \pm 2201 counts per pixel, standard error, n = 54 cells). Bars represent mean and standard error. *** indicates $P < 0.0001$ and * indicates $P = 0.0156$ from WT by two-tailed unpaired t-test.

to projected area, and the distribution of that ratio for each genotype was compared as an assay of Env density on the cell surface.

In CEM-A cells, we found that the levels of CTΔ144-Env on the surface of cells were, in general, greatly increased when compared with cells expressing WT-Env (Figure 4.1). This is in agreement with previous studies which showed that the rapid endocytosis of Env is dependent upon the cytoplasmic tail (Egan et al, 1996; Groppelli et al, 2014; Kirschman et al, 2018). The d8 mutation, on the other hand, lead to much lower levels of surface-exposed Env compared with WT (Figure 4.1). This would appear to support the hypothesis that trafficking through the recycling pathway is altered by this mutation. However, it is also possible that, as our single particle tracking assays showed that a smaller fraction of d8-Env becomes trapped in lattices than does WT-Env, the un-trapped Env of both genotypes is rapidly endocytosed and the total amount of surface-exposed WT-Env is inflated by a greater density of trapped trimers.

The experiment was repeated in COS7 cells. Again, levels of surface-exposed d8-Env were greatly decreased compared with WT (Figure 4.2). Unexpectedly, however, levels of surface-exposed CTΔ144-Env appeared to be slightly decreased compared with WT-Env (Figure 4.2). This result was significant in explaining the cell type dependent differences we observed in angular distributions and in Env incorporation. An abundance of WT-Env on the plasma membrane throughout lattice assembly would lead to incorporation of considerably more Env into each assembling particle, whereas in the T-cell line, a low density of available Env would limit the amount of Env incorporated per particle. It would also be expected that a much greater density of Env on the cell surface would be much more likely to encounter early-stage assembling lattices than a lower density, which would account for the unbiased distribution of incorporated WT-Env we observed in COS7 cells.

In order to assess intracellular retention of internalized Env, a second assay was designed to compare the size of the endocytosed Env pool between genotypes. Again, cells were adhered to clean coverslips and infected as before (Appendices F, G). Instead of fixing the cells before immunolabeling, the cells were subjected to the same pulse-chase labeling protocol that

was used for the single particle tracking experiments, with the addition of transferrin conjugated to the organic dye Alexafluor488 (AF488; #T13342, Thermo Fisher; Appendix N). The subset of Env that was externally exposed at the time of the immunolabeling step was bound by dye-labeled Fab fragments while all other Env remained unlabeled. Likewise, the population of transferrin receptor that was externally exposed was bound by dye-labeled transferrin. The cells were then chemically fixed 15 minutes after the labeling pulse. This allowed Fab-bound Env that had been on the cells' surfaces during the staining step to be endocytosed before the system was fixed in place. We did not give the recycling pathway time to equilibrate to a true steady state distribution of labeled Env, but, as we expected that most genotypes would eventually favor an internalized majority, though potentially by nonspecific mechanisms, we hoped to learn more about Env internalization by comparing intracellular Env pools at an early but consistent post-pulse time point. Samples were mounted in Fluoromount-G under clean cover glass and sealed. Single diffraction limited images were acquired of approximately 100 fields of view, each of which usually included multiple individual cells. Atto565 dyes were excited with a 561 nm laser at approximately $200 \pm 5 \mu\text{Wcm}^{-2}$ at 100 ms exposure times. AF488 dyes were excited with a 488 nm laser at approximately $12 \pm 1 \mu\text{Wcm}^{-2}$ at 200 ms exposure times. Each field of view was focused in the middle of cells, so that the transferrin-labeled recycling compartment was optimally in focus. Each cell was segmented into three regions by manually tracing in ImageJ (NIH) the outer edge of the cell, the inner edge of the in-focus cell surface Env pool, and the intracellular Env pool which co-localized with the transferrin channel. The total intensity of the segmented intracellular pool was normalized to the summed total intensity of the segmented intracellular and cell surface pools.

In CEM-A cells, we observed a significant intracellular pool of labeled Env for all three genotypes (Figure 4.3). This intracellular Env pool co-localized closely with the corresponding intracellular pool of transferrin, confirming its identity as the recycling endosome (Figure 4.4A). When the data were quantified, we found that the size of the intracellular pool increased significantly when the d8 mutant was expressed, compared with WT-Env. In contrast, the intracellular pool of CTΔ144-Env was significantly smaller (Figure 4.3).

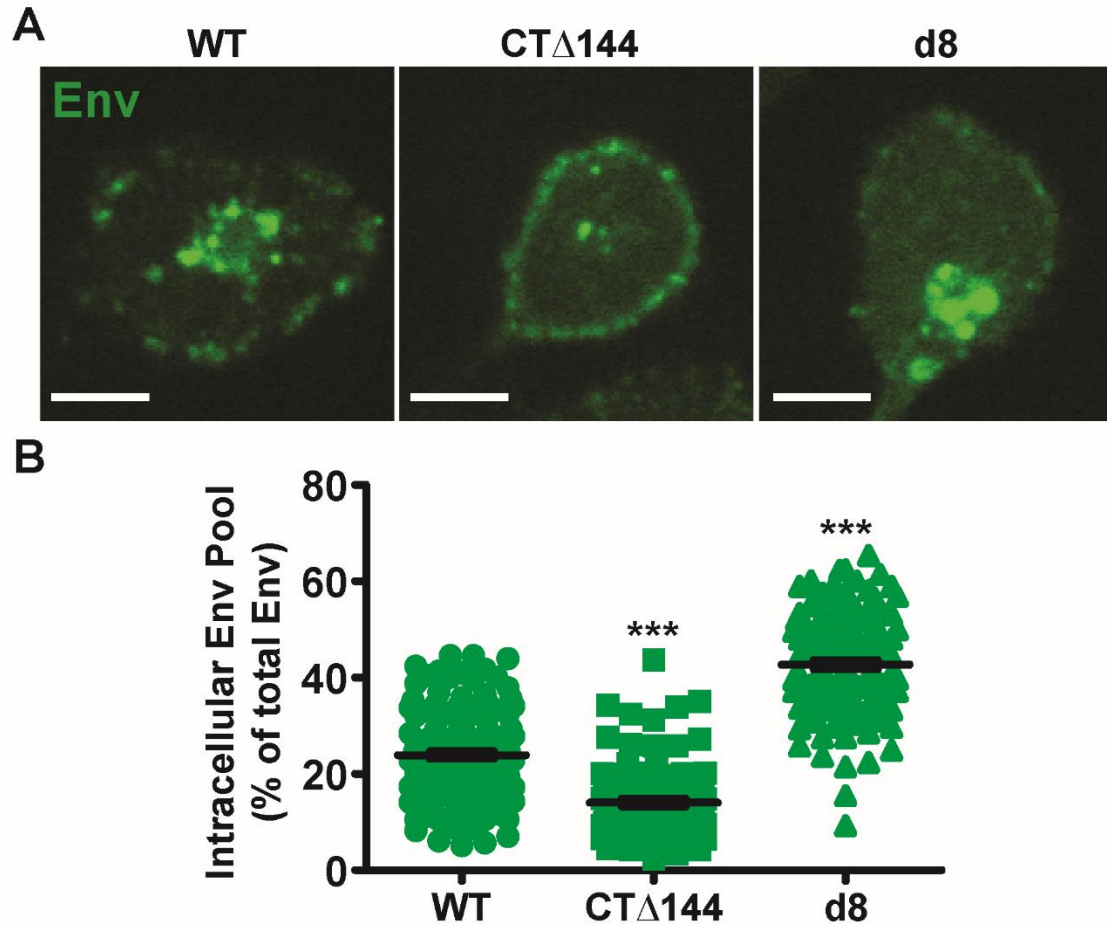


Figure 4.3. The internalized pool of Env in CEM-A cells is dependent on the Env-CT. Pulse-chase labeling followed by fixation of infected cells highlights Env internalized from the cell surface following the labeling pulse. **(A)** Representative images of CEM-A cells producing WT- (left), CT Δ 144- (middle), and d8-Env (right) show internalization and retention of intracellular Env is dictated by the Env-CT. Scale bars are 10 μ m. **(B)** Intracellular Env pools were quantified by normalizing segmented intracellular signal to the sum signal of the segmented intracellular and cell surface pools. The intracellular fraction of CT Δ 144-Env ($14 \pm 1\%$, standard error, $n = 99$ cells) was significantly lower than that of WT-Env ($24 \pm 1\%$, standard error, $n = 142$ cells). The intracellular fraction of d8-Env ($43 \pm 1\%$, standard error, $n = 123$ cells) was significantly higher. Bars represent mean and standard error. *** indicates $P < 0.0001$ from WT by two-tailed unpaired t-test.

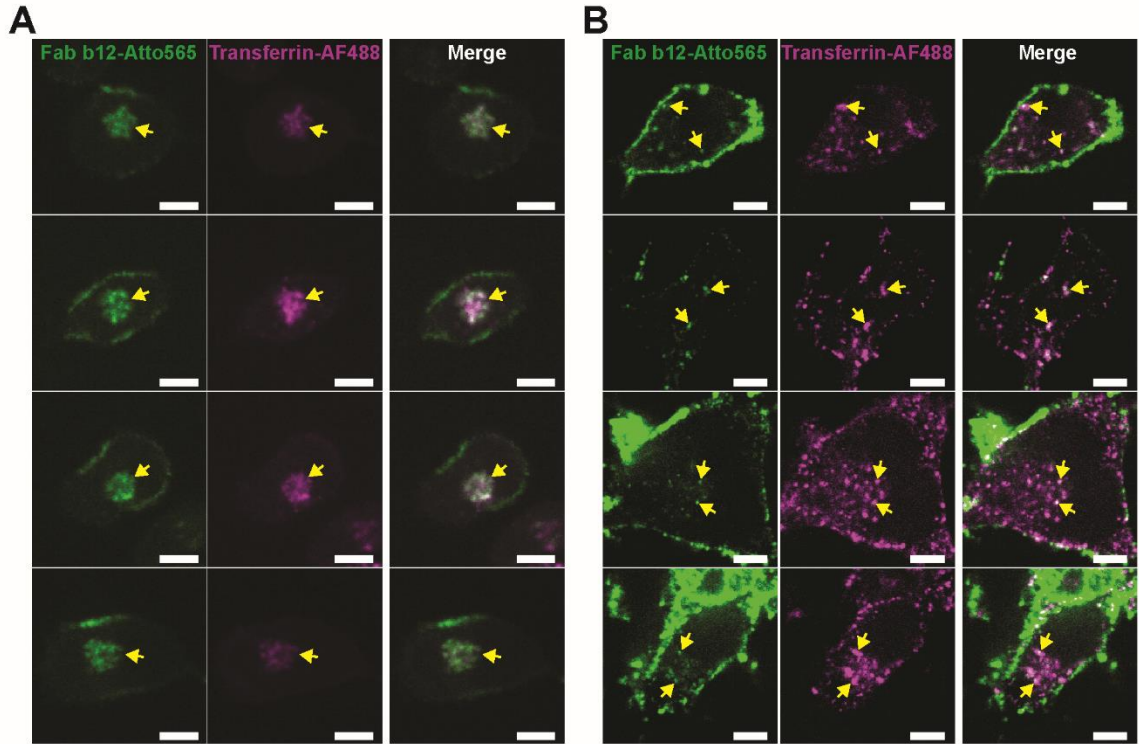


Figure 4.4. Env labeled at the cell surface is endocytosed and sorted to the recycling compartment. Live cells expressing WT-Env were pulse-chase labeled with both anti-Env Fab b12-Atto565 (green) and transferrin-AF488 (magenta) and then fixed after labeling to highlight internalized pools of labeled Env and transferrin receptor. **(A)** In CEM-A cells, internalized Env and transferrin receptor co-localized strongly in a large, centralized intracellular compartment (yellow arrows), identifying the intracellular pool of Env as the endosomal recycling compartment. Scale bars are 10 μm . **(B)** In COS7 cells, internalized Env pools were more dispersed and vesicular than in CEM-A cells, but still co-localized with transferrin (yellow arrows). Scale bars are 20 μm .

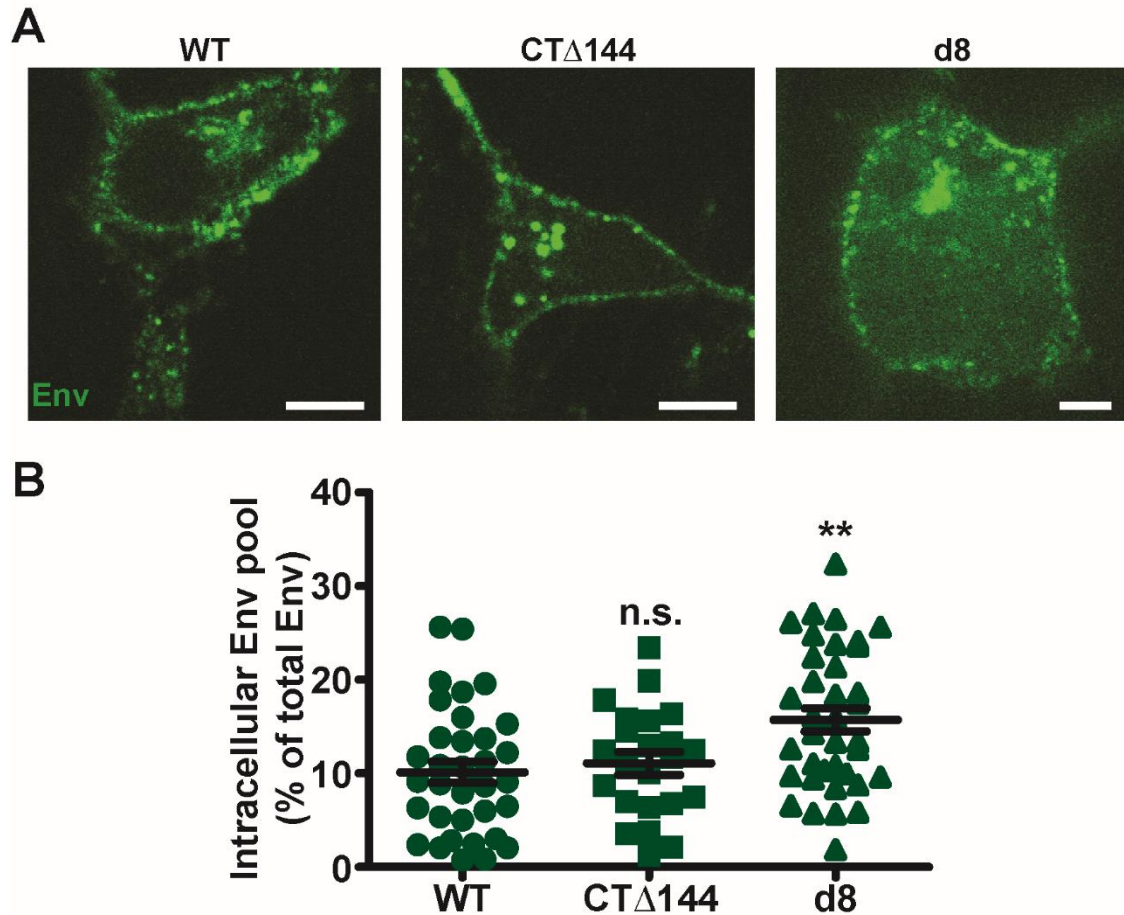


Figure 4.5. Internalized pools of Env in COS7 cells are altered by mutation, but not by deletion of the Env-CT. (A) Representative images of COS7 cells producing WT- (left), CT Δ 144- (middle), and d8-Env (right). Scale bars are 20 μ m. **(B)** The intracellular pool of Env was quantified as in Figure 4.3. There was no significant difference between WT- ($10 \pm 1\%$, standard error, $n = 35$ cells) and CT Δ 144-Env ($11 \pm 1\%$, standard error, $n = 23$ cells), but the intracellular pool of d8-Env was again significantly larger ($16 \pm 1\%$, standard error, $n = 36$ cells). Bars represent mean and standard error. ** indicates $P=0.0058$ and n.s. indicates not significant from WT by two-tailed unpaired t-test.

The intracellular pool of labeled Env in COS7 cells appeared both smaller and more dispersed than in CEM-A cells (Figure 4.5). These multiple smaller compartments still co-localized with transferrin labeling (Figure 4.4B), but their dispersed, vesicular morphology appeared distinctly different, which supports the idea of a difference in the recycling pathway between the two cell types. Unlike the CEM-A cells, COS7 cells producing CTΔ144-Env did not differ significantly from those producing WT-Env in the size of their intracellular Env pools (Figure 4.5). The intracellular pool of d8-Env, however, was again significantly larger than that of WT-Env (Figure 4.5).

Finally, we designed an assay intended to assess differences in the dynamics of Env trafficking to and from the recycling endosome using Fluorescence Recovery After Photobleaching (FRAP). FRAP uses targeted photobleaching of fluorophores in a particular region to study gross scale diffusion and mobility characteristics by quantifying the signal recovery in the bleached region. In an average FRAP experiment, measuring the degree of signal recovery within the photobleached region can be used to calculate a mobile fraction characteristic similar to the one we characterized by classifying the mobility of single particle tracks, and measuring the rate of signal recovery can be used to calculate an average rate of diffusion. We adapted this technique to examine intracellular trafficking, rather than diffusion, by photobleaching the labeled Env in the recycling endosome and then measuring the recovery of the intracellular signal. The same infection and pulse-chase immunolabeling protocol was used, but instead of fixing the infected cells after labeling, the samples were left unfixed and unsealed, and cells were imaged live approximately 15 minutes after the labeling pulse (Appendix K). Only CEM-A cells were assayed, as the intracellular pool of Env in the COS7 cells was too scattered to easily photobleach or measure signal recovery. The intracellular pool in CEM-A cells, on the other hand, was essentially centralized into a single compartment. This region was manually traced to define the region to be photobleached. The segmented region was then scanned by a high energy 405 nm laser for ~25 seconds to irreversibly bleach all fluorophores (iLas² photobleaching galvo scanner), leaving the cell surface pool of labeled Env as the only fluorescently labeled

population, which could then be endocytosed to recover signal in the photobleached region. Time lapses were imaged of each cell at 1 minute intervals, with the Atto565 dyes excited by a 561 nm laser at approximately $340 \pm 5 \mu\text{Wcm}^{-2}$. Photobleaching of the intracellular pool was done after 5 intervals, to establish a baseline intensity. Recovery was measured for 35 intervals after photobleaching.

Image analysis and quantification of signal recovery was done by Nairi Pezeshkian. The intensity of the segmented region of photobleaching was measured for each interval before and after photobleaching. These values were corrected for background signal, using the average intensity of regions on the unoccupied coverslip, and for any bleaching not due to the 405 nm laser scanning step, using the total background-corrected intensity of un-scanned cells in the same field of view, fit to a linear decay. The recovered intensity at each interval was averaged across four biological replicates for each genotype and the resulting recovery curve was fit, weighted by the standard deviations of each averaged value, to an exponential function whose rate constant described the rate of recovery.

This assay had several caveats: it was highly dependent upon post-labeling timepoint and the remaining un-endocytosed Env pool on the cell surface, the in-focus field of view did not encompass the entire recycling endosome and, although photobleaching was not limited to the focal plane, detection of signal recovery was, and the recovery of the intracellular signal was a net measurement and could not differentiate increase of signal by endocytosis from loss of signal by recycling back to the plasma membrane. However, it did allow us to compare the overall flux of intracellular Env genotypes.

We found that recovery of intracellular CTΔ144-Env was significantly impaired compared to WT, which fits with a defect in endocytosis of CTΔ144-Env (Figure 4.6). The rate of signal recovery of CTΔ144-Env was more than 10 times slower than that of WT-Env, and the total recovery at the end of the experiment was considerably less. On the other hand, intracellular d8-Env signal recovered to a similar degree to WT-Env, despite having a smaller cell surface pool of labeled Env to endocytose (Figure 4.1). The rate of recovery of d8-Env was somewhat slower

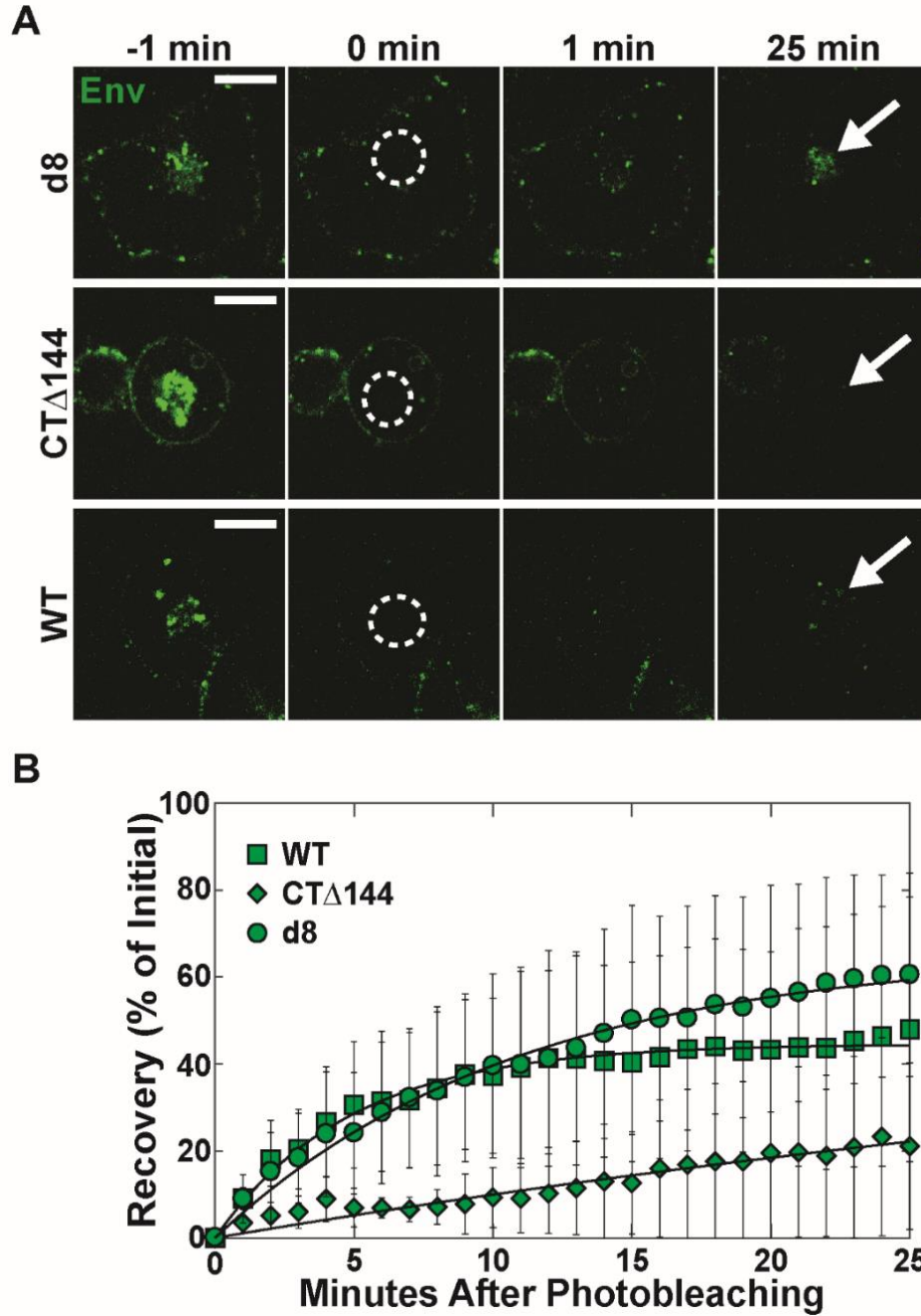


Figure 4.6. Analysis of intracellular Env flux by Fluorescence Recovery After Photobleaching. (A) Representative time lapses showing the recovery of intracellular Env pools (white arrows) in live pulse-chase labeled CEM-A cells before and after photobleaching of the intracellular compartment (dashed white circles). Scale bars are 20 μ m. (B) Recover curves show reduced recovery rates of intracellular CT Δ 144-Env (0.016 ± 0.01 s $^{-1}$, n = 4 cells), relative to both WT-Env (0.21 ± 0.01 s $^{-1}$, n = 4 cells) and d8-Env (0.092 ± 0.01 s $^{-1}$, n = 4 cells). The rate of recovery of d8-Env is reduced compared to WT-Env, but the final percent recovery is similar for the two genotypes. Error bars indicate standard deviation of each time point.

than WT-Env, which could be explained by the endocytosis of a less dense population of fluorescent Env. Possibly, the comparable percent recovery between the two genotypes is due to a buildup of intracellular d8-Env that is defective for recycling back to the cell surface, whereas WT-Env fluxes out of the intracellular pool as well as in, decreasing the apparent net recovery of signal. This assay cannot definitively prove either of these models.

Collectively, these assays support the hypothesis that the cell type dependent unbiased distribution of WT-Env on assembling virus particles that we observed in COS7 cells results from major differences in the host cell recycling pathway compared with the T-cell like CEM-A cells. This, in turn, supports the model that in T-cells, rapid endocytosis and retention of Env in the recycling pathway, with limiting quantities being returned to the plasma membrane, regulate the density of Env on the cell surface during Gag lattice formation and thereby regulate the density of Env incorporation into virus particles (Figure 4.7).

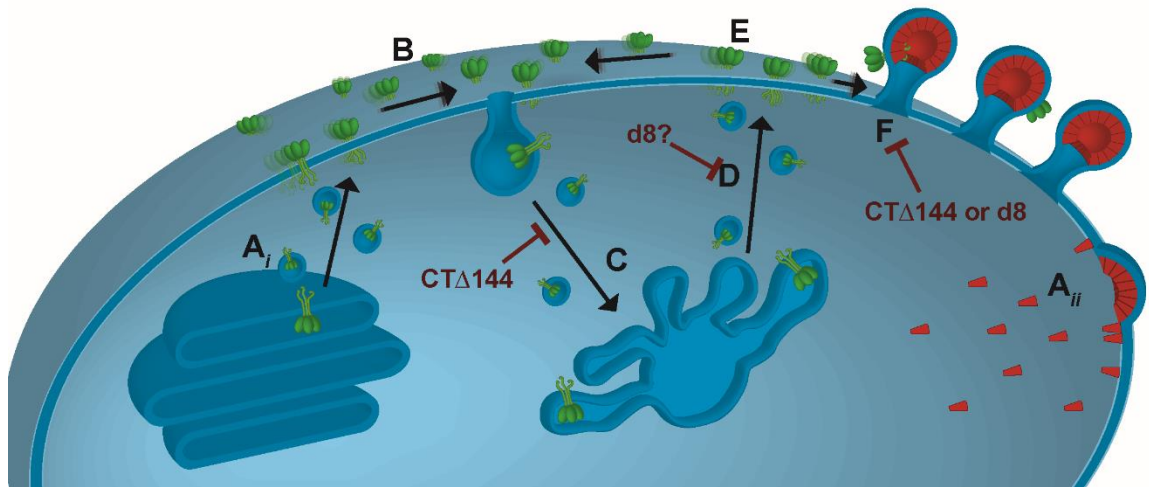


Figure 4.7. Working model for the fate of single Env trimers during HIV-1 assembly. (A_i) Env is synthesized at the endoplasmic reticulum and mature trimers traffic to the plasma membrane through the secretory pathway. (A_{ii}) Gag is synthesized in the cytoplasm and targeted to the plasma membrane, where it forms a protein lattice and causes budding of the plasma membrane. (B) Env trimers diffuse laterally on the plasma membrane and either become entrapped in assembling Gag lattices or are rapidly internalized through clathrin-mediated endocytosis. Truncation of the Env-CT (CTΔ144) impairs Env internalization, leading to increased levels of surface-exposed Env. (C) Endocytosed Env is sorted to the recycling endosome. (D) In T-cells, internalized Env is predominantly retained intracellularly, while limited quantities of Env are recycled back to the plasma membrane. Specific recycling may be regulated by interactions between host cell factors and elements of the Env-CT. (E) Upon recycling of Env to the plasma membrane, Env trimers once again diffuse laterally and either become entrapped in Gag lattices or are re-endocytosed. (F) Intracellular retention of Env leads to low densities of surface-exposed Env, increasing the probability that Env trimers will encounter pre-formed Gag lattices rather than low-order Gag oligomers, which results in the observed neck-biased distributions of Env. Truncation or mutation of the Env-CT results in a defect in Env interaction with Gag lattices and ultimately a defect in incorporation of Env trimers into virus particles.

CHAPTER FIVE: CONCLUSIONS

We sought to identify the mechanisms that regulate the incorporation of Env into HIV-1 virus particles by interrogating the timing of Env arrival at sites of particle assembly, encoded in the angular distribution of lattice-trapped Env trimers. We discovered an angular bias toward the necks of the budding particles which was dependent on the presence of the long cytoplasmic tail of Env, and on the host cell type. The angular bias of incorporated Env toward the necks of viral buds suggested that, on average, Gag lattices begin to assemble at the plasma membrane before Env arrives at these assembly sites, making it unlikely that Gag is specifically recruited by the presence of Env, and limiting the amount of Env that can be incorporated into the particle before abscission and release. The incorporation of Env was upregulated and the neck-biased distribution of Env was not observed in the second cell line tested, the fibroblast-like COS7. However, since it was observed in the T-cell-like cell line CEM-A, which can be assumed to be a better model for the natural host cell type of an HIV-1 infection, it can be expected that the neck-biased angular distribution of Env is representative of the incorporation of Env in a real infection, while the unbiased angular distribution observed in the COS7 cells is indicative of a cell type specific difference in some crucial host cell mechanism integral to the proper regulation of Env incorporation. The unbiased distribution of Env in the COS7 line indicates that Env arrives at assembly sites earlier in these cells than in the CEM-A line, suggesting that the mechanism of regulated incorporation is related to the timing of Env arrival at assembly sites.

The neck-biased phenotype could be rescued in COS7 cells by mutation of the Env-CT, though not necessarily by mimicking the same mechanism. The d8 mutation's capability to induce a neck-biased distribution in particles assembling on COS7 cells appears to be due to clashing with the Gag lattice, supported by previous studies proving that mutations in the Gag MA domain

can rescue the incorporation defects associated with the d8 mutation (Murakami and Freed, 2000; Tedbury et al, 2013). However, we also considered the possibility that the host cell mechanism that regulates the timing of Env arrival may be disrupted by the d8 mutation as well.

We conducted further experiments to better understand this host cell mechanism. We used single particle tracking of Env on the surfaces of live cells to confirm the model of cytoplasmic tail-dependent trapping of Env in Gag lattices that was crucial to the design of our initial experiments measuring angular distributions. The unbiased distributions of CTΔ144-Env, compared with the neck-biased distributions of WT- and d8-Env, already supported this model but did not prove it conclusively. Our single particle tracking data was able to show that significantly less Env becomes immobilized when the cytoplasmic tail is removed.

However, our confocal imaging experiments suggest a possible alternative interpretation for both the unbiased angular distribution of CTΔ144-Env and the decreased fraction of immobilized Env on the cell surface. Both results could be explained by the much higher density of CTΔ144-Env observed on the plasma membrane. A larger total population of cell surface Env could cause a similar number of trapped Env trimers, immobilized by a constant density of Gag, to appear to be a smaller fraction of the larger total. However, our other experiments make this explanation implausible. First, it is inconsistent with the observed defect in CTΔ144-Env incorporation into released particles. If the unbiased distribution of CTΔ144-Env resulted from an increased density of trapping-competent cell surface Env, then the density of Env on released particles would also necessarily be increased. Second, the increased mobile fraction of CTΔ144-Env is also seen in COS7 cells, which did not have a higher density of plasma membrane Env compared with WT. In addition, the increased mobile fraction of CTΔ144-Env in both cell types cannot be explained by saturation of the Env-trapping capacity of the constant density of Gag because previous studies show that incorporation of CTΔ144-Env into released particles is not saturable, whereas incorporation of WT-Env is (Qi et al, 2013). Given this, our data better supports the previously proposed model that the unbiased angular distribution and the decreased immobile fraction of CTΔ144-Env result because the cytoplasmic tail is necessary for the lattice

trapping of Env. This, in turn, leads to the incorporation defect; the failure of Env to become trapped in lattices decreases the chance of Env being present on the particle surface when the particle pinches off from the cell membrane, even at increased cell surface Env densities.

The fact that the diffusion behaviors we observed by single particle tracking did not seem to differ between the two cell types means that these behaviors cannot explain the difference in Env angular distributions between them, which means that the host cell mechanism regulating the timing of Env-Gag encounters is not related to the diffusion characteristics of Env on the plasma membrane. We hypothesized that this timing could be regulated instead by the density of Env on the plasma membrane. Given the known endocytosis and recycling pathway of Env, the cell surface density of Env could be regulated by the endocytosis and intracellular retention of Env. We showed that the levels of intracellular WT-Env were considerably higher than CTΔ144-Env in CEM-A cells, but approximately the same as CTΔ144-Env in COS7 cells. Cell surface levels of WT-Env were low, compared with CTΔ144-Env in CEM-A, but slightly higher than CTΔ144-Env in COS7. These results are suggestive of a cytoplasmic tail-dependent regulation of trafficking through the recycling pathway by host cell machinery in the CEM-A cell line that is altered or absent in the COS7 cell line. In the T-cell-like CEM-A line, WT-Env becomes significantly internalized and sequestered in intracellular compartments, leading to Env encounters with Gag lattices late in lattice assembly, whereas the fibroblast-like COS7 cells either do not efficiently internalize or do not significantly retain Env intracellularly, leading to a much higher density of Env on the plasma membrane, earlier encounters with assembling Gag lattices, and increased incorporation into released particles.

Removal of the cytoplasmic tail of Env was shown to impede internalization of Env, but the d8 mutation does not appear to impair endocytosis. In fact, as the intracellular pool of d8-Env is larger and the cell surface pool smaller than WT in both cell types, it seems that either internalization or retention, or possibly both, is upregulated by the d8 mutation. This could be explained by the single particle tracking data that shows that d8-Env trapping in Gag lattices is defective, which may cause more Env to be endocytosed because more un-trapped Env is

available. This seems to be supported by the comparison of Env incorporation between released particles produced by the two cell types. The cell type dependent differences observed for WT- and CTΔ144-Env were not seen in d8-Env, which would indicate that the incorporation defect seen in d8-Env is cell type independent. On the other hand, the FRAP results seemed to suggest that in CEM-A cells, retention of d8-Env may be upregulated compared with WT-Env. This assay cannot isolate endocytosis from recycling to the plasma membrane, however, so further experiments will be needed to establish if the d8 mutation impedes recycling to the plasma membrane.

Development of a direct assay of Env exocytosis through the recycling pathway could isolate this process and allow for comparison of the return of internalized WT-Env to the plasma membrane against that of d8-Env. Preliminary protocols for such an assay have been tested, but a pH-sensitive labeling system is needed that will detect recycled Env only as it returns to the cell surface, and such a system has not yet been optimized.

Further experiments will also be needed to identify the host cell machinery responsible for regulating the recycling pathway and the intracellular sequestration of Env during Gag assembly. Previous studies have implicated the vesicular trafficking protein FIP1C in Env incorporation into released particles (Qi et al, 2013; Qi et al, 2015, Kirschman et al, 2018) but its role is not well understood. Cellular and viral tools are in development to visualize native levels of FIP1C in infected cells, in collaboration with Eric Freed's lab and with Huxley Hoffman and Sofya Norman of the Van Engelenburg lab.

These are not the only questions raised by our results. Many aspects of the system of Env incorporation into assembling HIV-1 particles remain to be fully understood. However, these experiments have illuminated the mechanisms that both positively and negatively regulate incorporation, and therefore viral infectivity and immune visibility. We have shown that incorporation is upregulated by the trapping and retention of the Env-CT when it encounters Gag lattices, that incorporation is downregulated by a low density of available Env on the plasma

membrane, and that this low density is regulated by host cell modulated sequestration of rapidly internalized Env in the intracellular recycling pathway.

REFERENCES

- Alfadhli, A., Barklis, R.L. and Barklis, E. 2009. HIV-1 matrix organizes as a hexamer of trimers on membranes containing phosphatidylinositol-(4,5)-bisphosphate. *Virology* 387(2): 466-472.
- Barbas, C.F. 3rd et al. 1992. Recombinant human Fab fragments neutralize human type-1 immunodeficiency virus in vitro. *Proc Natl Acad Sci USA* 89(19): 9339-9343.
- Betzig, E. 1995. Proposed method for molecular optical imaging. *Opt Lett* 20(3): 237-239.
- Betzig, E., Patterson, G.H., Sograt, R., Lindwasser, O.W., Olenych, S., Bonifacino, J.S., Davidson, M.W., Lippincott-Schwartz, J. and Hess, H.F. 2006. Imaging intracellular fluorescent proteins at nanometer resolution. *Science* 313(5793): 1642-1645.
- Briggs, J.A., Riches, J.D., Glass, B., Bartonova, V., Zanetti, G. and Krausslich, H.G. 2009. Structure and assembly of immature HIV. *Proc Natl Acad Sci USA* 106(27): 11090-11095.
- Buchacher, A. et al. 1994. Generation of human monoclonal antibodies against HIV-1 proteins; electrofusion and Epstein-Barr virus transformation for peripheral blood lymphocyte immortalization. *AIDS Res Hum Retroviruses* 10(4): 359-369.
- Burton, D.R., Barbas, C.F. 3rd, Persson, M.A., Koenig, S., Chanock, R.M. and Lerner, R.A. 1991. A large array of human monoclonal antibodies to type 1 human immunodeficiency virus from combinatorial libraries of asymptomatic seropositive individuals. *Proc Natl Acad Sci USA* 88(22): 10134-10137.
- Burton, D.R. et al. 1994. Efficient neutralization of primary isolates of HIV-1 by a recombinant human monoclonal antibody. *Science* 266(5187): 1024-1027.

Checkley, M.A., Luttge, B.G. and Freed, E.O. 2011. HIV-1 envelope glycoprotein biosynthesis, trafficking, and incorporation. *J Mol Biol* 410(4): 582-608.

Chojnacki, J., Staudt, T., Glass, B., Bingen, P., Engelhardt, J., Anders, M., Schneider, J., Muller, B., Hell, S.W. and Krausslich, H.G. 2012. Maturation-dependent HIV-1 surface protein redistribution revealed by fluorescence nanoscopy. *Science* 338(6106): 524-528.

Chojnacki, J., Waithe, D., Carravilla, P., Huarte, N., Galiani, S., Enderlein, J. and Eggeling, C. 2017. Envelope glycoprotein mobility on HIV-1 particles depends on the virus maturation state. *Nat Commun* 8(1): 545.

Craigie, R. and Bushman, F.D. 2012. HIV DNA integration. *Cold Spring Harb Perspect Med* 2(7): a006890

Egan, M.A., Carruth, L.M., Rowell, J.F., Yu, X. and Siliciano, R.F. 1996. Human immunodeficiency virus type 1 envelope protein endocytosis mediated by highly conserved intrinsic internalization signal in the cytoplasmic domain of gp41 is suppressed in the presence of the Pr55gag precursor protein. *J Virol* 70(10): 6547-6556.

Ellison, V., Abrams, H., Roe, T., Lifson, J. and Brown, P. 1990. Human immunodeficiency virus integration in a cell-free system. *J Virol* 64(6): 2711-2715.

Farnet, C.M and Haseltine, W.A. 1990. Integration of human immunodeficiency virus type 1 DNA in vitro. *Proc Natl Acad Sci USA* 87(11): 4164-4168.

Freed, E.O. 2015. HIV-1 assembly, release and maturation. *Nat Rev Microbiol* 13(8): 484-496.

Freed, E.O. 2002. Viral late domains. *J Virol* 76(10): 4679-4687.

Freed, E.O and Martin, M.A. 1995. Virion incorporation of envelope glycoproteins with long but not short cytoplasmic tails is blocked by specific single amino acid substitutions in the human immunodeficiency virus type 1 matrix. *J Virol* 69(3): 1984-1989.

Gottlinger, H.G., Dorfman, T., Sodroski, J.G. and Haseltine, W.A. 1991. Effect of mutations affecting the p6 gag protein on human immunodeficiency virus particle release. *Proc Natl Acad Sci USA* 88(8): 3195-3199.

Groppelli, E., Len, A.C., Granger, L.A. and Jolly, C. 2014. *PLoS Pathog* 10(10): e1004518.

Heilemann, M., van de Linde, S., Schuttpelz, M., Kasper, R., Seefeldt, B., Mukherjee, A., Tinnefeld, P. and Sauer, M. 2008. Subdiffraction-resolution fluorescence imaging with conventional fluorescent probes. *Angew Chem Int Ed Engl* 47(33): 6172-6176.

Huang, B., Wang, W., Bates, M. and Zhuang, X. 2008. Three-dimensional super-resolution imaging by stochastic optical reconstruction microscopy. *Science* 319(5864): 810-813.

Huang, M., Orenstein, J.M., Martin, M.A. and Freed, E.O. 1995. p6Gag is required for particle production from full-length human immunodeficiency virus type 1 molecular clones expressing protease. *J Virol* 69(11): 6810-6818.

Jaqaman, K., Loerke, D., Mettlen, M., Kuwata, H., Grinstein, S., Schmid, S. and Danuser, G. 2008. Robust single-particle tracking in live-cell time-lapse sequences. *Nat Methods* 5(8): 695-702.

Jorgenson, R.L., Vogt, V.M. and Johnson, M.C. 2009. Foreign glycoproteins can be actively recruited to virus assembly sites during pseudotyping. *J Virol* 83(9): 4060-4067.

Kao, H.P. and Verkman, A.S. 1994. Tracking of single fluorescent particles in three dimensions: use of cylindrical optics to encode particle position. *Biophys J* 67(3): 1291-1300.

Kirschman, J., Qi, M., Ding, L., Hammonds, J., Dienger-Stambaugh, K., Wang, J.J., Lapierre, L.A., Goldenring, J.R. and Spearman, P. 2018. HIV-1 envelope glycoprotein trafficking through the endosomal recycling compartment is required for particle incorporation. *J Virol* 92(5): e01893-17

Klasse, P.J. 2012. The molecular basis of HIV entry. *Cell Microbiol* 14(8): 1183–1192.

Kwong, P.D., Wyatt, R., Robinson, J., Sweet, R.W., Sodroski, J. and Hendrickson, W.A. 1998. Structure of an HIV gp120 envelope glycoprotein in complex with the CD4 receptor and a neutralizing human antibody. *Nature* 393: 648-659.

Lippincott-Schwartz, J., Freed, E.O. and van Engelenburg, S.B. 2017. A consensus view of ESCRT-mediated human immunodeficiency virus type 1 abscission. *Annu Rev Virol* 4(1): 309-325.

Lucic, B. and Lusic, M. 2016. Connecting HIV-1 integration and transcription: a step toward new treatments. *FEBS Lett* 590(19): 1927-1939.

Mammano, F., Kondo, E., Sodroski, J., Bukovsky, A. and Gottlinger, H.G. 1995. Rescue of human immunodeficiency virus type 1 matrix protein mutants by envelope glycoproteins with short cytoplasmic domains. *J Virol* 69(6): 3824-3830.

McCune, J.M., Rabin, L.B., Feinberg, M.B., Lieberman, M., Kosek, J.C., Reyes, G.R. and Weissman, I.L. 1988. Endoproteolytic cleavage of gp160 is required for the activation of human immunodeficiency virus.

Murakami, T. and Freed, E.O. 2000. Genetic evidence for an interaction between human immunodeficiency virus type 1 matrix and alpha-helix 2 of the gp41 cytoplasmic tail. *J Virol* 74(8): 3548-3554.

Ono, A., Ablan, S.D., Lockett, S.J., Nagashima, K. and Freed, E.O. 2004. Phosphatidylinositol (4,5) bisphosphate regulates HIV-1 gag targeting to the plasma membrane. *Proc Natl Acad Sci USA* 101(41): 14889-14894.

Ono, A. and Freed, E.O. 2001. Plasma membrane rafts play a critical role in HIV-1 assembly and release. *Proc Natl Acad Sci USA* 98(24): 13925-13930.

Ono, A., Huang, M. and Freed, E.O. 1997. Characterization of human immunodeficiency virus type 1 matrix revertants: effects on virus assembly, gag processing, and env incorporation into virions. *J Virol* 71(6):4409-4418.

Postler, T.S. and Desrosiers, R.C. 2013. The tale of the long tail: the cytoplasmic domain of HIV-1 gp41. *J Virol* 87(1): 2-15.

Qi, M., Chu, H., Chen, X., Choi, J., Wen, X., Hammonds, J., Ding, L., Hunter, E. and Spearman, P. 2015. Maturation-dependent HIV-1 envelope glycoprotein tail mediates cel-type- and Rab11-FIP1C-dependent incorporation into virions. *Proc Natl Acad Sci USA* 112(24): 7575-7580.

Qi, M., Williams, J.A., Chu, H., Chen, X., Wang, J.J., Ding, L., Akhirome, E., Wen, X., Lapierre, L.A., Goldenring, J.R. and Spearman, P. 2013. Rab11-FIP1C and Rab14 direct plasma membrane sorting and particle incorporation of the HIV-1 envelope glycoprotein complex. *PLoS Pathog* 9(4): e1003278.

Roben, P., Moore, J.P., Thali, M., Sodroski, J., Barbas, C.F.^{3rd} and Burton, D.R. 1994. Recognition properties of a panel of human recombinant Fab fragments to the Cd4 binding site of gp120 that show differing abilities to neutralize human immunodeficiency virus type 1. *J Virol* 68(8): 4821-4828.

Roy, N.H., Chan, J., Lambele, M. and Thali, M. 2013. Clustering and mobility of HIV-1 env at viral assembly sites predicts propensity to induce cell-cell fusion. *J Virol* 87(13): 7516-7525.

Saad, J.S., Miller, J., Tai, J., Kim, A., Ghanam, R.H. and Summers, M.F. 2006. Structural basis for targeting HIV-1 gag proteins to the plasma membrane for virus assembly. *Proc Natl Acad Sci USA* 103(30): 11364-11369.

Shtengel, G., Galbraith, J.A., Galbraith, C.G., Lippincott-Schwartz, J., Gillette, J.M., Manley, S., Sougrat, R., Waterman, C.M., Kanchanawong, P., Davidson, M.W., Fetter, R.D. and Hess, H.F. 2009. Interferometric fluorescent super-resolution microscopy resolves 3D cellular ultrastructure. *Proc Natl Acad Sci USA* 106(9): 3125-3130.

Sochacki, K.A., Shtengel, G., van Engelenburg, S.B., Hess, H.F., and Taraska, J.W. Correlative super-resolution fluorescence and metal-replica transmission electron microscopy. *Nat Methods* 11(3): 305-308.

Stano, A., Leaman, D.P., Kim, A.S., Zhang, L., Autin, L., Ingale, J., Gift, S.K., Truong, J., Wyatt, R.T., Olson, A.J. and Zwick, M.B. 2017. Dense array of spikes on HIV-1 virion particles. *J Virol* 91(14): e00415-17

Sundquist, W.I. and Krausslich, H.G. 2012. HIV-1 assembly, budding, and maturation. *Cold Spring Harb Perspect Med* 2(7): a006924.

Tedbury, P.R., Ablan, S.D. and Freed, E.O. 2013. Global rescue of defects in HIV-1 envelope glycoprotein incorporation: implications for matrix structure. *PLoS Pathog* 9(11): e1003739.

Tedbury, P.R. and Freed, E.O. 2014. The role of matrix in HIV-1 envelope glycoprotein incorporation. *Trends Microbiol* 22(7): 372-378.

Tremblay, M., Sullivan, A.K., Rooke, R., Geleziunas, R., Tsoukas, C., Shematek, G., Gilmore, N. and Wainberg, M.A. 1989. New CD4(+) cell line susceptible to infection by HIV-1. *J Med Virol* 28(4): 243-249.

Trkola, A., Purtscher, M., Muster, T., Ballaun, C., Buchacher, A., Sullivan, N., Srinivasan, K., Sodroski, J., Moore, J.P. and Katinger, H. 1996. Human monoclonal antibody 2G12 defines a distinctive neutralization epitope on the gp120 glycoprotein of human immunodeficiency virus type 1. *J Virol* 70(2): 1100-1108.

Van Engelenburg, S.B., Shtengel, G., Sengupta, P., Waki, K., Jarnik, M., Ablan, A.D., Freed, E.O., Hess, H.F. and Lippincott-Schwartz, J. 2014. Distribution of ESCRT machinery at HIV assembly sites reveals virus scaffolding of ESCRT subunits. *Science* 343(6171): 653-656.

Zhou, W., Parent, L.J., Wills, J.W. and Resh, M.D. 1994. Identification of a membrane-binding domain within the amino-terminal region of human immunodeficiency virus type 1 gag protein which interacts with acidic phospholipids. *J Virol* 68(4): 2556-2569.

Zhu, P., Chertova, E., Bess, J.Jr., Lifson, J.D., Arthur, L.O., Liu, J., Taylor, K.A. and Roux, K.H. 2003. Electron tomography analysis of envelope glycoprotein trimers on HIV and simian immunodeficiency virus type 1 matrix. *Proc Natl Acad Sci USA* 100(26): 15812-15817.